Novel Soft-Rigid Hybrid Robotics Approach Enabled via Multilayered Bellow-type Soft Pneumatic Actuator

by

Seungjune Lee

A thesis
presented to the University of Waterloo
in fulfillment of the
thesis requirement for the degree of
Master of Applied Science
in
Mechanical and Mechatronics Engineering

Waterloo, Ontario, Canada, 2023

© Seungjune Lee 2023

Author's Declaration

I hereby declare that I am the sole author of this thesis. This is a true copy of the thesis, including any required final revisions, as accepted by my examiners.

I understand that my thesis may be made electronically available to the public.

Abstract

Soft robotics is an emerging field characterized by compliant and adaptable structures, presents unique challenges and opportunities for technological advancements. The thesis provided herein aimed to explore various soft robotic actuators and address critical limitations by proposing a novel Soft-Rigid Hybrid (SRH) approach. The study encompassed ideation, conceptualization, investigation, and the sharing of a multi-staged development of SRH robotics approach.

Following an extensive literature review and analysis of various soft actuators, multilayered bellow-shaped soft pneumatic actuators (MBSPAs) were selected as a basis for investigation, for their for their potential compatibility with the SRH approach. The first stage of development involved a thorough examination of the working principles and fabrication methods for layered soft pneumatic actuators, leading to the creation of the Thermoplastic Polyurethane Multilayered Bellow-shaped Soft Pneumatic Actuator (TPU-MBSPA). The TPU-MBSPA demonstrated highly efficient displacement motion, with key design variables and fabrication details documented in the thesis and submitted as a journal article to contribute to the expanding field of soft robotics. To further advance our understanding of the TPU-MBSPA and facilitate numerical simulations, extensive material characterization was conducted. Uniaxial tensile tests and additional investigations were employed to validate simplifications, isotropicity, and temperature independence. A numerical simulation model, based on experimentally obtained material data, accurately predicted the expansion performance of the TPU-MBSPA. Additional exploration of an alternative application as a displacement sensor showcased the versatility and potential applications of the TPU-MBSPA beyond its primary function.

With the TPU-MBSPA as the foundation, the study progressed to address limitations in the state-of-the-art soft grippers by introducing SRH Revolute Joint Actuator (SRH-RJA) and SRH Prismatic Joint Actuator (SRH-PJA). Detailed philosophies, designs, and constructions of these joint actuators were presented. Through iterative designs, the occurrence of radial bulging in SRH-RJA was mitigated using bio-inspired armadillo-casing and embedded casing methods, leading to significant improvements in force output. The choice of materials for the rigid components was justified based on practicality. The novelty, efficiency, and superiority of the proposed joint actuators were extensively evaluated through quasi-static displacement characterization, blocked-force output analysis, and variable joint-stiffness assessments. These key characteristics were compared with other soft-rigid hybrid robots in the literature. Additional tests, including frequency-based displacement characteristics, durability assessments with life cycle testing up to 25,000 cycles, force output, stiffness, and power density, further validated the performance of the joint

actuators. Furthermore, a proof-of-concept 3-point SRH Gripper (SRHG) demonstrated the manipulative capabilities, varied joint stiffness, and compliance when handling objects of diverse sizes, weights, and stiffness.

Leveraging the modular capability of the SRH joint actuators, a naturally compliant dexterous anthropomorphic hand was designed using the Modular SRH (MSRH) approach. By capitalizing on each SRH-RJA's active degrees of freedom (DOF), the MSRH hand offered up to 21 actively controlled DOF, making it highly adaptable and suitable for physical human-robot interaction (pHRI) while maintaining structural rigidity with the usage of rigid skeletons. The design, fabrication, and evaluation of the first MSRH prototype were presented, highlighting its lightweight and low manufacturing costs. The pneumatic soft robotic actuators provided flexibility in choosing the number of controlled DOF and joint coupling, enabling innovative solutions to spatial constraints in robotic hand design.

Finally, a preliminary pneumatic control strategy was investigated to pave the way for practical applications of the SRH approach in future fully automated systems. Adaptive control methods were studied for a 1-DOF SRH-RJA, demonstrating their potential for accurately tracking desired angular displacements of the soft-rigid hybrid actuator.

Overall, this thesis successfully provided valuable insights, demonstrations, and promising results for the proposed SRH approach in soft robotics. The comprehensive study not only established a precedent for the development of SRH robots but also contributed novel methods and procedures to expand knowledge in this emerging research field. The SRH approach holds significant potential for a wide range of applications, including delicate object handling in industries like agriculture, encouraging safe and efficient automated harvesting.

Acknowledgements

First and foremost, I would like to express my deepest gratitude to my supervisor, Professor Carolyn Ren, for her unlimited support and guidance throughout my journey since I first joined the lab back in January 2020. I have truly learned a lot from your leadership, kindness, and diligence. I would also like to thank Professor James Tung for his regular and direct guidance in our collaborative projects. It has been a great pleasure working with both of you.

I would also like to thank all of my friends and colleagues for their continuous support. Special thanks goes to all of my co-op students: Maya, Jacob, Rhys, Kelly, and Cameron. Each one of you contributed greatly to my thesis project and I am very fortunate and thankful that we could host you all in our lab.

Most importantly, special dedication goes to my family and Jana, for their unlimited unwavering support.

Table of Contents

Author's Declaration ii

Abstract iii

Acknowledgements v

List of Figures x

List of Tables xv

List of Abbreviations xvi

1 Introduction 1

1.1 Background 1

1.2 Motivation 3

1.3 Thesis Objectives and Contributions 5

1.4 Thesis Structure 6

2 Literature Review 8

2.1 Soft Actuators 8

2.1.1 Thermally Activated Soft Actuators 10

2.1.2 Photo-responsive Soft Actuators 11

2.1.3 Electromagnetic Soft Actuators . . . 11
2.1.4 Fluid-driven Soft Actuators . . . 12
2.2 Soft Pneumatic Actuators (SPA) . . . 14
2.2.1 Existing SPA Types . . . 14
2.2.2 New Generation of SPA . . . 16
2.3 SPA Implementation Approaches . . . 18
2.3.1 SPA-Enabled Soft Robotic End-Effectors . . . 18
2.3.2 SPA-Enabled Soft-Rigid Hybrid Robotics Approach . . . 19
2.4 Summary . . . 21

3 Development of Thermoplastic Polyurethane Multilayered Bellow-type Soft Pneumatic Actuator 22

3.1 Fabrication Methods . . . 22
3.1.1 Existing Layered SPA Methods . . . 22
3.1.2 Insert Material Selection . . . 24
3.1.3 Multilayered Fabrication Approach . . . 27
3.2 Material Characterization . . . 31
3.2.1 Hyperelastic Models . . . 31
3.2.2 Hyperelastic Material Test Modes . . . 34
3.2.3 Material Preparation and Testing . . . 36
3.3 Finite Element Method . . . 41
3.3.1 Material Model Evaluation . . . 41
3.3.2 FEM Simulation Setup . . . 43
3.3.3 TPU-MBSPA Estimation Results and Characteristics . . . 45
3.4 Additional Applications of TPU-MBSPA . . . 49
3.4.1 Background . . . 49
3.4.2 Methods and Results . . . 50
3.4.3 Conclusion and Limitations . . . 54

4 Soft-Rigid Hybrid Revolute and Prismatic Joint Actuators **55**
4.1 Conventional Soft Robotic Grippers . . . 55
4.1.1 Existing SRH Approaches and Limitations . . . 56
4.1.2 Project Objectives . . . 57
4.2 Soft-Rigid Hybrid Joint Actuators . . . 57
4.2.1 Design of Soft-Rigid Hybrid Revolute Joint Actuator . . . 57
4.2.2 Design of Soft-Rigid Hybrid Prismatic Joint Actuator . . . 61
4.2.3 Quasi-static Displacement Characterization . . . 62
4.2.4 Dynamic Displacement Characterization . . . 64
4.2.5 Blocked Force Output and Variable Stiffness . . . 66
4.3 Application as SRH Gripper . . . 68
4.3.1 3-Point Soft-Rigid Hybrid Gripper Design . . . 69
4.3.2 Gripper Workspace and Demonstration . . . 71
4.3.3 Conclusion . . . 73

5 Naturally Compliant Dexterous Anthropomorphic Hand via Modular Soft-Rigid Hybrid Robotics **74**
5.1 Background and Robotic Hand Philosophy . . . 74
5.1.1 Project Objectives and Motives . . . 76
5.2 MSRH Hand Design and Methods . . . 76
5.2.1 TPU-MBSPA Fabrication via Folding Technique . . . 76
5.2.2 Modular Soft-Rigid Hybrid Design Features . . . 78
5.2.3 Anthropometrics-Based Design . . . 80
5.2.4 Joint Angle Data Acquisition . . . 82
5.3 Evaluation of the MSRH Hand Prototype . . . 83
5.3.1 General Mechancial Specifications . . . 83
5.3.2 Thumb Dexterity Evaluation . . . 85
5.3.3 Demonstration of Gripping and Grasping Capabilities . . . 86
5.3.4 Conclusion . . . 86

6 Preliminary Pneumatic Control Strategies **88**
6.1 Overall System Structure and Modeling 89
6.1.1 System Definition 89
6.1.2 Pneumatic Control Dynamics 89
6.1.3 Soft Actuator Angle-Pressure Dynamics 91
6.1.4 Control Objective 93
6.2 Parameter Identifier Design 93
6.3 Controller Design 95
6.3.1 APPC Design 96
6.3.2 Feedback Linearization Design 98
6.4 Simulation Results and Discussion 100
6.5 Conclusion 101

7 Conclusions and Recommendations **102**
7.1 Thesis Conclusions 102
7.2 Recommendations 105

References **108**

APPENDICES **123**

A Detailed Fabrication Steps **124**

B ABAQUS Material Evaluation **128**

C ABAQUS FEM Model Setup **131**

List of Figures

2.1 The emergence of diverse soft actuator types developed over the past decade. This figure illustrates the segregation commonly adopted in the field of soft robotics classified into categories and subcategories based on the principle of operation [10]. 9

2.2 Examples of soft-robotic manipulation systems demonstrating a) microactuation, b) soft-continuum manipulation, c) particle jamming, d) soft-lithography based gripper, e) underactuated dextrous grasping, f) octopus-inspired manipulation, f) inflatable robotic manipulators, g) multisegmented arm, and h) a soft glove for rehabilitation [32]. 13

2.3 Conventional soft pneumatic actuators a) Pneumatic Artificial Muscle, b) Monolithic soft pneumatic actuator, c) Blow-molded bellow-type soft pneumatic actuator [36]. 16

2.4 Examples of fabric-based MBSPAs recently developed in soft robotics. a) Fabric-based MBSPAs with varied actuator designs to attain various motions, b) sample of most widely used linear MBSPAs [38, 37]. 17

2.5 Example of monolithic SPA-enabled soft robotic grasper most commonly investigated in the field of soft robotics [48]. 18

2.6 Illustration of expected variations in system output upon synergistic integration of soft and rigid robotic components [57]. 20

2.7 Examples of soft-rigid hybrid robotics approach presented in the literature. a) Enabled via blow-molded bellows-shaped SPA. b) Enabled via monolithic SPA [54, 55]. 20

3.1 The fabrication process of the low-profile single-layer SPAs previously developed at the WML toward soft robotic transtibial prosthesis interface for dynamic management of volume fluctuation and contact pressures [34]. . . 23

3.2 Samples of single-layer SPAs tested using various insert materials to determine the most feasible insert material. 25
3.3 Collage of designs tested during the development progress of TPU-MBSPA 28
3.4 The fabrication process of TPU-MBSPA. a) A schematic of key design variables, including outer diameters (OD) and inner diameters (ID) of TPU, insert, and separation layer (SL). b) Materials are prepared using the computer-controlled cutter. c) Formation of single-layered SPA. d) Stacking of multiple single-layered SPAs to form a multilayered structure. e) Insertion and gluing of tubing. Top TPU layer is designed to match the size of the tubing. f) Removal of SL results the final multilayered TPU-MBSPA [61]. 29
3.5 Example of material information readily available in the literature [76]. . . 34
3.6 Constitutive material test modes necessary to fully define hyperelastic material model. Upon the justification provided above, only uniaxial tension is studied in this thesis. 35
3.7 The three main material test modes used to fully define material model. . . 36
3.8 Tensile test setup. 38
3.9 A total of 10 raw Engineering stress-strain curves overlaid on top of one another to prevail the consistency of the hyperelastic responses. 39
3.10 Characteristics of the TPU material. a) Prevails the hyperelastic uniaxial tensile response. The results were unaffected by the heat treatment and sampled direction. b) An SEM image prevailing the distribution and the structure of the pores, supporting that the material is isotropic. 40
3.11 Stress strain comparison of hyperelastic models with the original data. . . 43
3.12 Samples of intermediate stages during FEM model setup. a) The meshed 2D axisymmetric cross-sectional model of 5-layer TPU-MBSPA. b) Result of the axisymmetric deformation simulation. c) Revolve-swept axissymetric model for better visualization 45
3.13 Automated test setup for attaining quasi-static expansion response of the 5-layered TPU-MBSPA. 46
3.14 The comparison of the quasi-static expansion behavior of the simulation and the experiment. a) To-scale visual comparison of the fully expanded state of TPU-MBSPA during the experiment and the simulation. b) Pressure-displacement estimation acquired from the FEM simulation compared with the experiment linear displacement data. 47

3.15 Quasi-static blocked force output of TPU-MBSPAs when using a) single TPU-layer, and b) doubled TPU-layer thickness. 48

3.16 Overview of the soft robotics-inspired multi-layered torus-shaped displacement compression sensing system for detecting downward movement and pistoning in prosthetic sockets [86]. 51

3.17 (a) The six LDBs manufactured for testing. (b) Top-down view of the manufactured LDBs. (c) Schematic of the LDB fabrication process [86]. . . 53

3.18 Results from vertical displacement range testing to characterize the effect of layers on LDB: (a) linearity plot. (b) Applied pressure vs. vertical displacement plot [86]. 53

4.1 The schematic entailing the key components of SRH-RJA. 58

4.2 a) Nominal operation of TPU-MBSPA in SRH-RJA. b) Radial bulging induced by a large counteracting force. As a consequence of severe radial bulging, the TPU-MBSPA malfunctioned and was not able to retract afterwards. c) Comparison of preliminary force output results when radial bulging is suppressed and unsuppressed. 59

4.3 The design of the casing methods shown in the right-side view, cross-sectional view, and the fabricated example of: a) Armadillo-inspired casing and b) embedded casing. 60

4.4 The schematic entailing the key components of SRH-PJA. 61

4.5 The displacement test setup and results of a&c) SRH-RJA and b&d) SRH-PJA. 63

4.6 a) The dynamic displacement setup used for both SRH-PJA and SRH-RJA. The frequency response and durability results of b&d) SRH-RJA and c&e) SRH-PJA 65

4.7 The test results of a) SRH-RJA obstructed force output, b) counteracting force against radial bulging, c) angular joint stiffness, d) SRH-PJA obstructed force output, d) linear joint stiffness, and e) power density. 67

4.8 a) The proof-of-concept 3-point SRH gripper. b) The co-bot in its simulation settings with the custom joint state publisher in ROS. 69

4.9 The schematic of the cascaded control setup. a) Entails the low-level controller and b) high-level controller configuration 70

4.10 a) The soft-grip workspace for stable gripping. b) Joint stiffness results of the SRH gripper. c) Collage of wide variety of objects tested for validation. 72

5.1 Fabrication details of the MBSPA joints. a) Preparation of layer components. b) Key features of the individual actuation layer. c) Heat-press to form multilayered structure. d) Second folding procedure. e) Resultant TPU-MBSPA. 78

5.2 The three modules comprising the mechanical construction of the MSRH hand. The two-piece phalanx modules have integrated pin joints and grooves to encapsulate and secure the position of the soft actuator modules and the IMU sensor. The soft skin is designed to slip onto the assembled modules. To assemble, i) Soft-actuator module is fitted into the grooves of the two-piece phalanx modules, ii) The pin is inserted for concentric alignment of pin joints and the actuator bulging constraint feature, iii) Soft skin sleeve is donned over the sub-assembly. 79

5.3 The anatomy of the MSRH hand. 81

5.4 Custom designed double-sided 6-DOF IMU PCB compared with the commercially available version. A 1 cent Euro coin is used in this figure for size reference purposes. 83

5.5 Proof of concept of the MSRH hand (left) at the resting state and (right) demonstrating its dexterity. 84

5.6 Demonstration of thumb dexterity, the MSRH hand is capable of attaining all locations specified in Kapandji Taxonomy Score. 85

5.7 Demonstration of the MSRH hand performing the grasping and gripping tasks specified in GRASP Taxonomy. 87

6.1 Overall system structure and the three dynamic subsystems. i) Represents the pressure and vacuum source considered constant in this study, ii) shows the 3/2 pneumatic solenoid valve switching between the pressure and the vacuum source. iii) Shows the pneumatic connection of the SRH-RJA to the pneumatic source via the solenoid valve. 90

6.2 The resultant plots from the experimental data. i) The step response and ii) the root locus plots of skeleton parameter-varying plant at 4 different input pressures. 92

6.3 Parameter estimation results compared to the true parameter values. As expected, the parameter estimates converge to their true values exponentially fast. 95
6.4 Performance of the State-Space APPC with driving the output angle of SRH actuator to desired target angular positions. 97
6.5 Performance of the a) Error Luenberger Observer and b) the Parameter Identifier. 98
6.6 Implementation of nonlinear feedback linearization controller 99
6.7 Implementation of nonlinear feedback linearization controller 100
6.8 Overall simulation environment incorporating all subsystems used in this study 100
6.9 Performance of the overall system in tracking of reference angles 101

List of Tables

3.1 Summary design matrix table of insert material candidates, evaluation criteria, and evaluation results. Upon this extensive investigation, Teflon-paper was selected to be the optimal insert material. 26

3.2 Summary of constitutive hyperelastic models, their respective coefficients, and the fitting errors attained from the evaluation of post-processed uniaxial test data. 42

4.1 List of objects gripped with soft-rigid hybrid gripper and their respective gripping diameter and weight. 73

5.1 Summary of key hand segment dimensions and their normalized ratio with respect to index proximal phalanx. 82

6.1 Summary of plant parameter variation fitted as a function of operating pressure. 92

List of Abbreviations

ASTM American Society for Testing and Materials 36

DOF Degrees of Freedom 57, 76, 88

FDM Fusion Deposition Modeling 45

FEM Finite Element Methods 22, 31

MBSPA Multilayered Bellow-type Soft Pneumatic Actuator 16, 21, 22, 57

MSRH Modular Soft-Rigid Hybrid 74, 76

NRE Neural and Rehabilitation Engineering Lab 22

pHRI physical human-robot interaction 2, 14, 74

PLA Polylacic Acid 45, 78

sHRI social human-robot interaction 75

SLA Stereolithography 62

SPA Soft Pneumatic Actuator 14, 21, 22, 55, 77

SRH Soft-Rigid Hybrid 4, 19, 21, 22, 55, 56

SRH-PJA Soft-Rigid Hybrid Prismatic Joint Actuator 55

SRH-RJA Soft-Rigid Hybrid Revolute Joint Actuator 55, 57, 88

SRHG Soft-Rigid Hybrid Gripper 69

TPU Thermoplastic Polyurethane 23

TPU-MBSPA Thermoplastic Polyurethane Multilayered Bellow-type Soft Pneumatic Actuator 24, 55, 56, 76

WML Waterloo Microfluidics Laboratory 22

Chapter 1

Introduction

1.1 Background

When depicting *robots* or *robotic systems*, it typically refers to electromechanical systems comprised of actuators driving motions of the attached deformation-negligible metallic mechanical linkages, often referred to as *traditional robots* [1]. Being able to perform a list of pre-programmed actions with high accuracy, reliability, and speed, traditional robots such as serial manipulators have dominated the efficiency of manual labor in repetitive and heavy-duty manufacturing tasks, which led to the development and implementation of robotic systems toward automated mass manufacturing facilities. Consequently, the productivity of consumer and industrial products has increased exponentially over the past few decades. It would not be of an exaggeration to state that development of traditional robots have greatly contributed to the exponential improvement of quality of life in modern lives, as the mass manufacturing methods allowed for the mass production and distribution of modern necessities and products such as phones, cars, electronics, etc.

The analytical theories and the numerical tools utilized in modern robotics are based on robust fundamental technologies that had already been well-established during the rapid growth of robotics as research field since the 1950s [2]. However, it should be noted that robotics as a research field started to explode only after a few research groups have successfully demonstrated the feasibility and the functional benefits, despite the fact that the ideation, underlying physics, and the background mathematics required to investigate automated robot-like systems have existed long beforehand [3]. Specifically, only after the invention of hydraulic serial manipulator *Unimate* in 1958 followed by the successful implementation in automated automobile manufacturing facilities of General Motors in

1961, the theories, applications, and implementation of robots have expanded tremendously [4]. As it is the case for many of the newly-emerging novel research fields, pioneering of a new technology requires courageous investigation of unexplored embodiment. It is a timely process involving numerous failed attempts and improvements, often requiring a successful precedent for the research field to actually start to grow.

Despite the enormous contribution of traditional robots in the early stage of robotics research, the usage had been limited to industrial applications due to safety reasons. Due to the nature of rigid metallic components that can be deadly in case of an accident, traditional robots are often provided with heavy fence guarding where humans are not allowed to coexist in the shared workspace [5]. However, with the exponential advancement of traditional robots accompanied by development of control system theories, sensor technologies, and improved processors, modern robotics attempt to explore implementing robotic systems outside the factories and industrial applications, to attain a social and collaborative environment. Known as *collaborative robots* or *cobots*, researchers have been investigating sensorization and algorithms safer for physical human-robot interaction (pHRI). Still, these robots can be dangerous in case of any unexpected malfunctioning, considering the innate nature of rigid-body robots. Hence, even with cobots humans need to abide to certain level of safety guidelines to protect themselves from injuries [6]. In other words, humans need to adjust themselves to coexist with robots. A more logical approach for coexistence would be designing robots which are inherently safe for pHRI, if possible, robots that adjust themselves to the humans and not the other way around. A newly emerging research field called *soft robotics* provides an alternative angle to contribute achieving this goal.

Soft robotics is rapidly evolving field focusing on development of robotic systems that are inherently safe for pHRI, in which the core design philosophy revolves around utilization of the innate compliant nature of soft materials [7]. As opposed to traditional rigid robots which are constructed from rigid materials, soft robots leverage soft and flexible hyperelastic materials such as elastomers and polymers, to formulate systems that are highly adaptable and compliant. The inherent compliance arises due to the continuous-deforming characteristics of hyperelastic materials, enabling the embodiment utilizing such materials to interact with objects in a more versatile and gentle manner compared to rigid robotic systems. With the added benefit of low material cost and ease of fabrication, soft robotics has been expanding rapidly as a research field since the early 2010s [8].

1.2 Motivation

There exists a wide spectrum of potential applications for soft robots. Specifically, soft robots offer new possibilities for manipulation and dexterous tasks, making them ideal for applications in industries such as healthcare, social robotics, and any applications requiring safe pHRI and handling of delicate objects. Of the numerous emerging applications, utilization of soft robotics toward the creation of end-effectors for object manipulation tasks has been the largest driving motivation in the field [9]. Soft robotic end effectors such as grippers and graspers are able to adapt their shapes to conform to the shape contour of the objects, allowing for reliable grasping of various object sizes, shapes, and textures without the need for complex control schemes and sensors. Due to the inherent compliance of soft actuators, these devices are able to provide safe and dynamic interactions with delicate and fragile objects without causing damages.

The majority of current research in the field of soft robotics is focused on developing robotic systems composed entirely of soft materials [10, 11]. However, systems comprised purely of soft materials have notable disadvantages. One significant drawback is the inherent lack of rigidity and structural stability of soft materials [12]. Due to the fact that soft robots are prone to deformation and are more susceptible to external forces, challenges arise when attempting to acquire precise and controlled movements. This limitation compromises the accuracy and repeatability required for tasks demanding high levels of precision [13]. Furthermore, the absence of structural rigidity contributes to inconsistencies in the kinematics of purely soft robots. Although kinematic trajectories are predetermined during the design phase of soft actuators, they often exhibit oscillatory motions heavily influenced by factors like gravity and external loads. In addition, soft actuators are vulnerable devices that require adequate protection elements, making purely-soft robotic systems unsuitable for real-life environments beyond laboratory settings. For example, soft actuators are prone to puncture and therefore need to be shielded from sharp objects. In contrast, purely soft robots have their soft actuators completely exposed to the environment. As a result, soft robots lack meaningful practical functionalities and their real-life implementations are significantly limited.

A potential solution to overcome the limitations of purely soft robotics is the incorporation of rigid structural components. Referred to as Soft-Rigid Hybrid (SRH) robotics approach, a few previous works have provided proof of concepts to showcase the improvements in actuator performances and to demonstrate the possibilities for hybrid robot design approaches. However, there has been limited research conducted in this area. One contributing factor is the scarcity of soft actuators that can seamlessly integrate additional components. Current soft actuators have fixed bulky sizes, making it difficult to incorporate rigid elements effectively. Furthermore, certain types of soft actuators experience a significant reduction in motion output when combined with additional components, further impeding their practicality. These limitations have restricted the exploration of the soft-rigid hybrid approach in general.

Moreover, there currently exists a significant disconnect between the newly emerging field of soft robotics and the traditional robotics approach. The field currently requires innovative interventions to bridge this divide and create designs that provide practical and feasible benefits to society. Specifically by embracing the SRH robotics approach, soft robots can unleash their full potential leading to the creation of more adaptable and capable robotic systems with enhanced capabilities. Overcoming these limitations will pave the way for significant progress in precision, control, and adaptability, revolutionizing various domains of robotic applications. It is hence the main motivation of this thesis, to harmonize the strengths of both soft and rigid components, to attempt to bridge the gap between the current limitations and the practical needs of real-world scenarios, opening doors to a new era of advanced robotics.

1.3 Thesis Objectives and Contributions

The primary aim of this thesis is to investigate various soft robotic actuators and their practical applications, taking into consideration the challenges previously discussed as well as keeping in mind the objective of developing an innovative embodiment using the soft-rigid hybrid robotics approach.

The rational behind the hybrid approach is rooted in attaining the advantages provided by both soft robotic and traditional rigid robotic methodologies, in an effort to create a system which can overcome the clear limitations exhibited in both soft robotic systems and rigid traditional robotic approaches, which were as previously summarized in section 1.2. To elaborate, the utilization of soft actuators allow the system to leverage the inherent compliance of soft robotics to facilitate the a wide range of variable joint stiffness which can be acquired without the need of a complex control system. In contrast, this would this would require an extensive sensorization, expensive computation, and complex control schemes with traditional robotics approach. This naturally provides a soft interface safe for physical human robot interaction. Moreover, the inclusion of rigid linkage systems to formulate the hybrid framework allows acquisition of structural stability, which is critical for achieving good repeatability and kinematic robustness. Without the inclusion of rigid components, the purely-soft robots would suffer from limited force output, flimsiness, and lack meaningful practical functionalities, hence limiting the real-life implementations. In addition, soft robots alone typically struggle with under-defined kinematics, unless extensive sensorization and complex models are adopted.

In order to demonstrate a successful soft-rigid hybrid embodiment, it is critical that the research first focus on inventing a novel soft actuator specifically designed for implementation in soft-rigid hybrid robotics. Given the interdisciplinary nature of soft robotics, a multidisciplinary characterization of the proposed actuator must be conducted to comprehensively evaluate its performance and potential for replication. Additionally, it is crucial to demonstrate the effectiveness and value of this new soft-rigid hybrid robotics approach through practical implementation strategies.

In summary, the main objectives and contributions of the presented theses are to:

- Conduct a comprehensive analysis of the current state-of-the-art technologies in soft robotics, and identify the specific area of study with established rationale.
- Develop a novel soft actuator ideal for soft-rigid hybrid embodiment and conduct a multidisciplinary characterization of the actuator, followed by sharing the fabrication processes, test setups, and results with the soft robotics community to facilitate knowledge exchange.
- Introduce innovative soft-rigid hybrid joint actuators formulated via seamless integration of the newly developed soft actuator with rigid components, attaining the advantages offered by both soft and rigid robotics.
- Utilize the developed soft-rigid hybrid joint actuators to create soft-rigid hybrid end effectors that are practical and functional, showcasing their viability and potential for real-world applications.
- Conduct a concise investigation of pneumatic hardware control methods using analytically derived simulation environments, thus establishing a baseline for future implementations.
- Paving the way for a broad spectrum of potential applications where the newly invented robotics approach can be utilized.

1.4 Thesis Structure

The presented thesis is prepared as follows:

- Chapter 2: Extensive literature review providing existing technologies, followed by logical rationale and justification for investigating a soft-rigid hybrid robotics approach.
- Chapter 3: Detailed development progress of the internally developed Thermoplastic Polyurethane Multilayered Bellow-shape Soft Pneumatic Actuator (TPU-MBSPA), as well as the preliminary investigation of alternative application as a displacement sensor.

- Chapter 4: Design philosophy and the rationale behind adopting Soft-Rigid Hybrids (SRH) robotics approach, leading to the formulation and characterization of SRH revolute and prismatic joint actuators via the synergistic integration of TPU-MBSPA with rigid components.
- Chapter 5: Detailed investigation of the Modular SRH robotics approach toward designing of a naturally compliant dexterous anthropomorphic hand, sharing the critical design philosophies in robotic hand design, methodologies, and evaluation.
- Chapter 6: Preliminary investigation of pneumatic control strategies specifically targeted for controlling the SRH robots.
- Chapter 7: Overall summary of the presented thesis work and recommendations of the proposed future works.

Chapter 2

Literature Review

Soft robotics is a rapidly emerging interdisciplinary research field bringing together experts and researchers from various scientific backgrounds to make impactful progress. In the multifaceted field of soft robotics, a profound understanding of existing methodologies and technologies is critical for attaining insights to identify the gaps, challenges, and opportunities for improvements in the field. By conducting a thorough analysis of the existing literature, a holistic understanding can be established to guide toward innovative advancements addressing real-world problems and advancing the field forward. This extensive review process serves as a foundation for educated decision-making and developing cutting-edge solutions in soft robotics.

This chapter entails the literature review which also provides justifications and rationale for the choice of the proposed approach, establishing a baseline. The presented review aims to synthesize the existing knowledge and identify gaps or areas that require further exploration which are presented in this thesis work.

2.1 Soft Actuators

To begin the soft actuator selection process, it is crucial to explore and comprehend the existing soft actuators. This section entails an overview of types and the underlying fundamental principles of various soft actuators. Each subsection discusses the advantages and fundamental limitations of the soft actuator type. A wide variety of soft actuator types is often categorized in the literature as shown in Figure 2.1. With further categorization, the key types of existing soft actuators can be segregated further into: thermally-activated, photo-responsive, electromagnetic, and fluidic soft actuators [10, 14, 15].

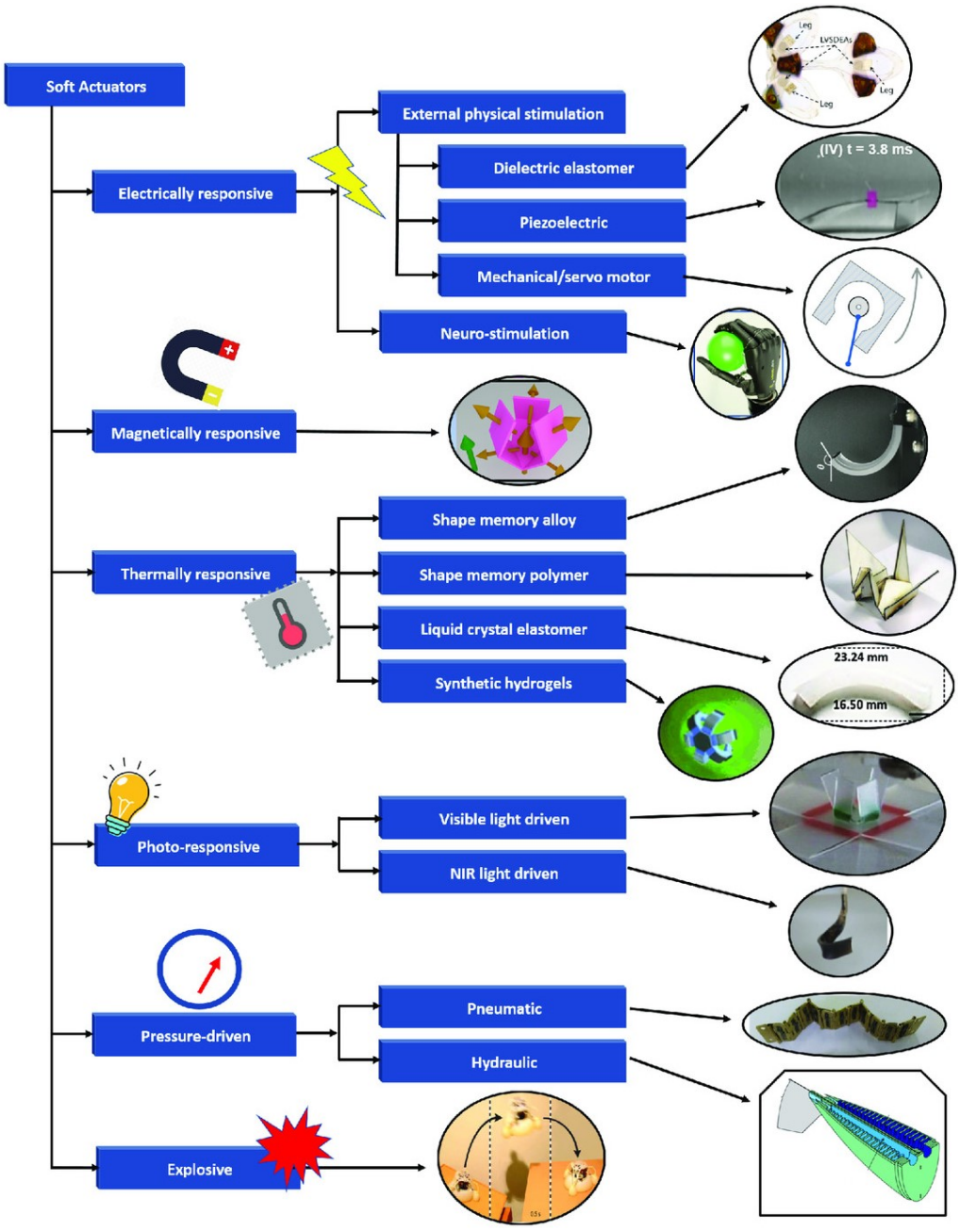


Figure 2.1: The emergence of diverse soft actuator types developed over the past decade. This figure illustrates the segregation commonly adopted in the field of soft robotics classified into categories and subcategories based on the principle of operation [10].

2.1.1 Thermally Activated Soft Actuators

A thermally activated soft actuator is a type of soft actuator in which the desired motions are achieved by actively varying the changes in actuator temperatures. To be specific, these actuators leverage the thermal expansion and contraction properties of materials to generate changes in motion, shapes, and sizes, which are typically reversible by switching the polarity of the temperature gradient.

Shape memory polymers and shape memory alloys are the commonly addressed subcategories of thermally activated soft actuators which harnesses the properties of thermally responsive materials [16, 17]. These actuators are capable of undergoing a transition between a temporary deformed state and a permanently deformed shape upon exposure to joule heating. By inducing the opposite effect of active cooling, these actuators can revert the process of deformation and return to the original shapes, hence fulfilling the name *shape memory*. This behavior is attributed to the reversible phase transition of the shape memory alloys and polymers, enabling easily repeatable actuation cycles. Another type of thermally activated soft actuator is based on liquid crystal elastomers. These materials exhibit a unique property known as the isotropic-nematic phase transition [18], which causes a change in shape and mechanical properties in response to increased temperatures. Once the internal temperature of liquid crystal elastomers exceeds the critical temperatures governed by the material selection, the isotropic-nematic transition occurs to provide bending or twisting motions, which are reversible via a decrease in temperature below the critical temperature.

The fabrication process of shape memory alloy soft actuators begins with the choice of a suitable alloy, such as nickel-titanium (NiTi) wires, selected based on the desired actuation characteristics. Similarly, the fabrication process of liquid crystal elastomer soft actuators starts with the synthesis of desired liquid crystal materials with polymer matrices to create an anisotropic structure [19]. Both types of thermally activated soft actuators are then shaped into the desired geometry using laser cutting, deposition techniques, or mold-casting methods. Following the shaping process, these soft actuators undergo training phases that involve repeated heating and cooling cycles to establish and store the desired actuator properties. These cycles allow the actuators to store their original shape and recover it after being deformed.

The advantages of thermally activated soft actuators such as high power-to-weight ratio, lightweight design, and scalability have alluded to interest in soft robotic object manipulation. However, these actuators possess notable practical drawbacks and limitations. Mainly, these actuators pose challenges in terms of designing suitable heating systems [20], ensuring precise temperature control, and optimizing actuation performance. Compared

to other types of actuators, they exhibit slow response times and are highly energy inefficient [21]. Moreover, the fabrication of thermally activated soft actuators necessitates specialized materials and equipment, and is difficult to replicate. Considering the current state of technology, thermally activated soft actuators are not a feasible choice for practical robotics applications.

2.1.2 Photo-responsive Soft Actuators

A photo-responsive soft actuator is comprised of photo-sensitive elements which provide movements when under illumination. Typically made of materials that exhibit photo-responsive behavior, such as light-sensitive polymers or hydrogels, these materials undergo reversible changes in the physical properties to provide actuation via shape transformations when provided with a light stimulus of specific wavelengths and intensities [22]. Depending on how the materials are prepared and shaped prior to exposure to light waves, photo-sensitive soft actuators can provide various movements such as bending, twisting, expanding, contracting, or a combination of these motions.

The fabrication process of photo-sensitive soft actuators involves the selection of a suitable photo-responsive material, which is then shaped into desired forms using mold-casting or photolithography techniques. To enhance their functionality, electrodes or light-responsive additives are often required to be incorporated into the actuator structure. These actuators also require extensive testing and characterization to ensure their functionality and repeatability [23]. While previous investigations have explored the programmable photo-sensitive soft actuators toward object manipulation using varied light patterns, photo-sensitive soft actuators provided lower force output compared to other types of soft actuators [24, 25]. In addition, these actuators require relatively high material costs to produce and intricate laboratory equipment. Moreover, considering that these actuators can easily be affected by other environmental lighting, which causes deviations from the desired behavior, photo-sensitive soft actuators are not feasible for practical robotic manipulation applications.

2.1.3 Electromagnetic Soft Actuators

Electromagnetic soft actuators refer to a superset of soft actuators that are magnetically, electrically, or electromagnetically activated. These actuators are comprised of piezoelectric material and dielectric or conductive polymers which convert the electric and electromagnetic inputs into mechanical movements [26]. These materials deform under high applied

voltage, typically in kilovolt-range, and are able to revert back to the original shape upon removal of potential difference. These actuators are often referred to as artificial muscles, due to their resemblance to how human muscles work.

The fabrication process for electric and electromagnetic soft actuators involves the integration of flexible materials with electrically conductive or magnetically responsive components. This includes deposition or integration of conductive electrodes onto or embedded within the soft material, in which the materials are often custom-made in laboratories specialized in the fabrication of these materials [27, 28]. Common methodologies such as 3D printing and mold-casting are then utilized to implement the outer structures of the actuators in the desired shapes and sizes.

With the ability to directly convert electrical energy to mechanical energy, electrical and electromagnetic soft actuators provide more efficient motions compared to other types of soft actuators. However, electric and electromagnetic soft actuators are extensively susceptible to mechanical hysteresis and fatigue characteristics, resulting in long-term instability and poor reliability [29]. In addition, the fabrication of these actuators is complex and requires specialized equipment with high-precision manufacturing tolerance control. Moreover, these actuators necessitate a complex and bulky power source to generate the required motions and forces, resulting in high power consumption. Therefore, the practical implementation of electromagnetic soft actuators is not feasible with the existing methods.

2.1.4 Fluid-driven Soft Actuators

Fluid-driven soft actuators are a type of soft actuators that utilize mass flow or pressurization of fluids, such as air or liquid, to attain mechanical motion via active exploitation of the continuously-deforming nature of soft materials [30]. These actuators are comprised of highly-deformable hyperelastic materials designed with internal inflation chambers, in which fluids can be displaced for internal pressurization to deform the material. When pressurized, they can provide a wide range of motions including linear translations, angular displacements, bending and twisting, as well as any combination of these motions [31]. With the ease of fabrication, low manufacturing expense, and low material cost, soft fluidic actuators are the most extensively explored option in the field of soft robotics. Examples of soft robots comprised of fluid-driven soft actuators are as shown in Figure 2.2.

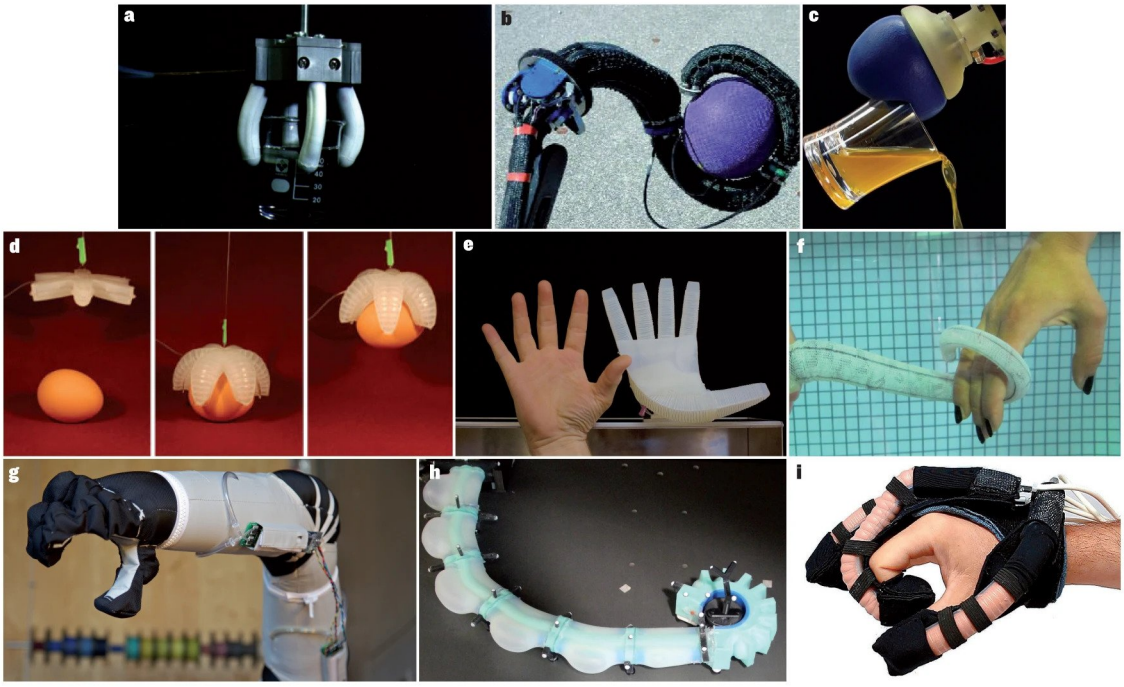


Figure 2.2: Examples of soft-robotic manipulation systems demonstrating a) microactuation, b) soft-continuum manipulation, c) particle jamming, d) soft-lithography based gripper, e) underactuated dextrous grasping, f) octopus-inspired manipulation, f) inflatable robotic manipulators, g) multisegmented arm, and h) a soft glove for rehabilitation [32].

Nevertheless, fluid-driven soft actuators come with certain limitations that need to be taken into consideration. One such limitation is their dependence on a continuous supply of fluid pressure or flow to sustain their actuation, which can restrict their portability and autonomy [33]. However, researchers are actively working on incorporating microfluidics technologies to enable the development of portable soft robots that utilize soft fluid actuators [34].

Another challenge lies in the manipulation of fluid pressure, which requires precise control systems to achieve desired actuation behaviors. In addition, the potential for leakage or failure of the fluidic components can have an impact on the overall performance and reliability of fluid-driven soft actuators. These practical considerations are often overlooked in the literature, highlighting the need for innovative approaches to address these limitations and further enhance the performance and functionality of fluid-driven soft actuators, ultimately facilitating their practical implementation in real-world applications.

2.2 Soft Pneumatic Actuators (SPA)

Often referred to as Soft Pneumatic Actuator (SPA) or soft balloon actuators, soft fluidic actuators are considered one of the most feasible options for real-life implementation among the various types of soft actuators discussed in the literature. While the term *SPA* refers to soft fluidic actuators that utilize air as the fluid medium of operation, these terms are interchangeably used in the field of soft robotics. The reason for choosing pneumatic systems is to leverage the compressible nature of air to enhance the compliance of the soft robots, characteristics particularly suitable for applications requiring safe pHRI and delicate object handling.

There exist numerous variations and types Within the subcategory of SPA. Understanding the underlying principles of operation, as well as the practical benefits and limitations of each type, is essential for establishing the justifications for the selection of specific actuators over the others. By closely analyzing these factors, educated decisions can be made about which type of SPA would be best suited for the intended application. Such considerations are critical for achieving optimal performance and functionality in soft robotic systems.

2.2.1 Existing SPA Types

McKibben muscle actuators, also known as pneumatic artificial muscles, are one of the first SPAs developed for biomechanical wearable robotics applications. Named after the inventor, J. McKibben, these actuators consist of thermoset elastomertic bladders encapsulated by a woven sleeve. When air is displaced into the bladder for pneumatic pressurization, the bladder expands radially, in which the sleeve shortens because the weaving of the sleeve is designed to comply with the contraction. During this contraction, McKibben actuators produce a pulling force similar to the contracting behavior of human muscles.

McKibben muscles offer several advantages, such as a high power-to-weight ratio, low material cost, and compliance similar to natural human muscles. However, these actuators are bulky in nature, possess high friction, and require significant power input to operate efficiently. In addition, the nature of the operating principle limits the McKibben muscles to only provide linear motion, with restricted versatility for applications requiring rotational or complex movements.

Monolithic soft pneumatic actuators have emerged as the predominant type of soft actuators that are most extensively studied in soft robotics. These actuators, often referred to as *PneuNet* or *Fast PneuNet* SPAs, were originally developed by G. Whitesides group

at Harvard University [35]. These are called *monolithic* because they are homogeneously comprised of a single integrated structure using thermoset elastomeric materials such as Ecoflex or Polydimethylsiloxane (known as PDMS). This monolithic structure eliminates the need for additional components, resulting in a simplified actuator design and fabrication process. These actuators are fabricated with internal inflating chambers during the fabrication, in which upon pressurization they deform and bulge to provide a bending motion. With the easiness of replication, numerous researchers contributed to the invention of a wide variety of monolithic SPA derivatives over the decade.

While monolithic SPAs offer simplicity and ease of fabrication, prominent challenges and disadvantages exist. These actuators also have a bulky nature, limiting their uses in applications requiring compactness or with limited spaces. They also require high input pressure to achieve the desired actuation, which together with the need for high volume displacement contributes to relatively slow response times. Most importantly, monolithic SPAs are flimsy and lack substantial structural rigidity and integrity on their own, posing threats toward utilizing these actuators for practical applications.

Blow-molded bellow-type soft pneumatic actuators are a newer category of soft actuators that utilize the blow molding fabrication technique, which is similar to the injection molding fabrication approach [36]. The usage of the blow-molding fabrication technique allows for the creation of complex geometries and intricate internal channels within the actuator, enabling precise control of the location of deformation occurrence and hence motion trajectory. The actuator structure design resembles a bellows, with accordion-like folds that expand and contract when pressurized. Considering the easily bendable nature of bellows-shape, they are better suited for applications requiring angular displacements. The blow-molded bellow-type SPAs offer a combination of simplicity in fabrication and enhanced functionality, making them an attractive choice for applications that require adaptable actuation and mass-production.

However, these blow-molded bellow-type SPAs are susceptible to radial bulging, which introduces significant impedance that greatly reduces system efficiency. While this phenomenon is observed commonly in applications where the SPAs are providing angular displacements and torques, blow-molded bellow-type SPAs specifically suffer severely from radial bulging. These actuators also require relatively high input pressure to provide a useful range of motion and possess fixed bulky volume. Examples of each SPA type explored are as shown in Figure 2.3.

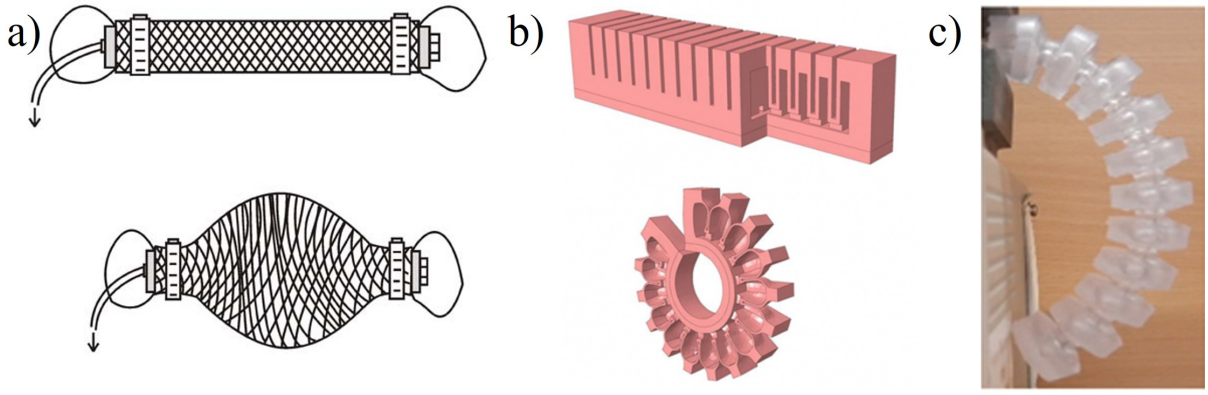


Figure 2.3: Conventional soft pneumatic actuators a) Pneumatic Artificial Muscle, b) Monolithic soft pneumatic actuator, c) Blow-molded bellow-type soft pneumatic actuator [36].

2.2.2 New Generation of SPA

To overcome the issues of inherent bulkiness and inefficiency SPAs, new methodologies have been explored using the layered fabrication approach [37], leading to the newer generation SPAs known as the Multilayered Bellow-type Soft Pneumatic Actuator (MBSPA)s. Also referred to as layered pouch-SPAs [38]. MBSPAs are comprised of multiple individual pouch-like SPAs stacked and attached on top of one another, with interconnected pneumatic connections. MBSPAs have an extremely minimal thickness of sub-centimeter range at the fully retracted state, but can provide significant expansion upon pressurization [39], achieving the highest retraction-expansion ratio amongst all existing soft actuators. Unlike the conventional SPAs relying on large inflation chambers and hence requiring high volume displacement for providing motion, MBSPAs are integrated with minimal inflation chamber that allows efficient expansion behavior. To be specific, pressurization of MBSPAs via the internal inflation chambers induces the deformation of the actuator boundaries in which in turn provides preprogrammed motion due to the geometry of the actuator during the expansion. As a result, MBSPAs provide a faster response to a smaller range of pressure increments compared to their conventional counterparts. To further elaborate the reasoning for efficient behavior, a fluid-electrical analogy can be utilized. The response of the conventional SPAs function like large capacitors (larger fixed fluid volume), whereas MBSPAs operate like small variable capacitors (small variable volume).

Despite the potential of MBSPAs and their clear benefits over the conventional SPAs, there currently exists limited investigation and exploration toward implementation in various applications. The existing research applications involve bulky-size MBSPAs, with majority relying on usage of fabrics and textiles. However, the reliance on fabric-based materials in MBSPA construction presents challenges in material characterization and in estimating actuator performances, often requiring a trial-and-error design approach [40]. Examples of fabric-based MBSPAs and illustration of their working principle are implicitly as shown in Figure 2.4. In addition, fabrics and textiles typically possess anisotropy along with a limited range of deformation which inherently limits the expansion range of MBSPAs [41]. While the replacement of fabrics with hyperelastic materials may be the remedy, limited investigation persists. Nevertheless, these new actuators are particularly suitable especially for applications where minimal bulkiness is desired.

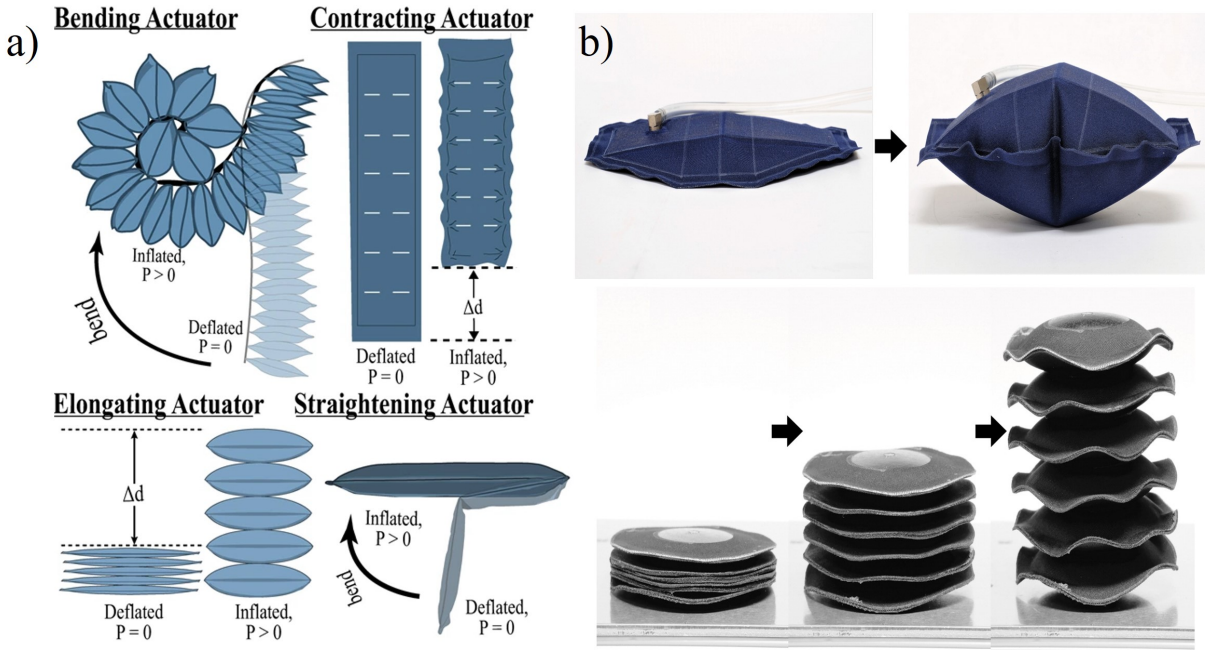


Figure 2.4: Examples of fabric-based MBSPAs recently developed in soft robotics. a) Fabric-based MBSPAs with varied actuator designs to attain various motions, b) sample of most widely used linear MBSPAs [38, 37].

2.3 SPA Implementation Approaches

2.3.1 SPA-Enabled Soft Robotic End-Effectors

The low fabrication cost and ease of replication of SPAs have attracted numerous researchers to explore the practical usage cases of SPAs. The inherent compliance of soft materials combined with the compressible nature of pneumatic systems providing additional conformity, SPAs have been deemed suitable toward the development of soft robotic end-effectors such as grippers and graspers [42, 43]. Examples of SPA-enabled soft robotic grasper are as shown in Figure 2.5. The potential benefits of these soft robots have been proven over many proof-of-concepts and seemed promising. However, as highlighted in several papers [44, 45, 46, 47], it is critical to acknowledge the prominent issues exhibited in purely-soft robotic systems. Many soft robotic end-effectors have been primarily investigated in controlled laboratory settings, with little-to-no considerations for practical parameters and often overlooking the fundamental limitations. In order for soft robotics to thrive and remain competitive as a novel robotics approach, it is essential for researchers to openly share all the limitations and challenges with complete honesty and transparency. It is through this collaborative and open approach that can help overcoming the obstacles to unlock the full potential of soft robots, ensuring success toward practical and various real-world domains.

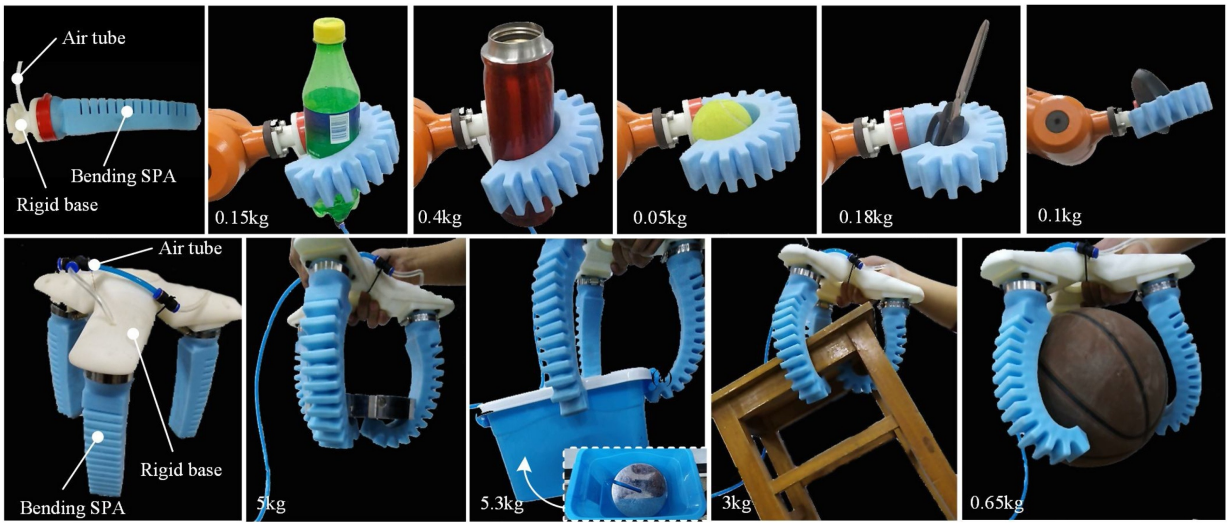


Figure 2.5: Example of monolithic SPA-enabled soft robotic grasper most commonly investigated in the field of soft robotics [48].

Soft robots purely comprised of SPAs exhibit numerous fundamental challenges that must not be overlooked. First of all, soft robots are especially vulnerable to punctures, restricting their deployment in environments where sharp objects can exist [7, 44]. For example, while delicate object handling is one of the leading investigations of soft robotic manipulation, soft grippers would not be suitable in harvesting applications with sharp edges or thorns such as blackberry and raspberry plants [49]. Moreover, the inherent flimsiness of soft robots is a double-edged sword that also introduces multiple disadvantages. While compliance is advantageous for safe pHRI, it comes with the cost of undefined kinematics which leads to poor repeatability and precision [50, 51]. Hence, soft robots are not well-suited for applications requiring high levels of accuracy and precision. In addition, all SPAs exhibit limited payload capacities arising from bulging issues that significantly reduce the system efficiency. Lastly, conventional SPAs tend to have inefficiently high power consumption, though ongoing innovations such as MBSPAs are paving the way to address this challenge.

2.3.2 SPA-Enabled Soft-Rigid Hybrid Robotics Approach

Since the early stages of development in soft robotics, the addition of rigid components has been ideated as a potential candidate for improving the performance of soft robots [7, 52]. The harmonious balance between rigidity and compliance would provide the creation of more effective manipulators and end-effectors. This approach is rather logical when considering the human hand, for example, which is comprised of rigid phalanges combined with soft ligaments and soft skins. This composition allows a uniquely remarkable combination of strength, dexterity, and flexibility. As such, designing manipulators and end-effectors using this Soft-Rigid Hybrid (SRH) robotics approach would grant the robots with added physical benefits of added safety [53], as well as increased social acceptance. The idea of attaining a balanced robotic device is as illustrated in Figure 2.6.

Examples of previous investigations utilizing the SRH robotics approach are as shown in Figure 2.7. At present, the SRH robotics approach has only been studied with conventional SPAs [54, 55, 56]. While this approach has demonstrated improved force output compared to purely-soft robots, incorporating rigid components into conventional SPAs is significantly challenging and fundamentally limited, primarily due to the inherent bulkiness of conventional SPAs. In the literature, there currently exists no feasible solutions that effectively address the challenges discussed in previous sections, highlighting the need and the opportunity requiring novel interventions.

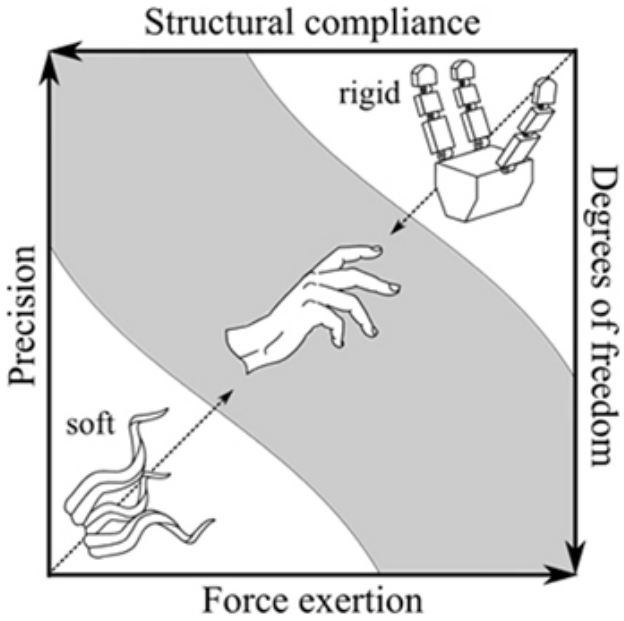


Figure 2.6: Illustration of expected variations in system output upon synergistic integration of soft and rigid robotic components [57].

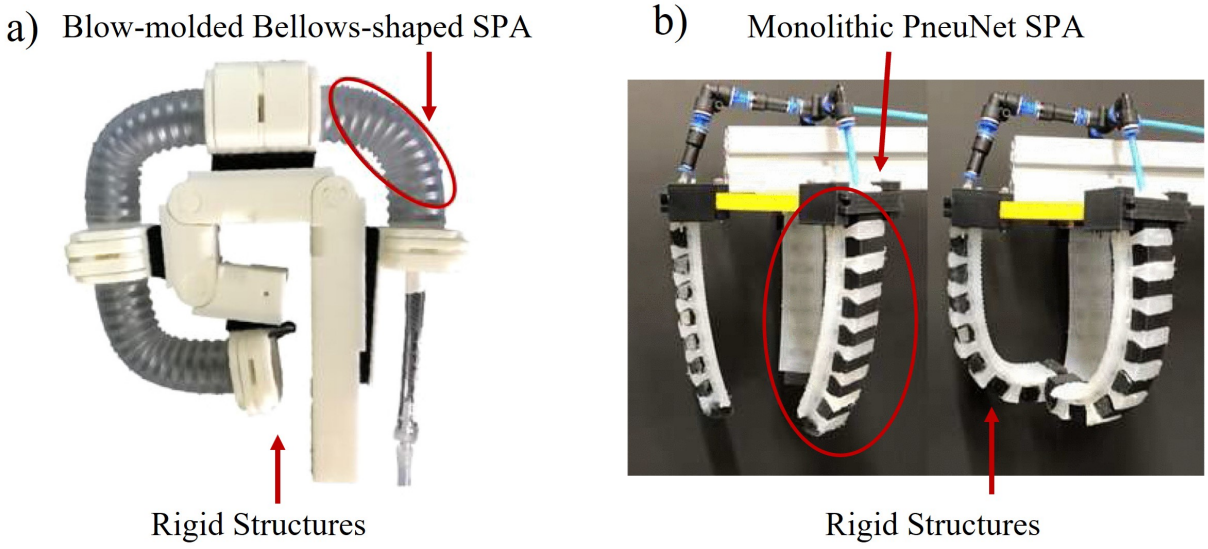


Figure 2.7: Examples of soft-rigid hybrid robotics approach presented in the literature. a) Enabled via blow-molded bellows-shaped SPA. b) Enabled via monolithic SPA [54, 55].

2.4 Summary

In the rapidly rising field of soft robotics, numerous types of soft actuators have emerged over the years. These actuators can be categorized based on their principle of operation, namely: thermally-activated, photo-responsive, electromagnetic, and fluidic soft actuators. Upon extensive literature review, it is evident that Soft Pneumatic Actuators (SPA)s offer several advantages over other types of actuators. These advantages revolve around fast actuation speed, cost-effective fabrication, ease of replication, and potential synergy with microfluidic technologies.

Being the most commonly studied type of soft actuator in soft robotics, there exists many types of SPAs that have emerged during the past decade. In general, all types of SPAs share a relatively straightforward and low-cost fabrication processes. However, conventional SPAs possess numerous disadvantages. Firstly, they are susceptible to environmental conditions especially that can cause puncture. They also lack structural rigidity, in which results undefined kinematics leading to poor repeatability and low precision. Furthermore, conventional SPAs have limited payload capacities and consume high amounts of power.

A newly invented SPA utilizing layered manufacturing approach provided an innovative angle to battle the limitation of conventional SPAs. Known as Multilayered Bellow-type Soft Pneumatic Actuators (MBSPA)s, the principle of operation is based on minimal volume, which allows these actuators to provide an unprecedentedly high efficient expansion characteristics. However, this novel actuator has not been extensively explored, especially in terms of utilizing different materials. Thus, there exists an opportunity for further investigation.

The Soft-Rigid Hybrid (SRH) robotics approach has demonstrated the significantly enhanced force output characteristics of soft robots upon implementation of rigid components. However, existing literature continues to focus utilizing conventional SPAs in SRH robotics approach, in which the additional potential improvements are fundamentally limited by the inherent limitations of conventional SPAs. With the prominent benefits MBSPAs offer, there exists a need and opportunity to investigate the SRH approach adopting this actuator. it is therefore the hypothesis of this thesis, to leverage the strengths of both soft and rigid components, aiming to bridge the current limitations and address practical needs using the newly invented MBSPAs. This ambitious endeavor seeks to open doors to a new era of advanced robotics harmoniously integrating soft and rigid robotics.

Chapter 3

Development of Thermoplastic Polyurethane Multilayered Bellow-type Soft Pneumatic Actuator

This chapter entails the detailed development progress of the MBSPA developed at the Waterloo Microfluidics Laboratory toward SRH robotics implementation. Upon review of existing methodologies, material selection and characterization are carefully executed toward the utilization of Finite Element Methods (FEM) as a design tool for the proposed actuator. This simulation approach provided a generous estimation of actuator performance, serving as an educated alternative to the previous trials-and-errors approach. Upon establishment of methodologies, actuator performances are compared with existing technologies.

3.1 Fabrication Methods

3.1.1 Existing Layered SPA Methods

As described in Section 2.2.1, the majority of the SPAs studied in soft robotics are conventional SPAs. In realization of the prominent disadvantages of conventional SPAs, research has been investigated at the Waterloo Microfluidics Laboratory (WML) in collaboration with the Neural and Rehabilitation Engineering Lab (NRE) since January 2020, in search for alternative solutions that can overcome the fundamental limitations of the existing

technologies. With a particular focus on the creation of low-profile actuators, a layered manufacturing approach has previously been adopted using Thermoplastic Polyurethane (TPU) thermal adhesive films in conjunction with microfluidic technologies toward biomechanical applications such as dynamic volume management of transtibial prosthesis [34], and toward automated Lymphedema treatment [58]. The fabrication process of the single-layered SPA developed internally at the WML is as illustrated in Figure 3.1.

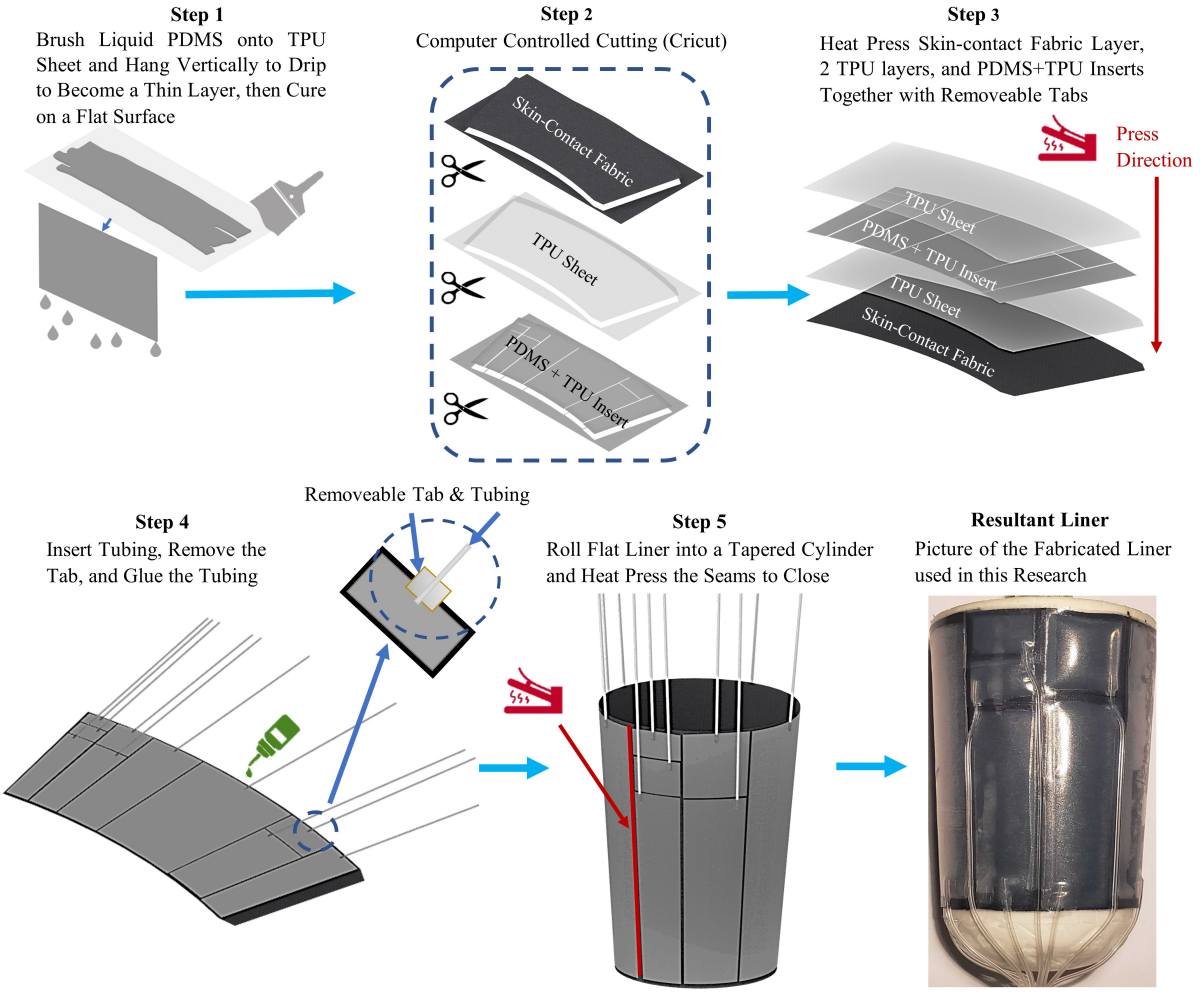


Figure 3.1: The fabrication process of the low-profile single-layer SPAs previously developed at the WML toward soft robotic transtibial prosthesis interface for dynamic management of volume fluctuation and contact pressures [34].

The fundamental principle of single-layered SPAs developed internally at the WML is based on the different surface bonding compatibility of dissimilar material combinations. Each actuator is comprised of three layers stacked on top of another: bottom TPU layer, insert layer, and top TPU layer, which are in the respective order of stacking. The insert layer is purposely designed with smaller surface area than the two surrounding TPU layers, such that the TPU layers thermally bond at the outer seams upon heat-pressing. This enclosure allows the insert layer to create an inflatable chamber, in which tubing is inserted to establish a pneumatic connection to the pressure source. When air is displaced into this chamber through the inserted tubing and the chamber is pressurized via the pressure source, hoop stress is induced to elastically deform the enclosure TPU material, resulting in the linear expansion of the single-layered SPA. Provided that the hoop stress does not exceed the elastic limit, the actuator can fully restore its elastic deformation and return to its original state upon deflation [34].

Overall, the invention of the MBSPA presented in this work leverages the fundamental self-bonding ability of TPU adhesives at elevated temperatures to create a multilayered structure via stacking of multiple single-layered SPAs developed previously. From hereon, this TPU-based MBSPA will be referred to as Thermoplastic Polyurethane Multilayered Bellow-type Soft Pneumatic Actuator (TPU-MBSPA).

3.1.2 Insert Material Selection

The single-layered SPAs are fabricated using the thermal bonding capability of Bemis 3916 Sewfree TPU thermal adhesive film (3916 Thermal Bonding Film; Bemis Associates Inc.), along with an embedded insert material. The choice of this specific TPU film lies in the benefits of low cost, availability at large bulk, and a minimal thickness of only 152 μm per layer [59]. The main purpose of the insert layer is to form an inflatable chamber within the two encapsulating TPU layers during the heat-press process. Without the insert material, the two TPU layers would simply overlap on top of one another, transforming into a homogeneous TPU layer with a larger thickness upon the heat-pressing procedure. Therefore, the insert material must be carefully selected to ensure the formation of the chamber, such that any occurrence of TPU-TPU surface bonding is prevented during the heat-pressing process.

In search of the insert material best suited for this application, a total of 9 materials were tested and evaluated. The materials investigated in this selection process are namely the: dissolvable paper, water-soluble Polyvinyl Alcohol (PVA), vinyl, fibrous fabric, non-fibrous fabric, hand-ironing without insert, Teflon membrane, Polydimethylsiloxane (PDMS) membrane, and Teflon-coated paper. To determine the compatibility of the insert material with the TPU layer, 9 single-layered SPAs were fabricated each using different candidate materials. Samples of single-layered SPAs comprised of various insert materials are as shown in Figure 3.2.

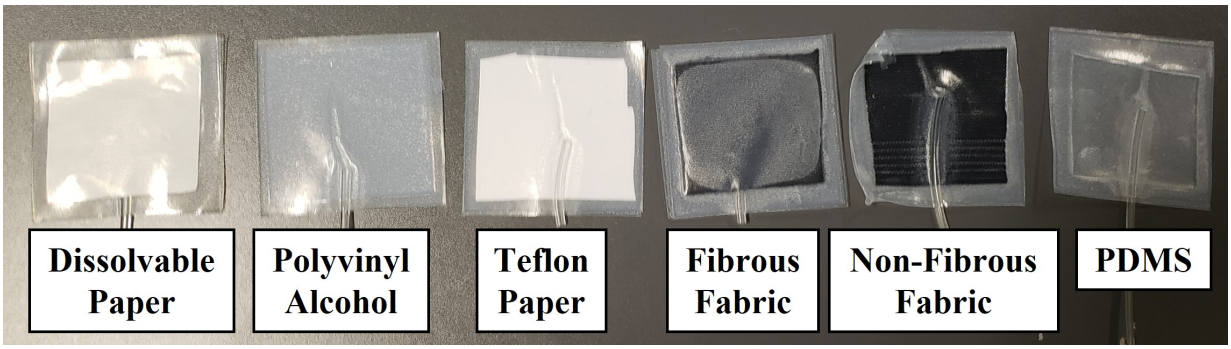


Figure 3.2: Samples of single-layer SPAs tested using various insert materials to determine the most feasible insert material.

Each SPA was evaluated using a series of important criteria regarding the functionality and practical aspects of the resultant SPA. The resultant insert material compatibility evaluations were then inputted into the design matrix, as summarized in Table 3.1. To begin with, the insert material must properly form the inflating chamber at high heat and pressure. This is because the glue-line temperature, the temperature at which the thermal bonding of TPU materials occurs, is at 110 °C [59]. This is a qualitative criterion. While most of the insert materials were capable of ensuring the proper formation of an inflatable chamber at elevated temperatures, vinyl and non-fibrous fabric materials failed to accomplish this task. These failures occurred because the vinyl insert had melted, and the TPU layer had smeared into the non-fibrous fabric cavities when the glue-line temperature was reached. Next, the friction coefficient between the insert material and TPU was evaluated by compressing the SPA with a 2 kg calibration weight and observing the resistance when detaching the layers. Friction not only contributes to the inefficiency of the system, it also induces an undesirable nonlinear stiction into the system. The evaluations were then rated from 0 to 5, with 5 possessing high frictional behavior. In this evaluation, Teflon-based materials have exhibited especially low frictional behavior. An additional functional criterion of potential for crumpling was also investigated. Crumpling

could potentially occur when the insert material is not properly anchored in its position and ends up rolled up or folded during the expansion and retraction of the SPA. This is highly undesirable since it ruins the intended performance and motion of the SPA. Teflon sheets exhibited a high tendency of curling inward to crumple.

As for the evaluation of the practical aspects of SPA, two criteria regarding the fabrication labor intensity were investigated. Firstly, the time required to prepare the insert material in the right shapes and sizes, as well as the efforts required in the alignment process of SPA fabrication were combined as one metric, rated from 0 to 5, with 5 being the hardest material for preparation. The preparation and processing of the hand-ironing method and Teflon sheet inserts required the most amount of time and effort. Lastly, the qualitative criterion of the post-processing requirement was evaluated. For example, materials such as water-soluble paper and PVA required a time-consuming process of repetitively pumping water in and out of the actuator post heat-pressing. Overall, Teflon-coated paper was chosen to be the insert material best suited for fabricating layered SPAs because it was able to properly form an inflatable chamber at high a operating temperature, provided a low-frictional interface with TPU layer, exhibited a low chance of crumpling, and ease of preparation without the need for post-processing.

Table 3.1: Summary design matrix table of insert material candidates, evaluation criteria, and evaluation results. Upon this extensive investigation, Teflon-paper was selected to be the optimal insert material.

Insert Materials	Functionality			Labor Intensity	
	Chamber	Friction	Crumpling	Preparation	Post-Processing
	Yes/No	5=Highest	5=High Chance	5=Hardest	Yes/No
Dissolvable Paper	Yes	3	0	5	Yes
Polyvinyl Alcohol	Yes	4	0	3	Yes
Vinyl	No	N/A	N/A	1	No
Fibrous Fabric	Yes	1	3	4	No
Non-Fibrous Fabric	No	N/A	N/A	3	No
Air (Hand-Ironing)	Yes	2	0	5	No
Teflon Sheet	Yes	0	5	5	No
PDMS	Yes	5	1	3	No
Teflon-Paper	Yes	0	1	1	No
				Final Choice:	Teflon-paper

3.1.3 Multilayered Fabrication Approach

MBSPAs are typically fabricated using the 2D layered manufacturing approach [37]. Many previous works had already investigated several variations of fabricating MBSPAs using different material combinations and alignment methods [40, 39, 60]. However, most MBSPAs are fabricated using a combination of fabric or textile as the actuation layers, using thermal adhesive films only for the purpose of providing thermal bonding between different layers. On the contrary, the MBSPA developed internally at the WML is a TPU-based MBSPA using the thermal adhesion properties of TPU adhesive film to function both as the continuously deforming structural actuation layer and as the self-adhesive layer, hence referred to as the TPU-MBSPAs. Adopting hyperelastic material such as TPU material as the structural layer in replacement of fabrics possesses several advantages. First, hyperelastic materials are able to provide higher elastic strain than fabric materials at a given stress. This translates to a more energy-efficient expansion behavior because TPU-MBSPAs require a lower internal pressure input to acquire the same displacement as the fabric-based MBSPAs. In addition, the fabric-based MBSPAs still require the utilization of TPU layers for thermal bonding of inter-layers, contributing to the added thickness and fundamentally challenging the goal of low-profile actuators. Lastly, most fabrics possess anisotropic characteristics which inherently adds difficulties in the simulation and modeling of the actuators, forcing researchers to adopt trials-and-errors approach.

Furbishing a new fabrication method is a timely process necessitating numerous design iterations. The TPU-MBSPA fabrication method presented in this section required a total of 21 major design revisions, not counting additional minor revisions required for perfecting the details. Figure 3.3 demonstrates a collage of key development stages of TPU-MBSPA.

The TPU-MBSPA is comprised of multiple single-layered SPA stacked together using separation layers. The separation layer is used to control the area of thermal adhesion from one single-layered SPA to another and is removed after the bonding process. As the required function of the separation layer is analogous to that of the insert layer, a Teflon-coated non-stick paper was chosen for both the insert layer and the separation layer. Specifically, the separation layer must allow two single-layered TPU actuators to bond to one another only at the specified locations while preventing the bonding at all other locations. As described previously, each TPU-based single-layered SPA consists of three layers: the bottom TPU layer, the insert layer, and the top TPU layer. While the shapes and sizes of MBSPA components can be varied depending on the intended applications, the following method resulted in highly repeatable and easy fabrication process.



Figure 3.3: Collage of designs tested during the development progress of TPU-MBSPA

A schematic of the generalized fabrication process of TPU-MBSPA developed internally at WML is as illustrated in Figure 3.4. To begin, each individual layer is designed via AutoCAD. A concentric circular design was chosen for the TPU-MBSPA for simplicity of illustration. Each component was first cut using a computer-controlled cutting machine (Cricut Maker; Cricut, Inc). Then, multiple single-layered SPAs were prepared individually with each having two layers of TPU layers placed concentrically with a sandwiched insert layer, and heat pressed at its glue line temperature of 110 °C for 30 seconds. The single-layered SPAs were then stacked one on top of another with the separation layer placed between the SPAs, and heat pressed again at 110 °C for 40 seconds. Then, a tubing (Tygon 1/32" ID x 3/32" OD; Saint-Gobain Corp.) was inserted and glued (Loctite 409; Henkel AG & Co.), and the separation layers were removed upon curing of the glue and cooling of the TPU-MBSPA. Further details of the fabrication process are as described in Appendix. A.

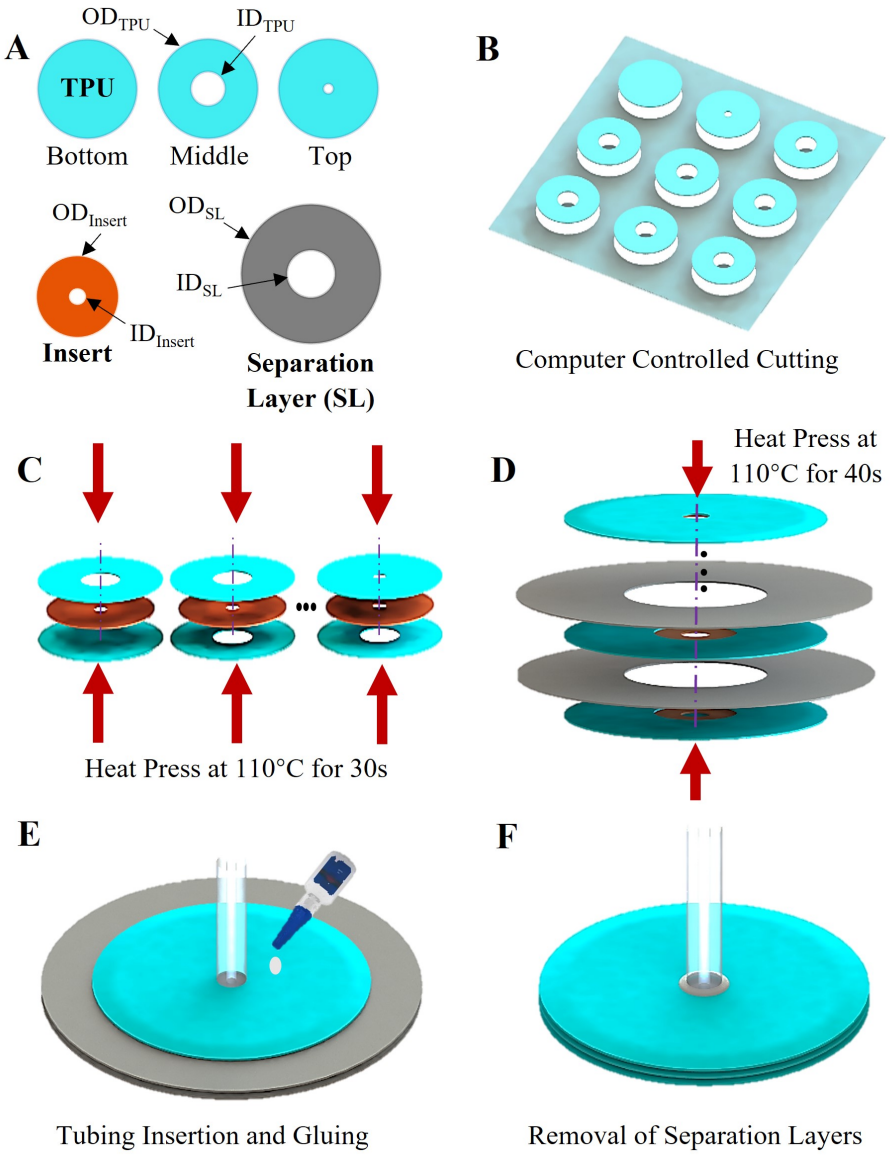


Figure 3.4: The fabrication process of TPU-MBSPA. a) A schematic of key design variables, including outer diameters (OD) and inner diameters (ID) of TPU, insert, and separation layer (SL). b) Materials are prepared using the computer-controlled cutter. c) Formation of single-layered SPA. d) Stacking of multiple single-layered SPAs to form a multilayered structure. e) Insertion and gluing of tubing. Top TPU layer is designed to match the size of the tubing. f) Removal of SL results the final multilayered TPU-MBSPA [61].

While the shapes and sizes of the TPU-MBSPA may vary depending on desired motions, force outputs, and applications, the relations (3.1) and (3.2) were found to constitute their general behavior and successful fabrication.

$$OD_{SL} > OD_{TPU} > OD_{Insert} \tag{3.1}$$

$$ID_{SL} > ID_{TPU} > ID_{Insert} \tag{3.2}$$

First, the outer diameter of the TPU layer determines the overall diameter of the TPU-MBSPA. However, it is the outer diameter of the insert layer that governs the surface area of the inflating chamber and this needs to be smaller than that of the TPU layer. The difference in the outer diameters of the TPU layer and the insert layer is a trade-off between maximizing the area for inflating chamber versus the ease of the fabrication process. For example, a larger difference between the outer diameters of TPU layer and insert layer allows easier concentric alignment but results in less area utilized for the inflating chamber. It was empirically determined that a radial clearance of 2 mm provides a good balance between ease of fabrication and maximizing the surface area of inflation.

In addition, the outer diameter of the separation layer must be larger than that of the TPU layer; otherwise, the outer seam of single-layered SPAs will thermally bond to one another. Next, the inner diameter of the insert layer needs to be smaller than that of the TPU layer; otherwise, the inner seam of single-layered SPA will thermally bond and collapse on its own. Lastly, the inner diameter of the TPU layer should be smaller than that of the separation layer. The difference in the inner diameters of the TPU layer and the separation layer governs the thermal bonding area between two single-layered SPAs, which is a compromise between bonding strength versus extension ratio.

Regardless of the fact that the techniques and detailed methodologies of TPU-MBSPA were developed internally at WML, one research group had recently published a very analogous approach [41]. This work utilized Thermoplastic Elastomer (TPE) material instead of TPU, which despite the TPU film in TPU-MBSPA being thicker than the TPU material (i.e. < 50 μm TPE versus 152 μm TPU layer), utilization of thermal adhesive TPU films allowed for lower temperature and shorter thermal bonding duration during fabrication. While the intended applications, fabrication details, and utilized materials differ, it is critical to acknowledge that this work provided the first precedent in low-profile MBSPA comprised of hyperelastic materials. However, this also supports the awareness and the need of inventing novel SPA methods being investigated in the field, further strengthening the motivation of this thesis objective to overcome the fundamental limitations of existing SPAs.

3.2 Material Characterization

In the interdisciplinary field of soft robotics, material science is especially critical in research and development of SPAs, as this process naturally encounters a wide variety of materials. In fact, a thorough material characterization of materials is crucial for establishing a new methodology and advancing the field as it brings numerous benefits. Mainly, full material characterization unlocks the ability to develop accurate hyperelastic models that govern the behavior of the SPAs. With reliable hyperelastic modeling methods, researchers can estimate the performance of the actuators during the designing phase (i.e. via FEM) [62, 63], saving valuable time and resources by avoiding a trial-and-error approach. Additionally, well-documented material characterization enables other researchers to understand and replicate, fostering collaboration and advancement in the field.

3.2.1 Hyperelastic Models

Unlike the classical solid mechanics where the deformation of materials is minimal and often considered negligible, hyperelastic material models are based on continuum mechanics in which the nonlinear continuous deformation of hyperelastic materials is considered [64, 65]. These continuum mechanics-based constitutive material models have been proven to provide a good estimation of material deformation behavior, and hence the estimation of the SPAs.

Fundamental knowledge of continuum mechanics is necessary to comprehend how hyperelastic material models work. The following background derivations and equations are the necessary components for comprehension of hyperelastic modeling that have already been well-established in continuum mechanics theory [66, 67, 68, 69, 70]. Using Einstein's tensor notation, the deformation gradient second-order tensor of an object subjected to displacement can be expressed as

$$F_{ij} = \delta_{ij} + \frac{\partial u_i}{\partial x_j}, \tag{3.3}$$

where the local volume scale factor is J=det(F).

Utilizing polar decomposition theorem which states that any second-order tensor can decompose into product of pure rotation matrix (R) and symmetric deformation tensor (U), the right and left Caushy-Green deformation tensors (C and B respectively) are formed as

$$F = RU = VR$$
$$F^T F = (RU)^T RU = U^T U = U^2 = C$$
$$FF^T = VR(VR)^T = VV^T = V^2 = B$$

The principle invariants of the right Caushy-Green deformation tensor provides

$$I_1 = tr(C), \quad I_2 = \frac{1}{2}(tr(C)^2 - tr(C^2)), \quad I_3 = det(C)$$

which can be represented in terms of the principle stretch ratios λ along principal axes as

$$I_1 = \lambda_1^2 + \lambda_2^2 + \lambda_3^2, \quad I_2 = \lambda_1^2\lambda_2^2 + \lambda_2^2\lambda_3^2 + \lambda_1^2\lambda_3^2, \quad I_3 = \lambda_1^2\lambda_2^2\lambda_3^2 \tag{3.4}$$

Skipping lengthy derivations, the nominal stress experienced by the hyperelastic material can be derived in terms of the strain energy density functions (W) to effectively predict the mechanical behavior of hyperelastic materials. Many hyperelastic models utilized in soft materials are phenomenological models based on material behavior and can be derived from two hyperelastic models which are polynomial form (3.5) and Ogden model (3.6) [71, 72]. The polynomial form represents strain energy density function by one or more of the three strain tensor invariants which is expressed as

$$W = \sum_{i+j=0}^{N} C_{ij}(I_1 - 3)^i(I_2 - 3)^j + \sum_{i=1}^{N} \frac{1}{D_i}(J-1)^{2i} \tag{3.5}$$

where I_1, I_2, I_3 are the strain tensor invariants (3.4), C_{ij} are material specific constants, D_i is fitting parameter dependent on compressibility, and J is the volume ratio before and after deformation known as the material Jacobian. Ogden model represents strain energy density function with principal stretch ratios instead of the invariants [73], which is expressed as

$$W = \sum_{i=1}^{N} \frac{2\mu_i}{\alpha_i^2}(\lambda_1^{\alpha_i} + \lambda_2^{\alpha_i} + \lambda_3^{\alpha_i} - 3) + \sum_{i=1}^{N} \frac{1}{D_i}(J-1)^{2i} \tag{3.6}$$

where μ_i is the infinitesimal shear modulus and α_i is the stiffness parameter, and these are primary fitting parameters which are multiplied with the three principal stretch ratios λ.

The coefficients of the constitutive hyperelastic strain energy density equations may vary depending on the material properties. While there exists numerous strain energy density models, the following models are most often adopted in soft robotics research. Note that the following equations assume incompressible isotropic material assumption, which is valid for numerous hyperelastic materials. The general polynomial model is

$$W = \sum_{i=0,j=0}^{N} C_{ij}(I_1 - 3)^i(I_2 - 3)^j$$

The Mooney-Rivlin model [74] which is often utilized in applications requiring moderate hyperelastic deformation, usually with strain range of under 200%, is expressed as

$$W = C_1(I_1 - 3) + C_2(I_2 - 3)$$

Then the Ogden model with incompressible assumption can be expressed as

$$W = \sum_{i=1}^{N} \frac{2\mu_i}{\alpha_i^2}(\lambda_1^{\alpha_i} + \lambda_2^{\alpha_i} + \lambda_3^{\alpha_i} - 3)$$

in which if six parameters of the third order models are defined, it can accurately describe the deformation at large strain ranges even at beyond 400%.

Lastly, the neo-Hookean model is a special case of reduced polynomial model [75], which can provide accurate estimates at lower strain range of below 50% is written as

$$W = C1(I_1 - 3) = \frac{\mu}{2}(I_1 - 3)$$

3.2.2 Hyperelastic Material Test Modes

A number of material test methods are required in order to attain the material properties necessary for fully defining hyperelastic material models. For conventional SPAs, extensive studies have already established detailed characterizations, hyperelastic material model coefficients, and methodologies. New researchers entering the realm of utilizing conventional SPAs simply need to obtain the material coefficients from the coefficient tables made readily available in the literature [45, 76]. An example of true stress-strain curves reported in the literature is as shown in Figure 3.5. The same reference contains tables of hyperelastic coefficients for each material. However, there exists insufficient information in the literature for modeling of TPU-MBSPA due to the lack of information available for TPU material. This is because previous investigations of MBSPA have mainly focused on the use of TPU only as a thermally adhesive layer rather than a continuously deforming structural layer. As a result, the required material properties specific to TPU used in TPU-MBSPA must be empirically tested and characterized, as they were not readily available in the literature.

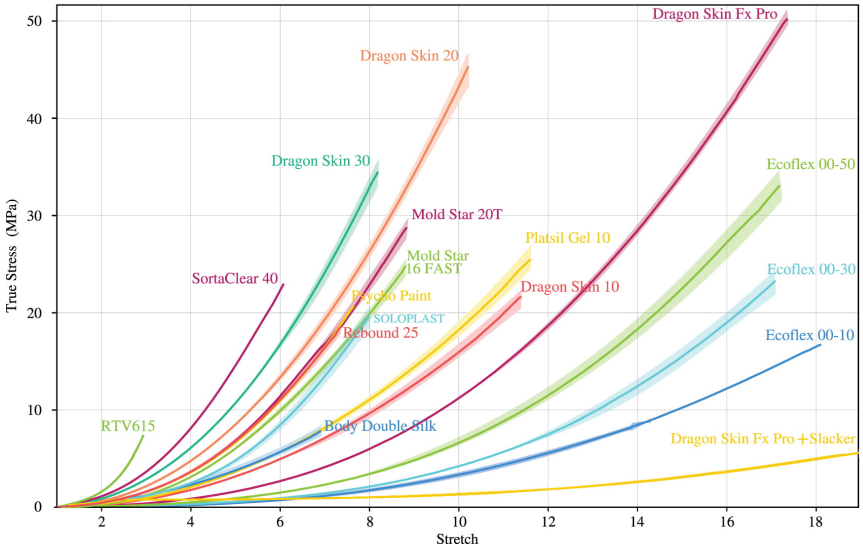


Figure 3.5: Example of material information readily available in the literature [76].

The material coefficients in hyperelastic models are typically determined using the following test modes: uniaxial tension (equivalent to equibiaxial compression), equibiaxial tension (equivalent to uniaxial compression), pure shear via planar tension (equivalent to planar compression), and volumetric deformations if the material is compressible. These test modes are as illustrated in Figure 3.6 Hyperelastic materials are generally assumed

to be incompressible [45], in which their volumetric deformations are neglected. Previous work has also validated this assumption for a similar TPU material [72]. Though equibiaxial tensile test is recommended for full description of deformation modes and improved accuracy of modeling, they require specialized testing equipment not readily available. As such, studies often used uniaxial tension and pure shear test data [71], and in most cases, used only the uniaxial tensile test data and yet obtained accurate estimation. Examples of each test mode are as shown in Figure 3.7. Given the similar limited circumstances and justifications based on the literature review, the uniaxial tensile test alone would be sufficient for the generous estimation of actuator performance via hyperelastic modeling.

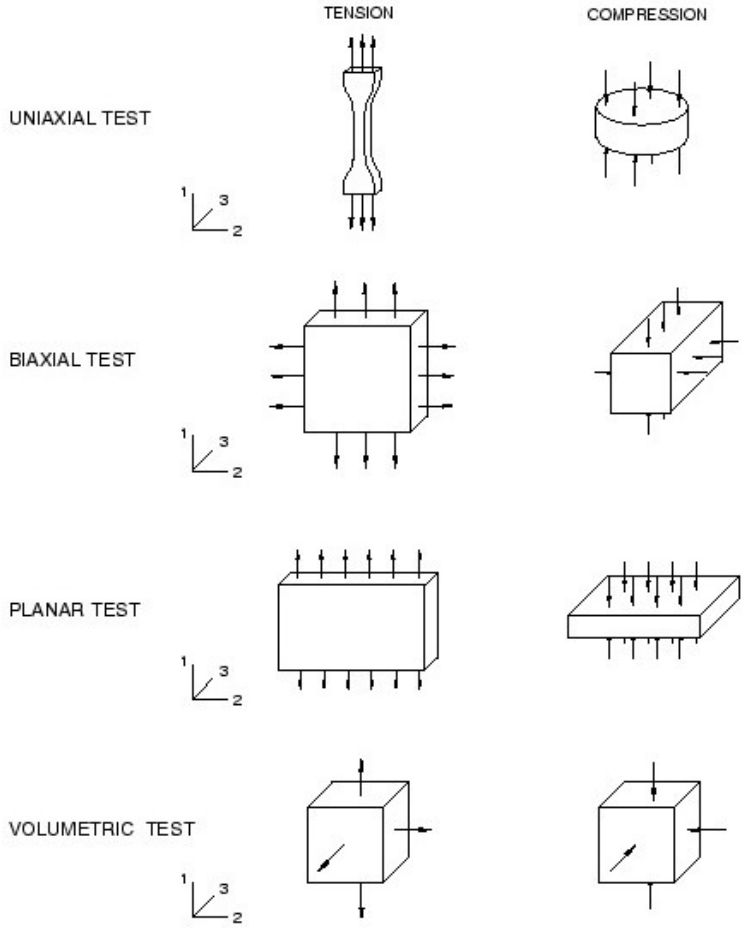


Figure 3.6: Constitutive material test modes necessary to fully define hyperelastic material model. Upon the justification provided above, only uniaxial tension is studied in this thesis.

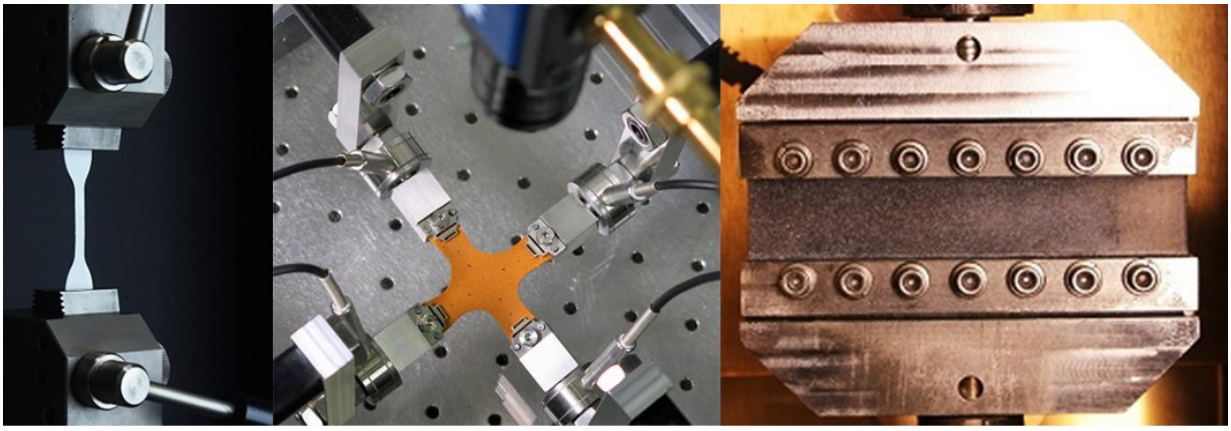


Figure 3.7: The three main material test modes used to fully define material model.

3.2.3 Material Preparation and Testing

Specific standard test methods for attaining tensile properties of a material depend on the physical properties of the material in question. According to the American Society for Testing and Materials (ASTM) standard guideline, tensile properties of plastics in the form of thin sheeting and films, specifically that of less than 1.0 mm and no greater than 0.25 mm in thickness, must follow the standard procedures provided in ASTM-D882 [77]. This ASTM standard provides the type of apparatus, test specimen dimensions, testing speed options, as well as additional details. While this standard is analogous to the standard provided by the International Standardization Organization (ISO), ISO 527-3, it is not considered technically equivalent.

The test specimens as well as the test procedures were prepared according to the standard. First, the standard specifies that the nominal width shall not be less than 5.0 mm or greater than 25.4 mm. Moreover, the width-to-thickness ratio should be of at least 8 to avoid any flaws in the longitudinal direction. Hence, the nominal width of all specimens was selected to be 15 mm. With the TPU film having a thickness of 0.152 mm, this results in width to thickness ratio of 99. Next, the gage length, which is an interchangeably referred term with grip separation, the length of the specimen in tension during the experiment, should be at least 50 mm long for general testing and be at exactly 250 mm if modulus of elasticity needs to be determined. Together with the specification of sufficient

material gripping length of at least 50 mm, the total length of the specimen was designed to be 320 mm, which is comprised of 250 mm gage length and 35 mm of gripping length on both ends of each specimen. Therefore, the resultant test specimen design which satisfied all specifications was determined to be a 15 mm by 320 mm rectangle. Uniform thickness within 10% of nominal thickness over the entire length of the specimen was also verified via caliper. All specimens were prepared using the computer-controlled cutter to prevent any nicks and tears, as specified in the standard.

As for the test method, the standard specified that a minimum of 5 specimens should be tested for each sample and every varied test setup. For general applications where the modulus of elasticity is the only characterization in question, specimens need to have an initial grip separation of 250 mm, and should be tested at a strain rate of 0.1 mm/mm*min. This translates to a rate of grip separation of 25 mm/min. In the case where additional material characteristics are in question and percent elongation at break is greater than 100, initial grip separation is reduced to 50 and strain rate increased to 10.0 mm/mm*min, translating to 500 mm/min. Upon manual trials, the percent elongation at break was determined to be over 1000%. This means that the TPU material needed to be elongated 10 times its original length to force failure, hence strain rate of 500 mm/min was more desirable. The drastic difference between the two strain rate options is because the slower strain rate focuses on describing the material behavior in a quasi-static process, whereas the faster strain rate attempts to capture additional dynamic elements of the material such as viscoelasticity. Knowing that the nominal operation of TPU-MBSPAs is under fast pneumatic actuation, a faster strain rate was chosen for material characterization.

The TPU material requires high displacement to reach material failure. To contain the hyperelasticity of this material, a specialty tensile test machine (C43-104 Criterion Electromechanical Test Systems; MTS Systems Corp) was required because other tensile test machines failed to provide enough displacement for characterization, or provided insufficient grip force onto the specimen resulting in severe slippage. Hence, specialty hydraulic grippers were also utilized in the test setup to prevent any form of slippage. The tensile test setup is as shown in Figure 3.8, and was setup with the help of a laboratory technician, at the Civil Engineering Structures, Mechanics, and Construction lab.

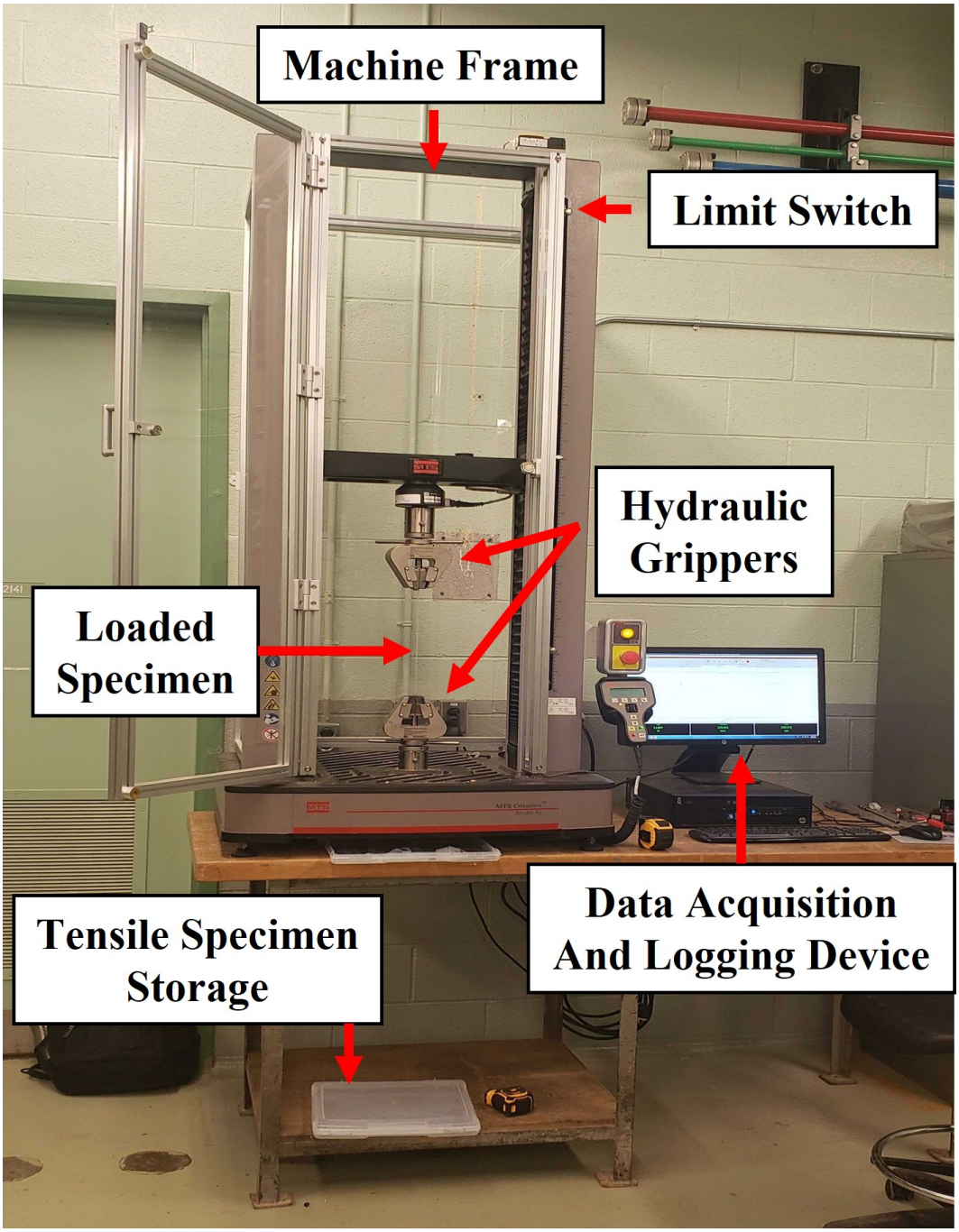


Figure 3.8: Tensile test setup.

A total of 10 tests were executed using the same setup and test parameters. The raw Engineering stress and strain data for all 10 tests were plotted on top of one another as shown in Figure 3.9. While the results were very consistent, even the specialty tensile test machine was unable to provide sufficient strain to fail the material. However, it was able to provide material strain of up to 700 %, capturing the majority of the hyperelastic response. Further investigations prevailed that the operating strain range of TPU-MBSPAs was determined to be under 100 %, and hence this material testing contained sufficient information for modeling.

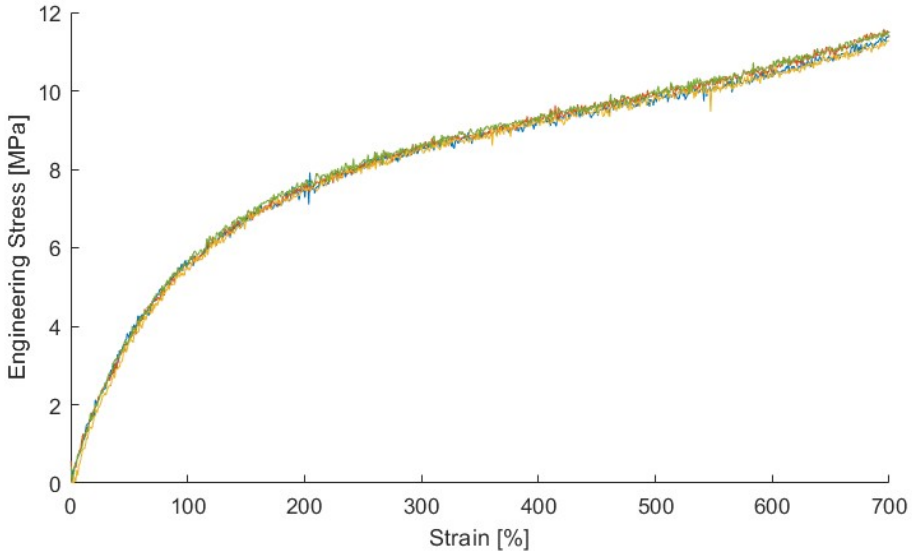


Figure 3.9: A total of 10 raw Engineering stress-strain curves overlaid on top of one another to prevail the consistency of the hyperelastic responses.

Prior to adopting FEM simulations, two additional material variations were considered and evaluated. Firstly, the TPU layers undergo an elevated heat-pressing treatment at their glue-line temperature of 110 °C during the fabrication of TPU-MBSPA. Hence, additional tests were conducted to ensure that this material heating process did not alter the mechanical characteristics of the material. Secondly, certain TPU materials are designed and fabricated with the intent to possess anisotropic properties. However, anisotropic materials necessitate equibiaxial tension material test data in order to fully define their constitutive hyperelastic models, making it significantly more difficult to accurately model using limited testing resources. To confirm the isotropic nature of the TPU material used in TPU-MBSPA, additional tests were conducted using specimens sampled along orthogo-

nal directions compared to the previous tests. As shown in Figure 3.10, the results revealed that the TPU material is not affected by the heat-pressing process and that the material has isotropic properties since the specimens sampled from orthogonal directions provided consistent results. To ensure that the TPU material is indeed isotropic, further investigation was carried out by attaining a Scanned Electron Microscopy (SEM) image of the TPU material. Upon visual inspection, it is apparent that the pores of the TPU material are not only distributed randomly across the material surface, but also the shapes of the pores are circular. This further supported that the TPU material is indeed isotropic, as the shape of the pores would be elongated to a certain direction and would have a skewed distribution if it were to be an anisotropic material.

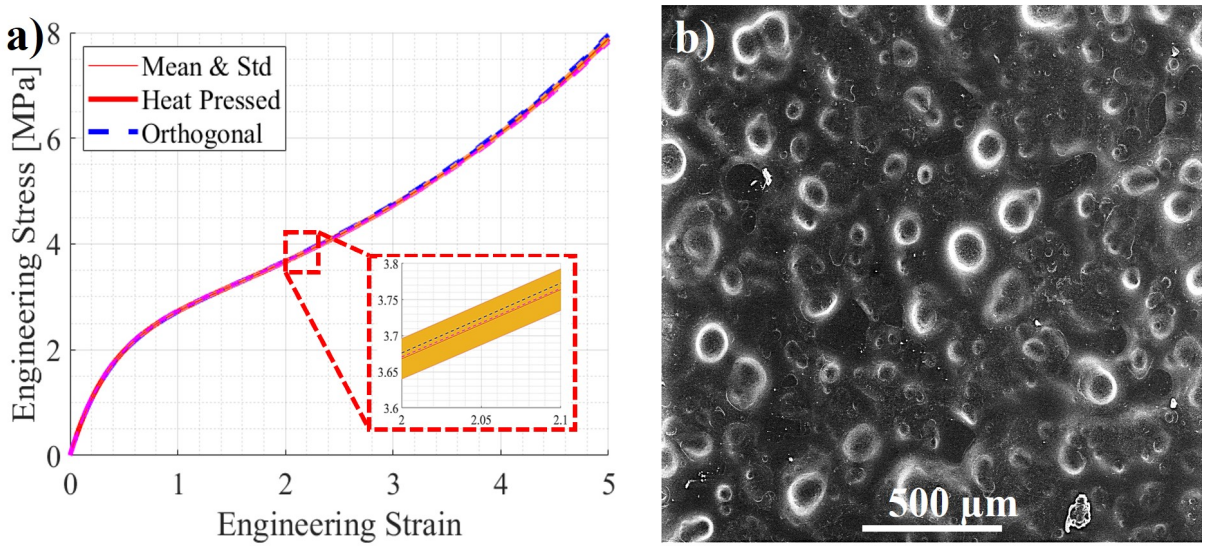


Figure 3.10: Characteristics of the TPU material. a) Prevails the hyperelastic uniaxial tensile response. The results were unaffected by the heat treatment and sampled direction. b) An SEM image prevailing the distribution and the structure of the pores, supporting that the material is isotropic.

3.3 Finite Element Method

Finite Element Method is undoubtedly one of the most commonly utilized design tools in soft robotics [78]. The benefit of FEM providing an accurate estimation of the actuator performance allows for an optimized actuator design without the need for a complex explicit analytical model to attain desired actuator behavior. By adopting FEM, empirical methods such as trials-and-error approach can be avoided to save time and resources. While hyperelastic materials generally require all hyperelastic test modes to be conducted for precise modeling, many works have provided precedents of using only uniaxial tensile measurements to attain generous estimation of the general actuator performances [79, 80, 81], which the accuracy of this approach can generally be determined beforehand by evaluating the formulated material model. The following material model evaluations and numerical simulations were conducted using ABAQUS (Abaqus CAE, Dassault Systèmes).

3.3.1 Material Model Evaluation

The hyperelastic material model coefficients were obtained using the *material evaluation* feature available in Abaqus. Specifically, custom materials can be added and defined using experimental data in the Abaqus material model module. The hyperelastic material models can be loaded through Mechanical-Elasticity-Hyperelastic tools, where the module allows data input using four material test modes: uniaxial, equibiaxial, planar, and volumetric. Before importing the data, the uniaxial engineering stress-strain data obtained from experiments were filtered during using a zero-phase second-order filter to eliminate noise. During this setup, it is critical to define the material as isotropic instead of anisotropic, as the anisotropic hyperelastic models are far more complex and necessitate additional material test data [82]. While the isotropicity of the material is provided as an assumption in general cases, the TPU material was specifically confirmed to be isotropic as discussed in the material characterization section. Details of material model evaluation using Abaqus are as described in Appendix. B.

The test data were then fitted to attain coefficients for the four most commonly used hyperelastic material models: third-order Ogden, Mooney-Rivlin, second-order polynomial, and Neo-Hookean models [83]. The resultant material coefficients of the material models and the respective root mean squared error are as summarized in Table. 3.2.

Table 3.2: Summary of constitutive hyperelastic models, their respective coefficients, and the fitting errors attained from the evaluation of post-processed uniaxial test data.

Constitutive Model	Material Coefficients				Fitting Error
	Deviatoric Terms			Volumetric	
Ogden (N=3)	μ_i	α_i	-	D	2.8723 E-02
	-2.5359	1.6269		0	
	1.0806	2.4824		0	
	3.7527	0.6109		0	
Mooney-Rivlin	C_{10}	C_{01}	-	D_1	16.17
	0.4705	0.6204		0	
Polynomial (N=2)	C_{10}	C_{01}	-	D_1	5.0212 E-03
	0.8971	0.2342		0	
	C_{20}	C_{11}	C_{02}	D_2	
	1.849 E-04	3.3015 E-02	-0.2433	0	
Neo-Hookean	C_{10}	C_{01}	-	D_1	113.3
	0.6621	0		0	

Stress-strain curves were then recreated using the material models and compared with the original uniaxial tensile test data, as shown in Figure. 3.11. Overall, third-order Ogden and second-order polynomial models provided a precise estimation of material behavior across all strain range. Mooney-Rivlin model provided the best estimation at a low strain range of less than 100 % strain, but failed to contain hyperelastic behavior at higher strain ranges.

Note that the volumetric coefficients of all material models are 0, which arises from the incompressible material assumption. Hyperelastic materials such as TPU are mostly considered incompressible or almost-incompressible as supported by previous works [78, 80, 81, 84], which simplifies the volumetric terms of the constitutive models (i.e. the D_i terms in equations (3.5) and (3.6)). To confirm that the TPU material is indeed incompressible or almost-incompressible, the transverse strain of the tensile specimen was measured with respect to the axial strain during the uniaxial test. The Poisson's ratio was determined to be 0.4 at high strain ranges and 0.45 at small strain ranges.

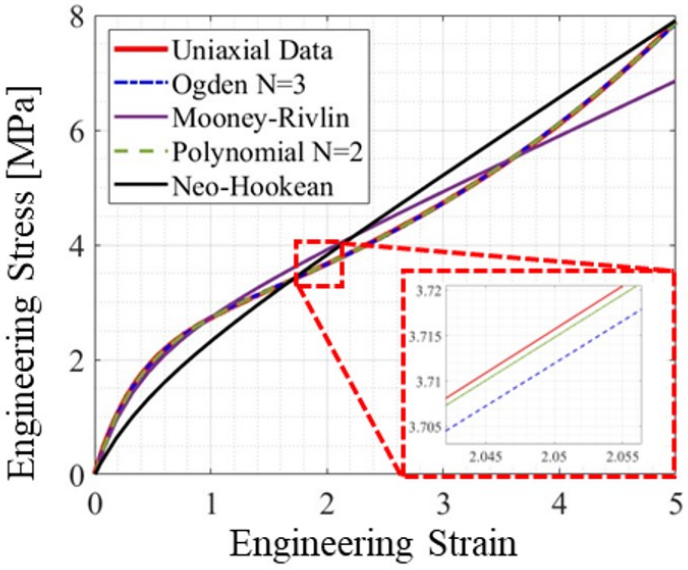


Figure 3.11: Stress strain comparison of hyperelastic models with the original data.

3.3.2 FEM Simulation Setup

In Finite Element Methods, it is generally preferred to minimize the complexity of simulation models in order to reduce computational costs. The ideal simulation model should be set to strike a balance between the simulation accuracy, which requires a certain level of complexity, and the computational efficiency requiring model simplicity. However, conventional SPAs often require full 3D numerical simulation models due to their complex shapes, leading to increased computational costs. Previous studies have shown that numerical simulations of SPAs could take several days to complete [85]. While this is significantly inefficient, this is an unavoidable issue with conventional SPAs due to their intricate shapes.

The newly developed TPU-MBSPAs, which can also be designed in various shapes and sizes depending on the desired motions in varied applications, therefore necessitate a careful consideration when setting up the FEM simulations for the same reason. To maximize the efficiency of executing numerical simulations on TPU-MBSPAs, TPU-MBSPA layers were designed in circular shapes. This allows the numerical simulation model of TPU-MBSPA to be greatly simplified via model reduction to a 2D axisymmetric model. This simplification

to an axisymmetric model offers an efficient alternative to the computationally intensive full 3D models.

Upon numerous improvements, the following list provided the key features required to stably formulate a 2D axisymmetric model and has resulted good estimation of TPU-MBSPA performance. Specific details of the simulation setup are described step by step in Appendix. C:

- To formulate an axisymmetric model, a part was created in Abaqus using the *Axisymmetric deformable* model feature. This feature enables a 2D cross-section to be designed.
- The cross-section of the TPU-MBSPA is only dependent on the diameter and the thickness of the layers. Specifically, the x-direction dimensions are dependent on the radius of the layers, and the y-direction dimensions are dependent on the thickness of the layers. For this study of 5-layer TPU-MBSPA, the dimensions were:
    1. radius r_{TPU}: 10 mm
    2. thickness t_{TPU}: 0.152 mm
    3. r_{Insert}: 8.5 mm
    4. t_{Insert}: 0.08 mm
    5. t_{Paper}: 0.1 mm
- The default Poisson's ratio of incompressible material is 0.475 in Abaqus/Explicit. While this is near-incomrepssible, Poisson's ratio of 0.5 (fully incompressible) diverges due to the limitation of Abaqus/Explicit. To avoid this issue:
    1. Option 1) Increase Poisson's ratio closer to 0.5, such as 0.495. Using this approach, however, requires volumetric hyperelastic coefficients.
    2. Option 2) Use hybrid mesh formulation using Abaqus/Standard, in which case the fully-incompressible material simulation is enabled.
- Define step increment using *Static,General* procedure to attain quasi-static process results
- Apply *Encastre* boundary condition at the bottom surface to fixate one end of the TPU-MBSPA
- Apply internal pressure load with desired magnitude, using ramp function to ensure linear quasi-static process

The 2D cross-sectional design of the 5-layer TPU-MBSPA for axisymmetric simulation is as shown in Figure. 3.12 a). The reference point denoted *RP* locates the tip of the TPU-MBSPA used to log maximum actuator displacement. The vertical axis is the axis of revolution for this axisymmetric model. This implies that the results attained in this cross-section are considered the same throughout the entirety of TPU-MBSPA. An example of the simulation result is as shown in Figure. 3.12 b), which can be revolve-swept for better visualizations, as shown in Figure. 3.12 c).

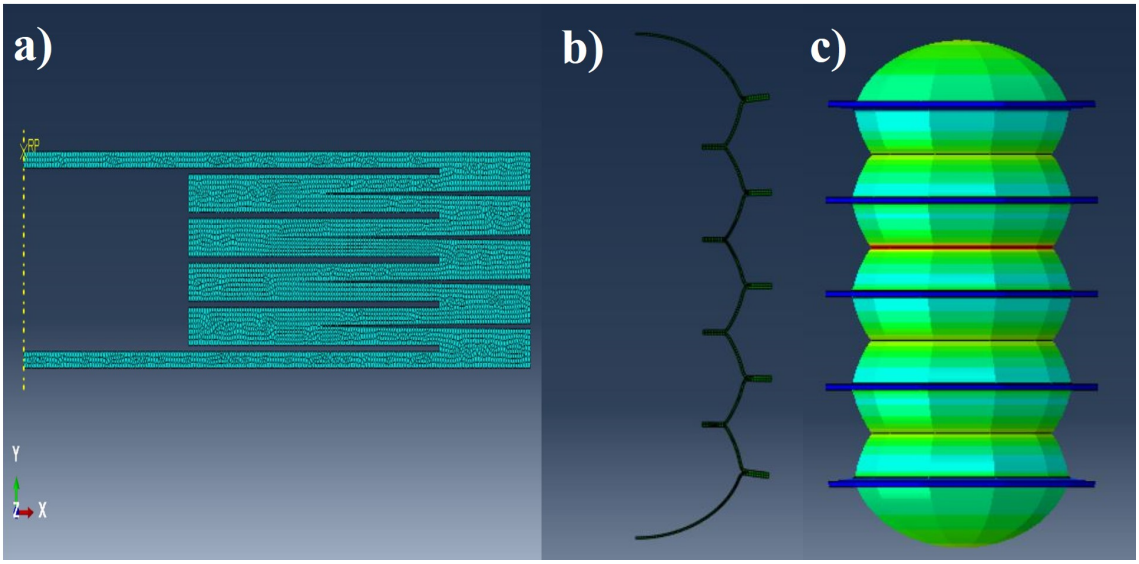


Figure 3.12: Samples of intermediate stages during FEM model setup. a) The meshed 2D axisymmetric cross-sectional model of 5-layer TPU-MBSPA. b) Result of the axisymmetric deformation simulation. c) Revolve-swept axissymetric model for better visualization

3.3.3 TPU-MBSPA Estimation Results and Characteristics

For purposes of studying the expansion behavior of TPU-MBSPA and validating the simulation data, a linear displacement test setup was configured using a desktop pressure controller (MFCS™-ez; Fluigent) and a uniaxial force displacement machine (UniVert; CellScale). As shown in Figure. 3.13, a customized two-piece test fixture was fabricated using Fusion Deposition Modeling (FDM) 3D printer (i3 Mega S; Anycubic) using Polylacic Acid (PLA) and attached on the UniVert system. The fixture was designed with linear guide rails which prevented any off-axis motion and kept the expansion of the TPU-MBSPA linear along the axial direction.

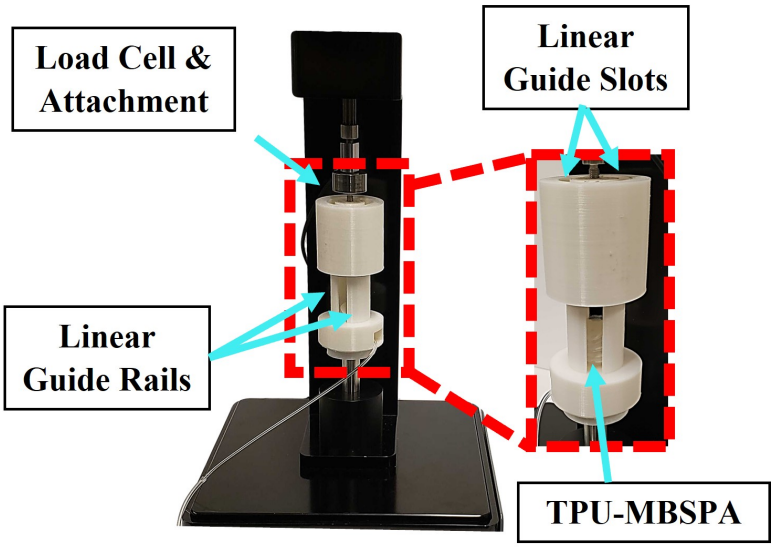


Figure 3.13: Automated test setup for attaining quasi-static expansion response of the 5-layered TPU-MBSPA.

The pressure controller was interfaced through MATLAB to control the pressure output and log the data directly into the MATLAB workspace for data analysis. The UniVert system was set to output system time, displacement, and force data, which were synchronized with the pressure data via a custom MATLAB script. To observe quasi-static linear performance of TPU-MBSPA, a staircase pressure input from 0 to 40 kPa with a 1 kPa step increment was applied. The load cell of the UniVert system was used as a feedback device to simulate the non-blocked, impedance-free linear displacement. To do so, a force threshold of 0.1 N was used to detect the expansion of the actuator such that when a force of more than 0.1 N was applied to the load cell, the equipment automatically displaced upwards to let the TPU-MBSPA expand further. The quasi-static displacements were logged at steady state in which the force applied to the load cell had stabilized below 0.1 N. A 5-layered TPU-MBSPA with the total initial retracted thickness of 2 mm was used in this test. As shown in Figure. 3.14 a), the FEM results using third-order Ogden model provided the closest visual resemblance to the fabricated actuator at fully expanded state.

The quasi-static linear displacement data of the 5-layered TPU-MBSPA along with the displacement results from the simulation are shown in Figure. 3.14 b). Even though Ogden models are not preferable in modeling with limited material test data, both the third order Ogden model and the Mooney-Rivlin model resulted in solid estimation of the TPU-MBSPA expansion behavior. Though Mooney-Rivlin model had overall fitting error

of 16.2, as shown in in Table. 3.2, it was able to provide a good estimation of actuator expansion because the maximum strain observed in the simulation was 87 percent, in which the Mooney-Rivlin model lied closely with the uniaxial data. However, the experimentally measured linear displacements were generally lower than the simulated results, in which the differences were non-linear throughout the pressure range. The discrepancy was mainly attributed to the internal stiction of TPU-MBSPA, the compression force exerted by the test fixture, and insufficient material test data.

During the expansion of TPU-MBSPA, it was observed that certain pouches did not expand until after certain pressure was reached. Such behavior is analogous to stiction in motors, which adds nonlinearity to the system. In addition, a constant compression force of 0.1 N was applied to the TPU-MBSPA throughout the experiment as a method to detect expansion, unlike the frictionless and blockage-free simulation environment. Though 0.1 N is a minimal force, it had a greater impact on impeding the displacement of TPU-MBSPA at a lower pressure input compared to a higher pressure input, further contributing nonlinearity to the response. Lastly, the simulation model was based on the uniaxial tensile test. The addition of equibiaxial and pure shear test data would fully define the material model and improve the accuracy of the simulation results.

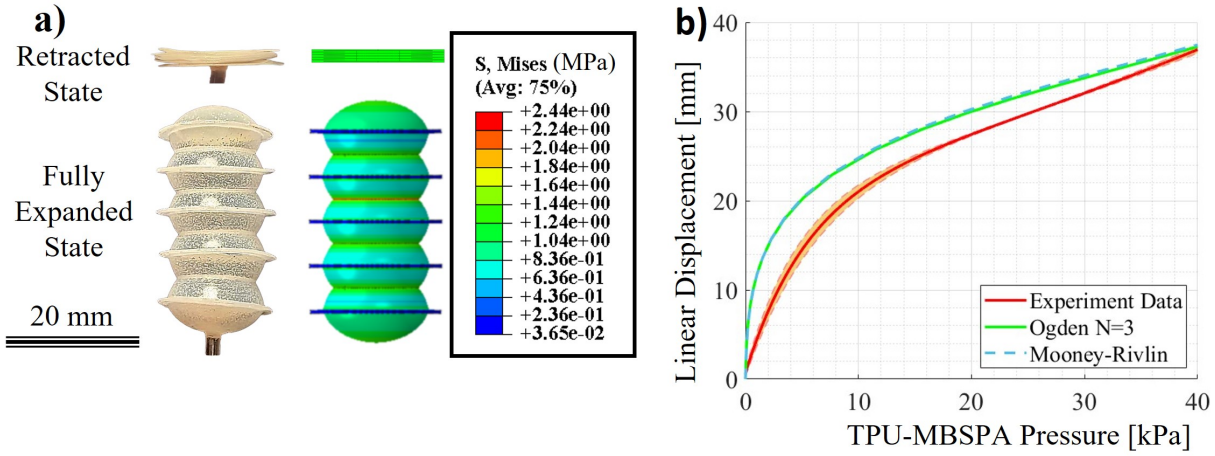


Figure 3.14: The comparison of the quasi-static expansion behavior of the simulation and the experiment. a) To-scale visual comparison of the fully expanded state of TPU-MBSPA during the experiment and the simulation. b) Pressure-displacement estimation acquired from the FEM simulation compared with the experiment linear displacement data.

To characterize the force output of the 5-layered TPU-MBSPA, the UniVert system was configured to provide a 5 mm displacement increment on command. At each displacement increment, the TPU-MBSPA was applied with staircase pressure input from 0 to 40 kPa with 5 kPa step increments. The output force at each pressure increment was measured through the load cell once the force output had stabilized. As shown in Figure. 3.15 a), TPU-MBSPA was able to output a maximum blocked force of 7.8 N at 40 kPa. These quasi-static force output results also revealed a linear relationship between the pressure input and blocked force outputted by the TPU-MBSPA at fixed displacements, with a decreasing slope at each displacement increment. This is because, as the unimpeded displacement increased, the TPU-MBSPA was allowed with further axial expansion. This allowed more room for radial expansion where a large portion of the pressure increment was utilized to expand TPU-MBSPA radially, instead of being used to produce more force. Therefore, the force output efficiency decreased as the blocked displacement increased.

In certain applications, TPU-MBSPA may be needed to deliver a higher force output. An intuitive approach would be to increase the surface area of the inflating chamber, in which the desired force can be achieved with the same operating pressure range. An alternative method would be required for applications where geometric constraints exist. To test this approach, the surface area of the inflating chamber and the overall size of the TPU-MBSPA were kept constant, while the thickness of the TPU-MBSPA TPU layer and the operating pressure range were doubled. As shown in Figure. 3.15 b), TPU-MBSPA was able to output an increased force output of 16.1 N at 80 kPa, and the results implied that linear extrapolation can provide a force output estimate using pressure input, should the application require higher or lower force output.

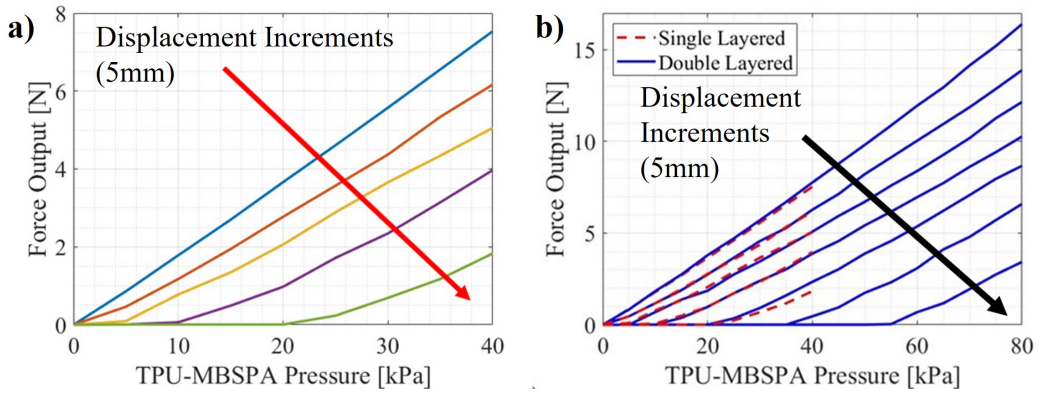


Figure 3.15: Quasi-static blocked force output of TPU-MBSPAs when using a) single TPU-layer, and b) doubled TPU-layer thickness.

3.4 Additional Applications of TPU-MBSPA

The fundamental principle of TPU-MBSPA involves the displacement of fluid into the actuator, causing an increase in the internal pressure, which induces hoop stress onto the structural TPU layers. The linear displacements are attained as a consequence of the hyperelastic strain of the TPU material. Applying the same principle but by simply altering the sequence of the operation, TPU-MBSPA can also serve as a displacement sensor analogous to a linear potentiometer. To acquire this, the TPU-MBSPA can first be made into a closed system with a predetermined initial internal pressure. Upon exertion of external forces which compresses the TPU-MBSPA, the internal pressure of TPU-MBSPA increases as a result. The magnitude of this linear displacement can be determined by the correlation of the increase in the internal pressure with respect to the amount of compression. This aspiration has been investigated in collaboration with the NRE lab, for the purpose of detecting downward movement and pistoning in transtibial prosthetic sockets application [86]. Note that this was a collaborative project, my contributions include: project conceptualization, pioneering sensor design and fabrication, assisting with test setups and methods, and manuscript editing. The following subsections provide a synopsis on the background, methods, and results of applying TPU-MBSPA as displacement sensors.

3.4.1 Background

Diabetic foot complications are a leading cause of lower extremity amputations, placing a significant burden on healthcare systems worldwide. Most lower-limb amputations are preceded by foot ulcers in diabetic individuals. A large number of these individuals also experience peripheral neuropathy, a condition which adds additional challenges for monitoring the health of the residual limb.

Optimizing socket fit is crucial to prevent skin breakdown and improve mobility for individuals with amputation. Poor prosthetic fit can lead to discomfort, skin ulceration, increased risk of falling, and dissatisfaction among users. However, the residual limb is subject to severe volume fluctuations especially in the early stages of post-amputation. These residual limb volume fluctuations, particularly during the early period of limb maturation, contribute to poor prosthetic fit which may lead to further complications caused by pistoning and downward movement. “Pistoning” refers to the vertical displacement of the residual limb within the socket, indicating proper suspension and fit. “Downward movement” occurs when the residual limb drops deeper into the socket over time, often due to limb volume loss. Both pistoning and downward movement can cause discomfort, skin ul-

ceration, and deep tissue injury. Many individuals with amputations report dissatisfaction and pain during prosthetic use due to inadequate fit.

Despite the importance of acknowledging improper socket fit due to the severe complications it may cause, the condition of the residual limb and the management of the volume fluctuations are typically accounted manually by the users, by manually adjusting the number of liners and socks in the socket. Since many amputees have peripheral neuropathy, relying on the amputees to self-manage these complications is illogical considering that the impaired sensation and proprioception are what led to diabetic foot ulcers at the first place. With the increasing prevalence of diabetes, the need for better fitting prosthetic sockets and alternatives is being highlighted. Although advancements in automatic dynamic socket adjustment are being explored, cost and complexity may inhibit automatic adjusting socket adoption.

Various sensor technologies, such as force-sensitive resistors (FSR) and activity monitors, have been developed to monitor pressure and shear at the residual limb and socket interface. However, they have limitations in terms of long-term use, durability, and drift. Textile and microfluidic technologies offer potential solutions, but their suitability for prosthetic settings is yet to be fully explored. Existing developments have also overlooked the vertical displacement associated with pistoning and downward movement. It is essential to have a sensor that can detect and measure the severity of these movements, that can assist users with impaired abilities to acknowledge when complications occur. Long-term sensor performance, reusability, and durability remain important considerations, as does minimizing disruption to the socket-residual limb interface. To account for these considerations, a multi-layered torus-shaped layered-donut balloon (LDB) was developed using the same fabrication and working principle as the TPU-MBSPA, for use of monitoring and detection of pistoning and downward movement of the residual limb within the socket.

3.4.2 Methods and Results

For accompanied use with the pin-locking or vacuum suspension prosthesis system, a torus shape LDB was adopted, as shown in Figure. 3.16. Consultation with a senior prosthetist was included in the design loop, such that the fabrication and implementation of the LDB displacement sensor can be customized and fabricated without expensive specialty machinery, focusing on integrating into the prosthetist's workflow during socket fabrication. The torus shape was adopted for accompanied use with the pin-locking or vacuum suspension prosthesis system. The pin lock fits through the hole of the LDB sensor. It is intended for prosthetic users who may have difficulty monitoring the health of the distal end of their residual limb due to reduced sensation.

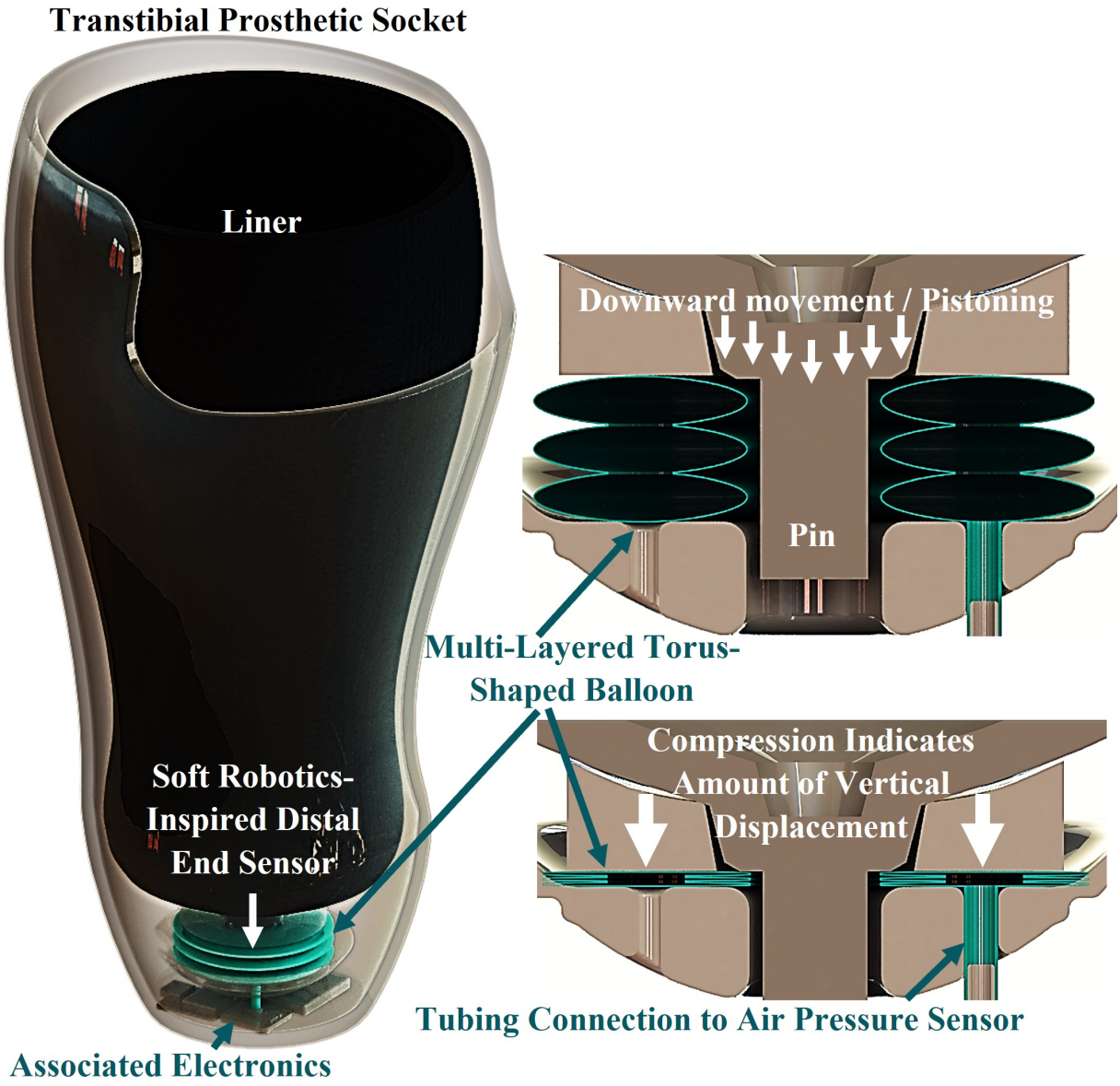


Figure 3.16: Overview of the soft robotics-inspired multi-layered torus-shaped displacement compression sensing system for detecting downward movement and pistoning in prosthetic sockets [86].

For testing and characterization purposes, a total of six LDBs of varied sizes and thicknesses were manufactured in the initial investigation. Three of the six LDBs were designed with smaller outer diameters of 46 mm, each manufactured with varied thicknesses; one with single-layered TPU material (∼150 mm), one with double-layered TPU (∼300 mm), and one with triple-layered TPU (∼450 mm). Similarly, the other three LDBs had single, double, and triple-layered TPU material, with a bigger outer diameter of 54 mm. This is as summarized in Figure. 3.17 a). All LDBs used in this study, as shown in Figure. 3.17 b), were fabricated using the same manufacturing method and processes as TPU-MBSPA, as shown in the simplified schematic detailing the fabrication process shown in Figure. 3.17 c).

As directed by the prosthetist, the main objective of the LDB sensor was to detect downward movement and pistoning of up to half an inch (or 12.7 mm) while imparting less than 20 kPa contact pressure to the distal end of the residual limb. In order to provide an automated and reliable test method for characterizing the proof-of-concept LDB, mechanical benchtop tests were set up using the Univert tensile testing machine, as previously used for TPU-MBSPA. Additional components were fabricated using FDM 3D printing with PLA material, to modify the attachment to the tensile testing machine.

The Univert system was set up to monitor both the vertical displacement as well as the applied forces. To ensure a total of 12.7 mm vertical displacement, the LDB was first inflated to a height of 12.7 mm, in which the minimal contact force onto the load cell was used as an indicator. While the LDB was compressed at a rate of 0.21 mm/s (or 12.7 mm/min), the load cell was monitored to ensure that the force limit of 50 N was not exceeded. This was to indicate that the maximum acceptable pressure has been reached. The compression rate was selected to accurately determine the capable vertical displacement range of LDB, without inducing impulse, thus, simulating standing or static positioning.

Additional vertical displacement tests were conducted to determine the optimal number of layers for LDB. As shown in Figure. 3.18 a), a linear relationship was determined between the internal pressure of the LDB sensor and the external pressure applied at the distal end. The two and three-layered LDB had above 0.99 R^2 coefficient of determination, whereas the five-layer had above 0.98 R^2. The LDB demonstrated decreasing stiffness with increasing layer count, as shown in 3.18 b). The 2-layer, 3-layer, and 5-layer LDB reached an externally applied pressure of 20 kPa at 7 mm, 7.1 mm, and 7.4 mm vertical displacement, respectively. In all three cases, the applied pressure exponentially increases after 25 kPa with increasing vertical displacement after 7.5 mm.

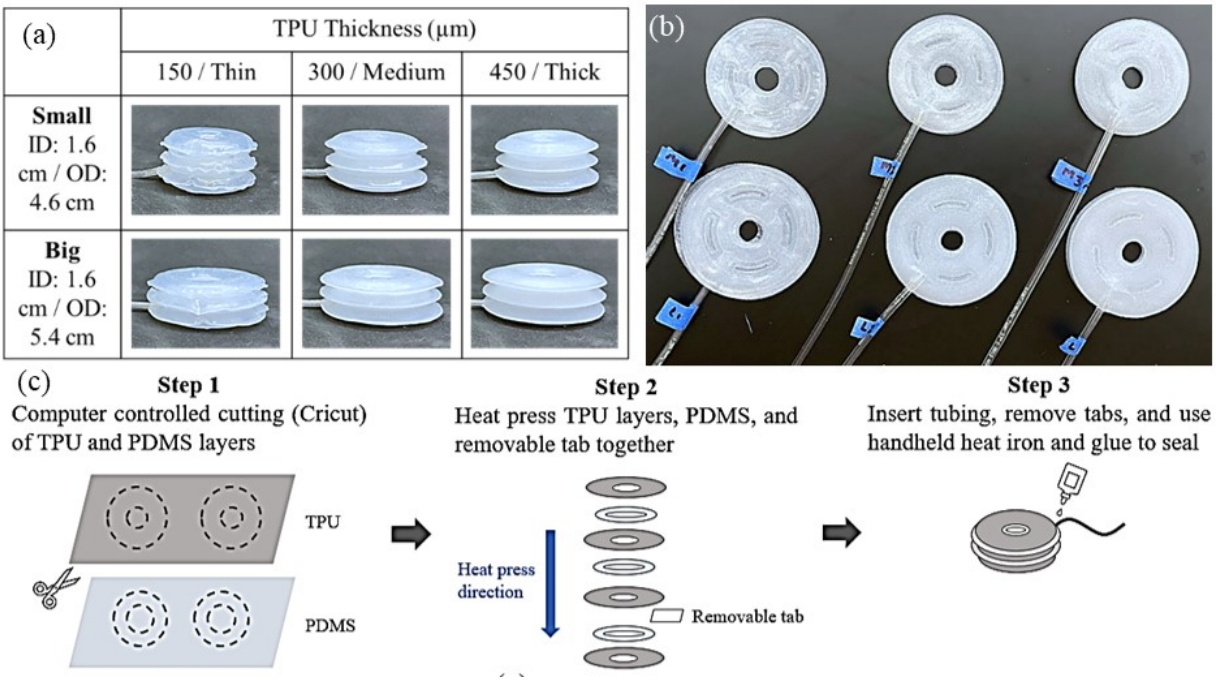


Figure 3.17: (a) The six LDBs manufactured for testing. (b) Top-down view of the manufactured LDBs. (c) Schematic of the LDB fabrication process [86].

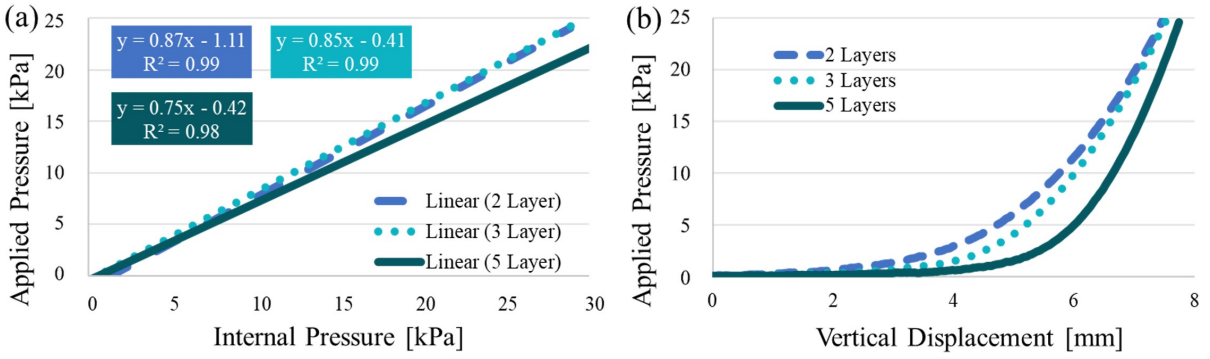


Figure 3.18: Results from vertical displacement range testing to characterize the effect of layers on LDB: (a) linearity plot. (b) Applied pressure vs. vertical displacement plot [86].

3.4.3 Conclusion and Limitations

In this preliminary investigation, a novel soft robotics-inspired multi-layered torus-shaped balloon sensor was invented to measure the downward movement of the residual limb within a socket. This layered donut-shaped balloon sensor was designed and fabricated using the same approach developed for TPU-MBSPA and has exhibited promising initial benchtop testing results. While in this proof-of-concept the LDBs could not attain a target vertical displacement of 12.7 mm while maintaining applied pressure below 20 kPa, this preliminary study successfully demonstrated the potential of using TPU-MBSPA as an LDB displacement sensor. Though in real-world applications, a 12.7 mm displacement may not be necessary, since the sensor would likely prompt the user to wear additional socks well before reaching this threshold. Nevertheless, a full-scale displacement span of 12.7 mm would remain a valuable feature.

Several limitations should be considered, given the proof-of-concept study only focused on LDB characteristics. While effective for initial validation, the testing apparatus cannot fully simulate human gait. Firstly, it cannot create the residual limb's bell-clapping motion (horizontal movement). The residual limb and the liner are soft and compliant; however, the testing apparatus's surfaces contacting the LDB were rigid. Compliance of the interface was missing during this study and may heavily influence measurement noise and confidence. Lastly, the LDB itself cannot reach half an inch (12.7 mm) vertical displacement without imparting pressure/applied reaction force too high to be considered safe onto the distal end of the residual limb. One solution may be adding a pneumatic capacitor to the system, reducing its stiffness. Further bench testing, case studies, and clinical trials will need to be conducted to determine the efficacy of the LDB sensor during real-world use.

Unlike the TPU-MBSPA, FEM simulation of the LDB sensor would be a challenging task necessitating multiphysics modeling and simulation. With TPU-MBSPA and with the conventional FEM in general, known loads such as internal pressures, forces, and boundary constraints are applied to the model. With known loads, the material strain is dependent on the material properties, in which the resultant displacement and expansion can be numerically estimated. This order changes when TPU-MBSPA is used as a displacement sensor. While the input now becomes the vertical displacement or the external load compressing the material, estimating the resultant change in pressure must include the compressibility of air, requiring Computational Fluid Dynamics simulation on top of the FEM.

Chapter 4

Soft-Rigid Hybrid Revolute and Prismatic Joint Actuators

This chapter entails the design philosophy and rationale behind adopting Soft-Rigid Hybird (SRH) robotics approach comprised of synergistic integration of rigid components with the previously developed TPU-MBSPA toward manipulation applications, followed by the invention of Soft-Rigid Hybrid Revolute Joint Actuator (SRH-RJA) and Soft-Rigid Hybrid Prismatic Joint Actuator (SRH-PJA). A brief literature review is first provided to highlight the benefits and the prominent disadvantages of the existing technologies, followed by sharing of the details and reasoning of specific design features. Upon extensive characterization of both joint actuators, a proof-of-concept three-point SRH robotic gripper is designed and studied.

4.1 Conventional Soft Robotic Grippers

Leveraging the ability of soft actuators to safely manipulate delicate objects via conforming to irregular shapes and sizes, soft manipulators such as soft grippers have been developing quickly toward delicate object handling [87]. There exist numerous types of soft grippers made available with the rising efforts of soft robotics research over the years. While the mechanisms and the gripper methodologies are dependent on the functionality required in specific applications, conventional soft pneumatic actuators (SPAs) are one of the most commonly reported soft grippers [42, 88]. Conventional SPAs fundamentally have low inertia, fast response, and a wide range of force output and technologically they can be

fabricated easily with low cost, hence are favorable for iterative research purposes [15, 32, 89]. With variable stiffness and its capability to provide compliant gripping for the safe handling of delicate objects, many researchers adopted SPAs as end-effectors in harvesting applications [87].

However, soft robotic systems comprised solely of conventional SPAs rely on predefined trajectories, have limited payload capabilities, suffer from oscillations, and lack structural support [12, 13]. Moreover, SPAs are susceptible to cuts and punctures, and hence extremely vulnerable to any sharp objects [90]. In applications such as berry harvesting, environmental factors such as thorns, sharp branches, and UV radiation puts the practicality of soft grippers at risk. For soft robotic systems to deliver a valid impact to the targeted industry, practical considerations must be incorporated [91].

4.1.1 Existing SRH Approaches and Limitations

In efforts to overcome the disadvantages of soft pneumatic grippers, the incorporation of rigid structural components [7, 92] has been proven to be effective in providing improved performances [93] and has opened doors for new types of SRH embodiment. One class of SRH systems incorporates monolithic SPAs with rigid components [94]. An example of SRH robotic approach using monolithic SPA is as previously shown in Figure. 2.7 b). SRH grippers comprised of conventional SPA and rigid components have achieved increased tip force output, allowing for a wider range of actuator stiffness, and shortened actuation times [43, 55, 95]. While the fabrication is straightforward and repeatable, monolithic SPAs have fixed bulky sizes. Their bulky nature fundamentally limits the addition of rigid components, especially when trying to provide an enclosure or protection elements to the soft actuators, completely exposing them to harsh environments.

Another class of SRH systems utilizes blow-molded bellow-type SPAs as joint actuators driving the linear and/or angular movements of the rigid linkages [54, 96]. An example of this is as previously shown in Figure. 2.7 a). Often incorporated with rigid hinges, the kinematic trajectory is always consistent and hence repeatable [97]. However, blow-molded bellow actuators require high pressure input to achieve practical displacements and hence energy inefficient [98]. The nature of the fabrication method also results in a fixed bulky volume, even at the fully retracted state using vacuum pressure. As an alternative approach to blow-molding, TPU-MBSPAs utilize a 2D manufacturing approach using thin textiles, polymer films, and thermal adhesives. As previously shared in Chapter. 3, the resultant MBSPAs have minimal thickness when fully retracted, provide an excellent retraction-expansion ratio, and can be easily stacked on top of one another. These features make

them well-suited to be integrated into small spaces and less susceptible to spatial constraints [41]. SRH embodiments with TPU-MBSPAs would allow the system to be modular and help to attain dexterous manipulation.

While there had been investigations on SRH structure using MBSPA as soft joints driving the attached rigid links [99], methods to utilize only one single MBSPA to achieve motions equivalent to a revolute joint of a rigid robot have not yet been explored. In addition, the current existing methods require 2 or more MBSPAs to provide a multi-Degrees of Freedom (DOF) such as roll and pitch motion [100, 101], in which the rotation axes are often unconfined with a lack of rigid reinforcements [41, 100]. Moreover, limited information is available in terms of the durability, performance repeatability, dynamic response of these MBSPA-enabled SRH structure, and solutions to practical considerations such as protection methods from the workspace environment.

4.1.2 Project Objectives

In this project, the goal is to develop and share a novel method for attaining a 1-DOF SRH revolute joint actuator enabled via synergistic integration of rigid components and a single TPU-MBSPA. This investigation is extended to develop toward delicate object handling applications for demonstration purposes. To contribute further, this project is also extended to study a 1-DOF SRH prismatic joint actuator. The key rationale behind adopting the proposed hybrid approach lies with the specific benefits each acquirable from soft robotics and the rigid counterparts. Specifically, soft actuators allow the system to leverage the compliant nature of soft robotics to enable the a wide range of variable joint stiffness without a complex control scheme. With traditional robotics approach, this would require an expensive sensorization, computation, and control. In addition, structural stability is acquired with rigid links, which are critical for repeatability and strength. Hence, the proposed SRH system would allow for more efficient displacement characteristics, improved force output, and better resilience against external loads compared to purely-soft system or similar types of SRH configurations.

4.2 Soft-Rigid Hybrid Joint Actuators

4.2.1 Design of Soft-Rigid Hybrid Revolute Joint Actuator

The 1-DOF Soft-Rigid Hybrid Revolute Joint Actuator SRH-RJA is comprised of the TPU-MBSPA utilized as a rotary actuator driving the angular displacement of the attached rigid

components. As illustrated in Figure. 4.1, the rigid components are divided into two pieces, namely the rotary part and the stationary part. The stationary part serves as the base and can be securely mounted on a surface such as a base plate or an optical table, and the rotary part is designed to rotate with respect to the stationary part. These rigid parts are each attached to the top and the bottom surface of the TPU-MBSPA using glue adhesive specialized for attaching elastomers (LOCTITE 4902, Henkel AG & Co. KGaA), hence actuated via the expansion and retraction of the attached TPU-MBSPA. With a pin-hinge fixating the location of the axis of rotation, the linear expansion of the TPU-MBSPA is forced to curve in an arc, providing the angular displacement of the rotary part. For the presented SRH-RJA specifically, the range of angular motion is designed to be limited within [0 90] degrees, which requires the TPU-MBSPA to expand an arc length of 21 mm. To ensure this arc length is sufficiently provided by the TPU-MBSPA at low internal pressure, a 9-layered TPU-MBSPA is adopted.

To acquire real-time angular displacement data of the 1-DOF SRH-RJA, a capacitive bend sensor (1-Axis Soft Flex Sensor, Nitto Bend Technologies) is integrated throughout the internal cavities of the rotary and stationary components. This capacitive bend sensor is preferable over the resistance-based flex sensor because unlike the resistance-based flex sensor the capacitive bend sensor does not require manual calibration procedures or an additional voltage-divider circuit. This is possible because the angle readings of capacitive bend sensors are only dependent of the integrated angle between the two ends of the sensor. Hence in this case, the sensor reads 90 degrees when SRH-RJA is at the fully retracted state (0-degree angular displacement), and reads 0 degrees when SRH-RJA is at fully extended state (90-degree angular displacement), which are accounted for in the software.

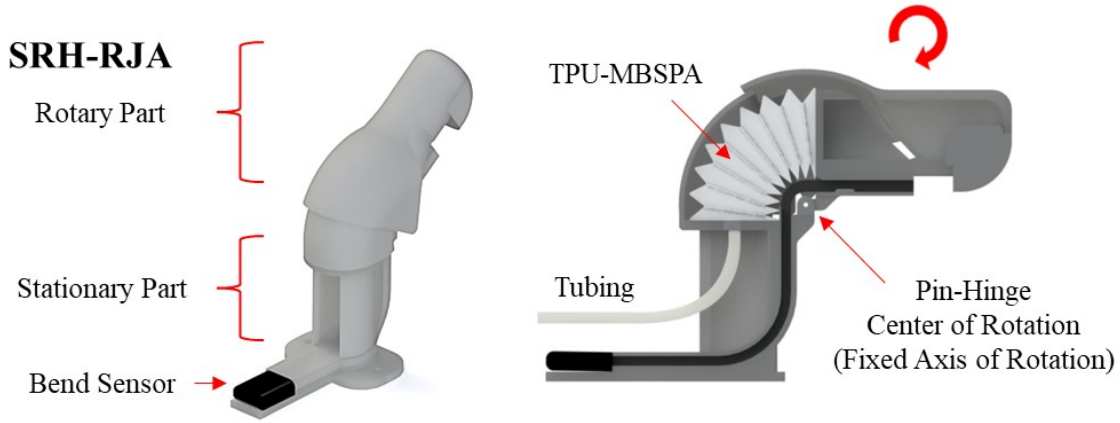


Figure 4.1: The schematic entailing the key components of SRH-RJA.

Preliminary force output investigation of the joint actuators revealed that the SRH-RJA is susceptible to radial bulging. Radial bulging is a phenomenon often exhibited in systems where soft actuators are utilized to provide angular displacement and/or torque [102, 103]. Due to the natural compliance of the soft actuator, the actuator has a tendency to adopt the path with least physical impedance. When a certain counteracting force is enacted upon the blockaded TPU-MBSPA attempting to expand further, the TPU-MBSPA prefers to bulge outward in the radial direction rather than staying in its nominal course to increase the applied force. As demonstrated in the preliminary trials shown in Figure. 4.2, this phenomenon of radial bulging not only induces inefficiency to the system, but also the TPU-MBSPA may be malfunctioned depending on the extent of radial bulging. The consequence of not mitigating radial bulging resulted in a large drop in force output at higher blocked angles. On the contrary, results of additional preliminary investigation proved that the effective force output of the system increased drastically when radial bulging is mitigated. Despite this severe negative effect of radial bulging, methods to mitigate this issue has not yet been explored in the literature.

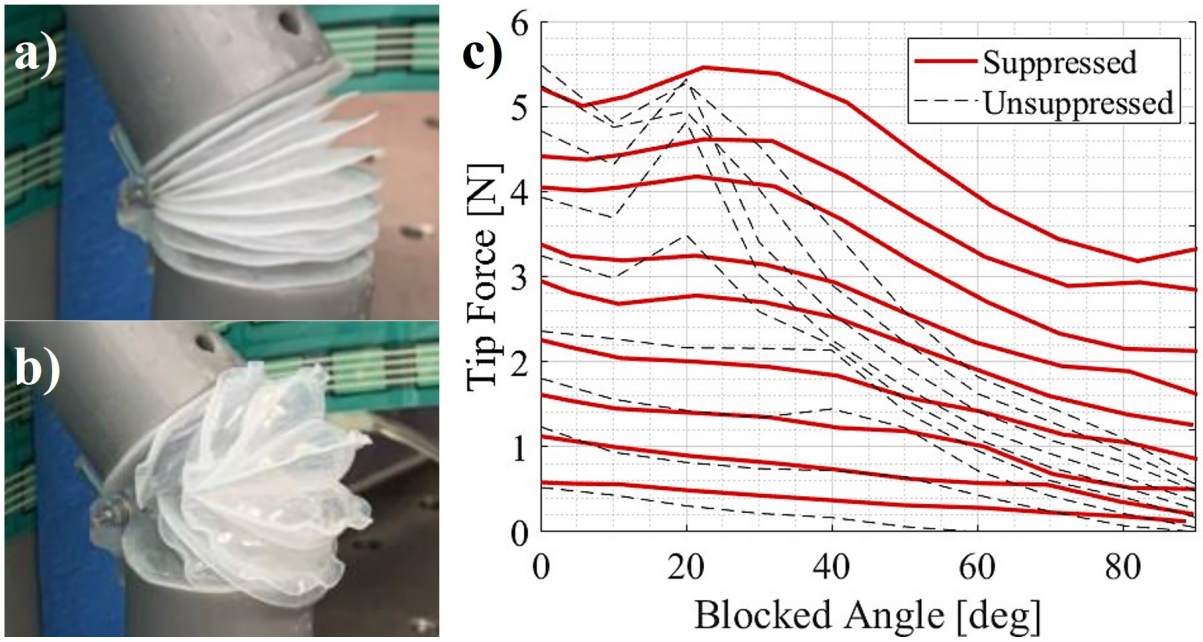


Figure 4.2: a) Nominal operation of TPU-MBSPA in SRH-RJA. b) Radial bulging induced by a large counteracting force. As a consequence of severe radial bulging, the TPU-MBSPA malfunctioned and was not able to retract afterwards. c) Comparison of preliminary force output results when radial bulging is suppressed and unsuppressed.

Aside from the need to provide effective methods for mitigating TPU-MBSPA bulging radially, TPU-MBSPA is relatively delicate and fragile compared to electromechanical motors. Due to the fact that TPU-MBSPA is a type of soft pneumatic actuator, any puncture or damage of the hyperelastic layer is critical for the nominal operation of the joint actuator. Therefore, TPU-MBSPA must be protected from the external environmental factors for the proposed soft-rigid hybrid joint actuator to succeed in practical applications.

Also considering the need to provide protection and the necessity to mitigate TPU-MBSPA radial bulging, two TPU-MBSPA protective casings were designed to account for these practical considerations. The first design is a bio-inspired, armadillo-like multilayered casing method (Figure. 4.3 a). Comprised of 5 casing layers stacked on top of one another, all layers are attached to the SRH-RJA at the pin-hinge such that the center of rotation of all casing layers are fixated and the trajectory curvatures are concentric with the rotary part. With the top and the bottom layers each attached to rotary and stationary parts, the the inter-layers are carefully designed with mechanical latches that activates the movement of the casing such that the TPU-MBSPA is encapsulated throughout its entire range of motion. This casing hence complies to the movement of rotary component with minimal physical impedance, eliminating the need of additional actuation component to move the casing.

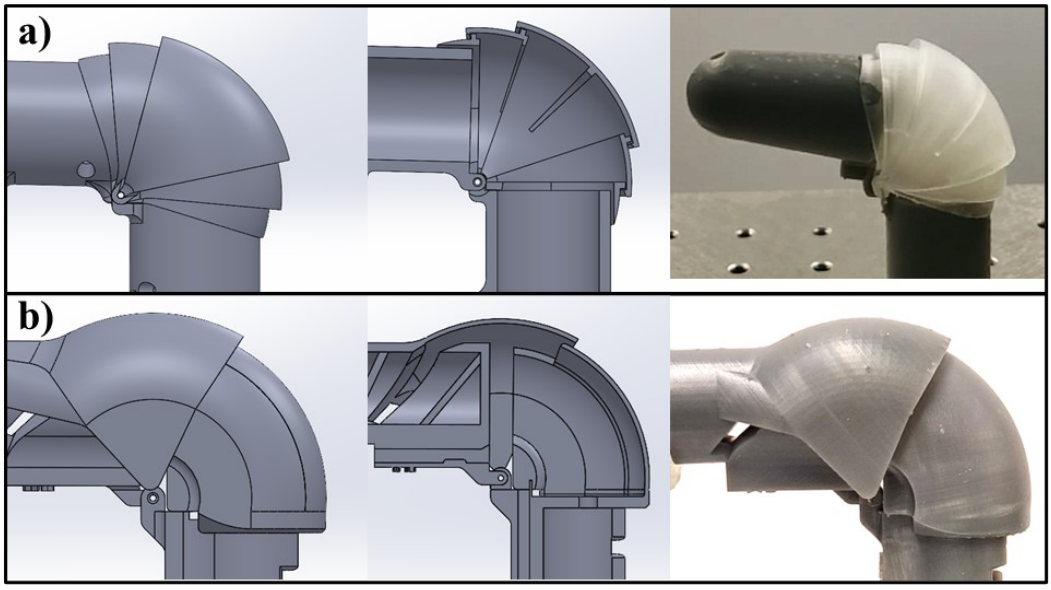


Figure 4.3: The design of the casing methods shown in the right-side view, cross-sectional view, and the fabricated example of: a) Armadillo-inspired casing and b) embedded casing.

The second casing design is similar to the armadillo-inspired casing method, but simplified to two casing layers embedded within the rotary and stationary components. When the joint actuator is fully actuated, the casing layer in the stationary part covers 70 % of the TPU-MBSPA, while the remaining portion is protected by the casing layer in the rotary part. The rotary component is designed with internal cavities that allow the casing layer of the stationary part to slide freely in and out. While both the armadillo-inspired casing and the embedded casing methods worked as intended and deemed effective, the embedded casing approach is adopted due to fewer moving parts and easier assembly.

4.2.2 Design of Soft-Rigid Hybrid Prismatic Joint Actuator

The construction of 1-DOF Soft-Rigid Hybrid Prismatic Joint Actuator is analogous to the rotary joint actuator. As shown in Figure. 4.4, it is comprised of a stationary part and a sliding part, in which the sliding part follows a fixed axis of linear motion as the embedded TPU-MBSPA expands and retracts. Both the sliding and the stationary parts are designed with internal grooves as linear motion constraints, forcing all movements to occur strictly along the axis of linear motion. The sliding component moves along with the expansion of TPU-MBSPA, encapsulating to provide protection through the entire range of linear motion.

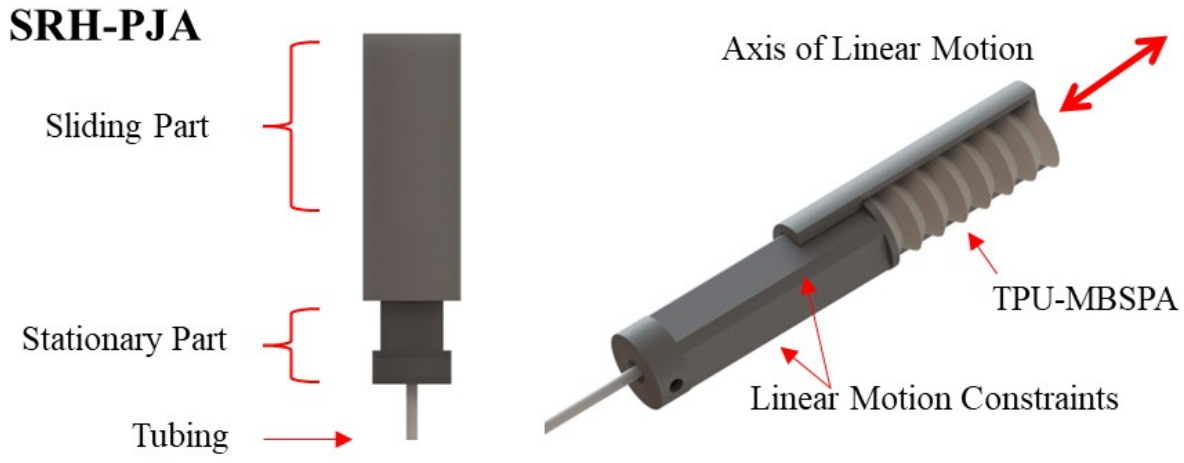


Figure 4.4: The schematic entailing the key components of SRH-PJA.

All rigid components of SRH-RJA and SRH-PJA are 3D printed via the Stereolithography (SLA) resin printer (Form 3; Formlabs). These rigid components are designed such that the TPU-MBSPA is always encapsulated throughout the entire range of motion of the joint actuator to protect the actuators. These encapsulating components are made of photosensitive resin (Tough 2000 Resin; Formlabs), which possess a a tensile modulus of 2.2 GPa and a flexural modulus of 1.9 GPa upon curing with UV light [104, 105]. With an unnotched IZOD impact property of 715 J/m, these rigid components allow the entire joint actuators to be highly resilient against impact, high heat, UV light, and protected from sharp objects.

4.2.3 Quasi-static Displacement Characterization

To investigate unobstructed quasi-static angular displacement output of the SRH-RJA, the stationary part of the SRH-RJA was fixed while the rotary part was allowed to revolve freely during pneumatic pressurization. To incorporate the effect of air's compressibility in the system of interest, all tests were done with air as the medium. To observe the quasi-static angular displacement output of SRH-RJA, a staircase pneumatic pressure input from 0 to 15 kPa with a 0.1 kPa step increment was applied into the TPU-MBSPA. The SRH-RJA was given sufficient time to settle before moving onto the next step increment. The capacitive bend sensor was used to log the angular displacement output throughout the experiments. To minimize the effects of gravity, the axis of rotation was placed perpendicular to the ground. All tests were repeated three times.

The quasi-static angular displacement result of the SRH-RJA is as shown in Figure. 4.5. Note that all pressures referred in this paper are gauge pressures. At 1 kPa input pressure, TPU-MBSPA enabled SRH-RJA provided an average unobstructed angular displacement of 19.8 $\pm$ 0.4 degrees, 59.4 $\pm$ 1.2 degrees at 5 kPa, and reached the desired maximum angle of 90 degrees at 13.1 kPa. To put into perspective, a similar SRH revolute joint utilizing a blow-molded bellow-type soft pneumatic actuator required a pressure displacement of 20 kPa to provide an angular displacement of 70 degrees [97], which also required the internal pressure of the actuator to be over 110 kPa. It is also more efficient compared to the soft pneumatic actuator reinforced with origami shells [106], which required an input pressure range of 30 to 45 kPa to reach 90-degree angular displacement.

The unobstructed linear displacement output of the SRH-PJA was measured with a setup similar to that of the SRH-RJA. To observe the quasi-static linear displacement output of TPU-MBSPA enabled SRH-PJA, a staircase pneumatic pressure input from 0 to 25 kPa with a 1 kPa step increment was applied. A linear potentiometer with minimal friction (PS100; TT Electronics) was used to log the quasi-static unobstructed linear displacement output. The linear displacement characteristic of the SRH-PJA is as shown in Figure. 4.5. At 2 kPa input pressure, the SRH-PJA provided a linear displacement of 10.7 mm, 26.5 mm at 10 kPa, and saturating at 40.9 mm at 24 kPa. Overall, the linear displacement output of the SRH-PJA followed a logarithmic curve, which is commonly observed with bellow-type soft pneumatic linear actuators [41].

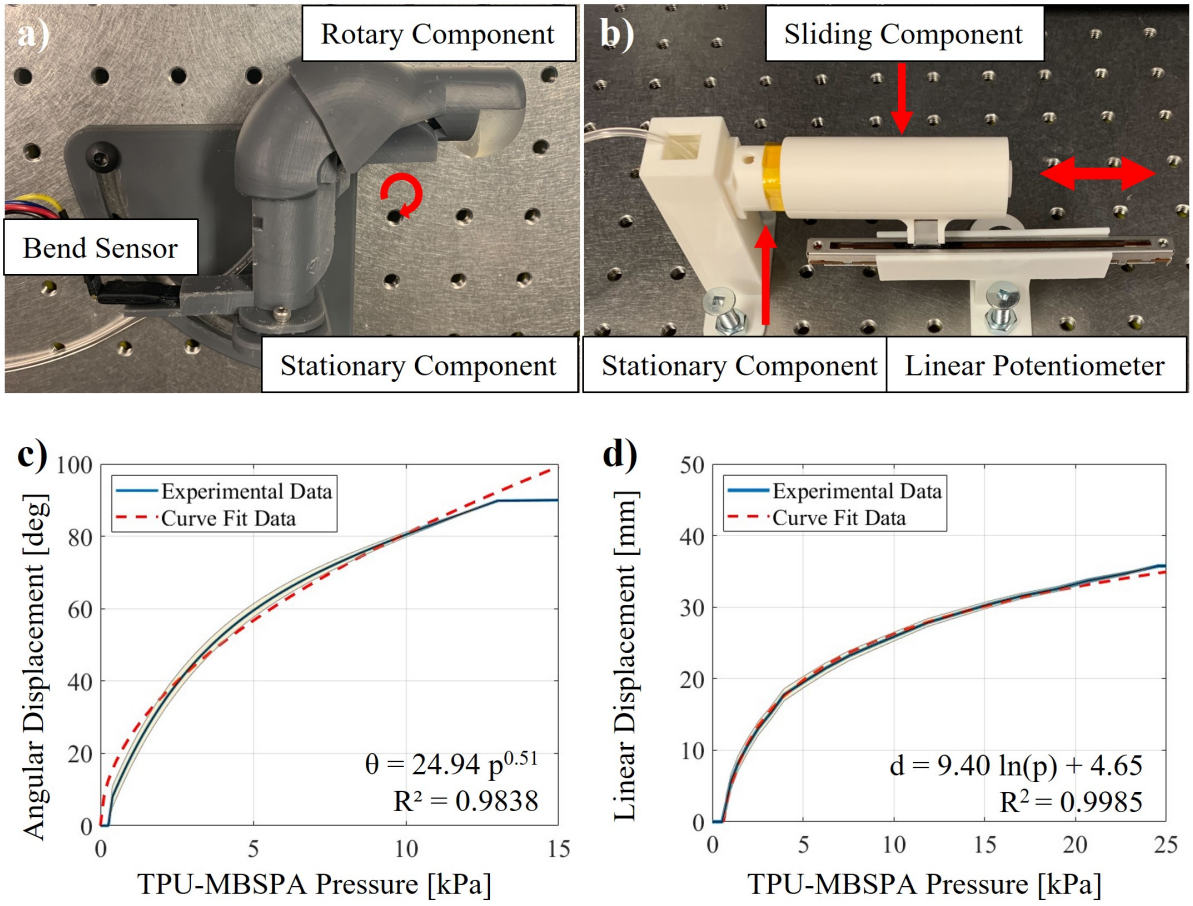


Figure 4.5: The displacement test setup and results of a&c) SRH-RJA and b&d) SRH-PJA.

4.2.4 Dynamic Displacement Characterization

Though quasi-static displacement characterization is commonly reported in soft robotic actuators, it does not convey any information about the dynamic displacement response of the actuators. While speed and actuation time are often reported, they provide limited understanding because the speed of actuation and delay in response are highly dependent on specific experimental conditions such as viscoelasticity and friction. Hence, the frequency response of the SRH-RJA and SRH-PJA was investigated to further enrich the displacement characteristics and to provide an objective way to comprehend the performance of the hybrid configuration.

To cover the entire range of motion a setup was designed to provide 12 mL volume displacement as the input. The setup as shown in Figure. 4.6 a), with the SRH-PJA illustrated uses a stepper motor (NEMA 17; ABB) to drive a crank-slider attached to the piston of a syringe, in which the pneumatic volumes were then displaced into the SRH-RJA or SRH-PJA. The input frequency was altered via the speed of the stepper motor. s revealed in the bode plot (Figure. 4.7 b), the relationship between the volume displacement input and the angular displacement output follows closely a first-order transfer function response. This can be verified by observing that the phase lag reaches 45 degrees at 1.2 Hz. With the cutoff frequency at 1.2 Hz, this implies that the SRH-RJA is capable of stably providing its full range of motion from 0 to 90 degrees and back, at 1.2 Hz. Using the same setup, the dynamic displacement characteristic of the SRH-PJA in frequency domain was studied (Figure. 4.7 c). The displacement bandwidth of the SRH-PJA was determined to be 0.9 Hz.

To ensure the repeatability as well as the durability of the proposed method, the change in response to the SRH-RJA and SRH-PJA displacement output upon accelerated life cycle testing was investigated . Both the SRH-RJA and SRH-PJA were provided with step pressure input of 20 kPa for free expansion, followed by vacuum for retracting back to the starting position. The SRH-RJA was tested for 15,000 cycles and the SRH-PJA was tested for 25,000 cycles. The comparison of the first five and the last five cycles of the SRH-RJA is shown in Figure. 4.6 d). After 15,000 cycles, the differences in peak angular displacement between the first and last cycle were found to be + 0.31 degrees, with a mean difference of + 0.15 degrees at steady state. Therefore, the SRH-RJA expanded additional 0.34 % of its original angular displacement range. Similarly, as shown in Figure. 4.6 e), the SRH-PJA provided a mean difference of + 0.22 mm after 25,000 cycles. This results in the SRH-PJA expanding additional 0.62 % of its original linear displacement range. Overall, the actuators do possess tendency to expand further after numerous cycles, but the magnitudes of additional expansion were insignificant for both the SRH-RJA and SRH-PJA.

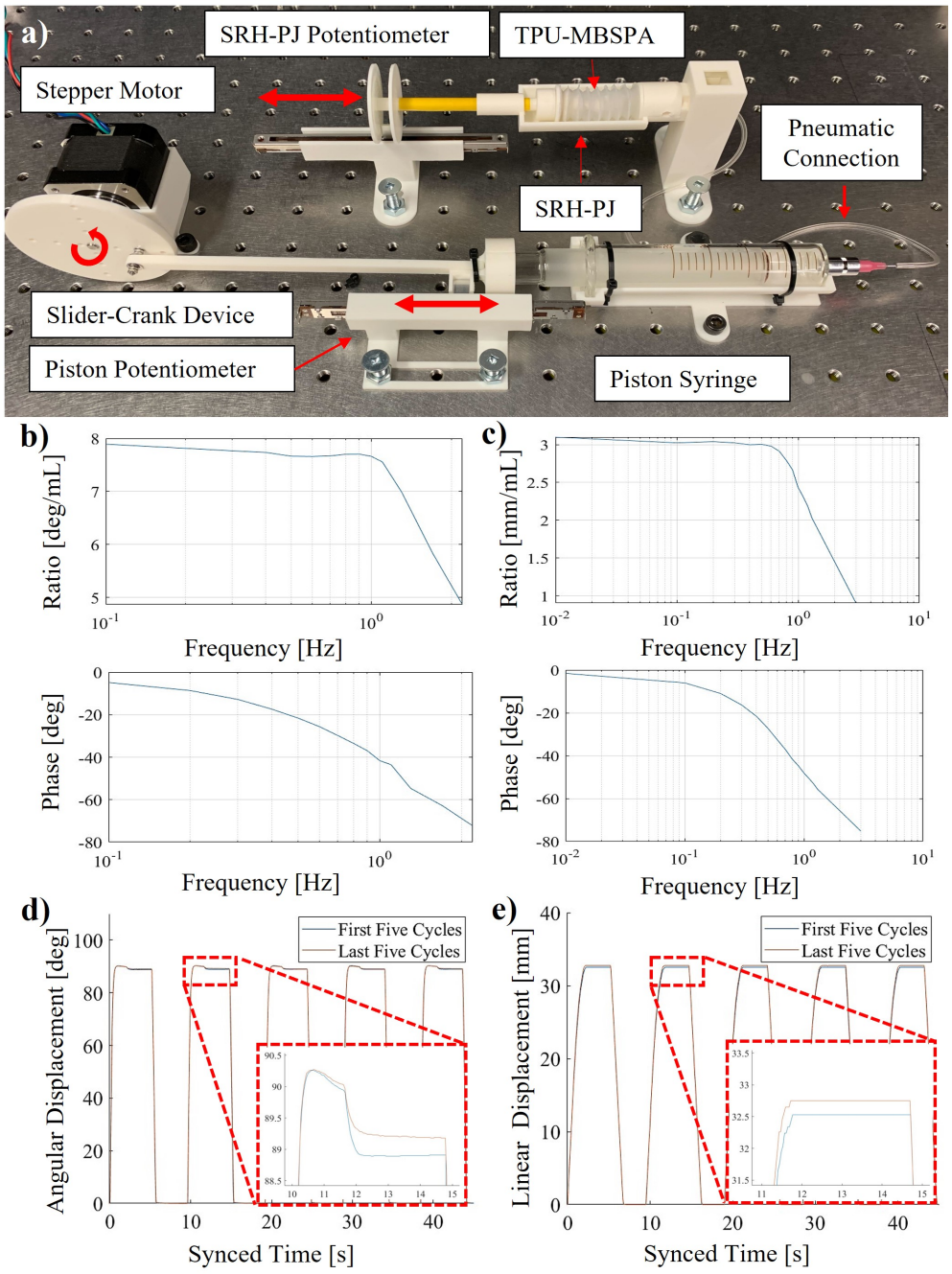


Figure 4.6: a) The dynamic displacement setup used for both SRH-PJA and SRH-RJA. The frequency response and durability results of b&d) SRH-RJA and c&e) SRH-PJA

4.2.5 Blocked Force Output and Variable Stiffness

The force output characteristics of the SRH-RJA and SRH-PJA were investigated via the procedures commonly used in literature [40, 107, 108]. With the stationary component of the SRH-RJA fixed, the TPU-MBSPA was pneumatically injected with 0.1 kPa step increment pressure up to 40 kPa, in which the tip force of the rotary component was measured via the load cell (FS2050; TE Connectivity). To investigate the range of force outputs provided by the SRH-RJA when at different obstructed angular displacements, the load cell was moved from 0 to 90 degrees with a 5-degree increment. A total of 18 tests were repeated three times for each.

As shown in Figure. 4.7 a), the quasi-static blocked force output showed that the tip force output decreased as the obstruction angle increased. This phenomenon is simply because the portion of the provided pneumatic pressure input was used to expand the TPU-MBSPA. As previously shown in the angular displacement output characteristic of the SRH-RJA, the TPU-MBSPA needs to be expanded with a minimum of 13 kPa pressure in order to drive the rotary component to a 90 degrees angular displacement. The additional inefficiency arises due to the radial bulging of TPU-MBSPA when encountered with counteracting forces. With the casing method, the TPU-MBSPA makes contact with the inner wall of the rigid casing which counteracts the radial bulging. This counteracting force applied by the rigid casing was measured with a force resistive sensor (A301, Tekscan). The maximum force between the TPU-MBSPA and the inner wall of the casing to prevent the buckling of TPU-MBSPA was found to be 2.2 N (Figure. 4.7 b).

Overall, the SRH-RJA provided a max tip force output of 4.93 $\pm$ 0.1 N when the angle of obstruction was at 0 degree, 3.37 $\pm$ 0.08 N when obstructed at 30 degrees, 1.95 $\pm$ 0.05 N at 60 degrees, and 1.05 $\pm$ 0.02 N at 90 degrees. This result is significantly superior compared to previous studies which utilized MBSPA without rigid embodiment [40, 41]. This improvement is largely contributed by the proposed method of rigid casing counteracting the tendency of TPU-MBSPA to buckle.

Using the similar setup, the stiffness of the SRH-RJA was investigated by applying known external forces via the force sensor, while regulating the constant internal pressure of the TPU-MBSPA and monitoring the magnitude of the SRH-RJA angular retraction. The stiffness of SRH-RJA configuration is as shown in as shown in Figure. 4.7 c). Though the revolute joint stiffness measurements had high variations at lower pressures, the joint stiffness of the SRH-RJA followed an upward linear trend. This implies that the higher the maintained internal pressure of the TPU-MBSPA is, the higher the stiffness of the SRH-RJA will be. Higher stiffness of the SRH-RJA also corresponds to its magnitude of resilience against external loads.

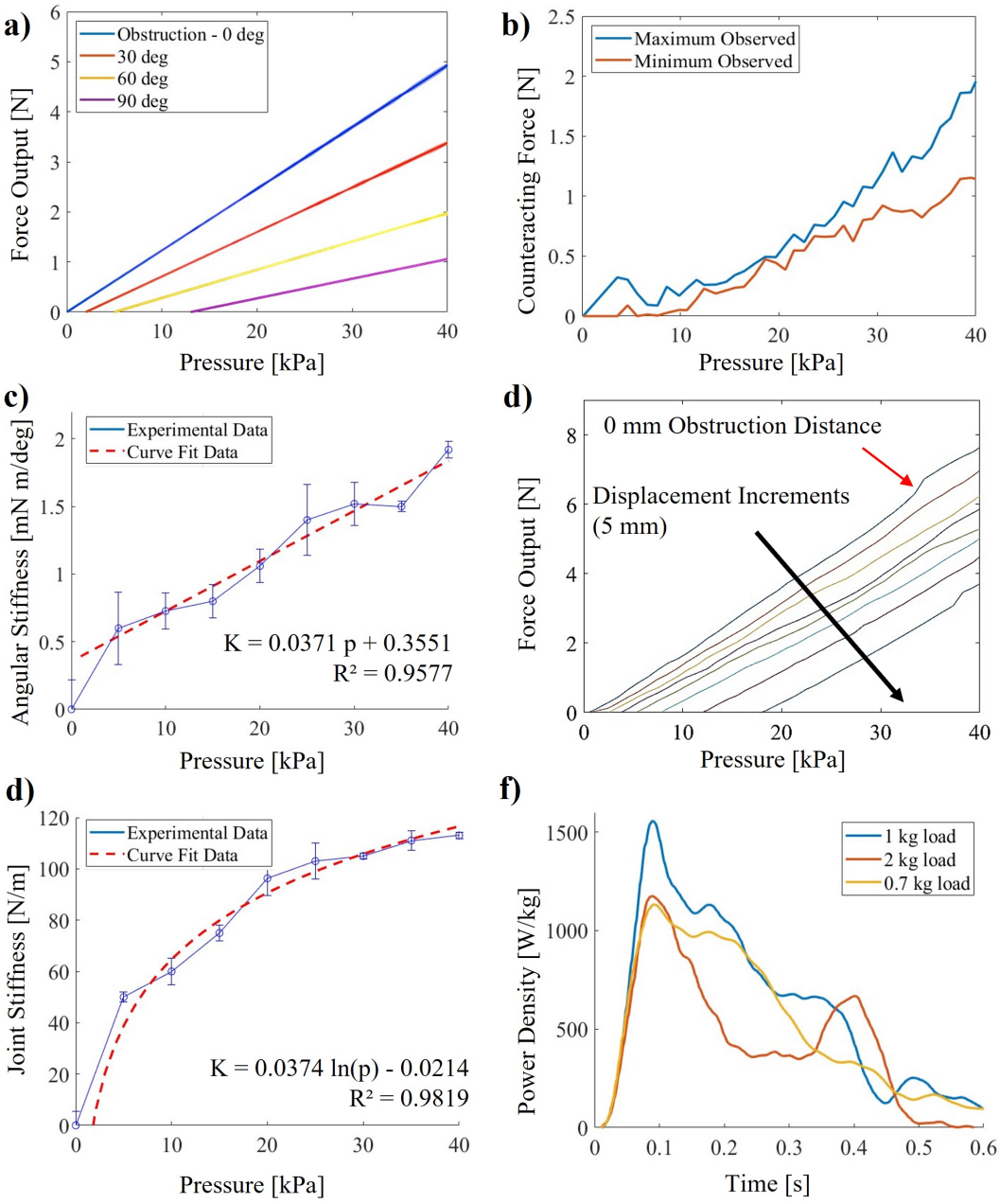


Figure 4.7: The test results of a) SRH-RJA obstructed force output, b) counteracting force against radial bulging, c) angular joint stiffness, d) SRH-PJA obstructed force output, d) linear joint stiffness, and e) power density.

To quantitatively characterize the force output characteristics and joint stiffness of the SRH-PJA, the same load cell was used with the linear displacement setup. As shown in Figure. 4.7 d), the SRH-PJA provided a max force output of 7.61 ± 0.09 N at 40 kPa, with 0 mm obstruction distance. With the same input pressure, the tip forces were 6.15 ± 0.08 N at 10 mm obstruction distance, 5.27 ± 0.06 N at 20 mm, and 4.43 ± 0.04 N at 30 mm, respectively. The reason for the reduced tip force output with increased obstruction distance is analogous to the case of the SRH-RJA. When the obstruction distance had increased, an increased portion of the input pressure was used to expand the TPU-MBSPA in the SRH-PJA. Unlike the linear trend presented for the joint stiffness of the SRH-RJA, the joint stiffness of the SRH-PJA (Figure. 4.7 e) followed a logarithmic trend. Following the standard method of measuring power density as presented in previous works [41, 109, 110], the power density of the TPU-MBSPA was also investigated. The SRH-PJA was configured to push different calibration weights vertically upwards using the TPU-MBSPA which weighs only 0.85 g. To explore the power density output of the TPU-MBSPA, an input pressure of 100 kPa was provided. As shown in Figure. 4.7 f), the peak power density delivered by TPU-MBSPA was experimentally determined to be 1.56 kW/kg, when lifting a 1 kg calibration weight. This is comparable to a wide range of power densities reported for soft pneumatic actuators, ranging from 8 W/kg [109], 2 kW/kg [110], up to 6.31 kW/kg [41].

4.3 Application as SRH Gripper

One prominent direction of soft grippers is in food and agriculture industry applications such as harvesting of berries and other delicate fruits, in which the compliant soft grippers prove the potential for automated harvesting without damaging the products to preserve their commercial viability [111]. In fact, the importance of soft robotics research toward fruit harvesting is growing rapidly. According to the United States Department of Agriculture report, the U.S. berry market reached a value of $ 7.5 billion in 2020 [112]. The global market is expected to grow an additional 9.3 % by 2025, with the compound annual growth rate from 2023 to 2028 is projected to be 3.7 % [49]. With the rising demand for food products confronted by the increasing labor shortage issues, producers are now gearing toward automated harvesting options [113].

4.3.1 3-Point Soft-Rigid Hybrid Gripper Design

As shown in Figure. 4.8 a), a proof of concept 3-point Soft-Rigid Hybrid Gripper (SRHG) was developed using three SRH-RJAs placed 120 degrees apart from one another such that they do not collide into each other throughout the entirety of motion. As a sample application, it is designed to grip objects as large as 70 mm and as small as 6 mm in diameter from the fully retracted position to the fully actuated position. For the purpose of demonstrating uniform 3-point gripping and its functionality, the proposed SRHG was integrated as an end-effector of a collaborative robot (myPalletizer 260; Elephant Robotics). In this proof of concept, the co-bot was controlled via the customized forward kinematics joint angle publisher in Robot Operating System (ROS). The main angle position controller was subscribed to the joint state publisher, in which the desired angular position of each joints were controlled via the slider user interface.

The three SRH-RJAs are pneumatically interconnected to share the same pneumatic source, which also allows the internal pressures of all three SRH-RJAs to be uniform. Since all three fingers are identical to the SRH-RJA investigated in the previous sections, the majority of characteristics such as frequency response, durability, and displacement characteristics were equivalent to a singular SRH-RJA.

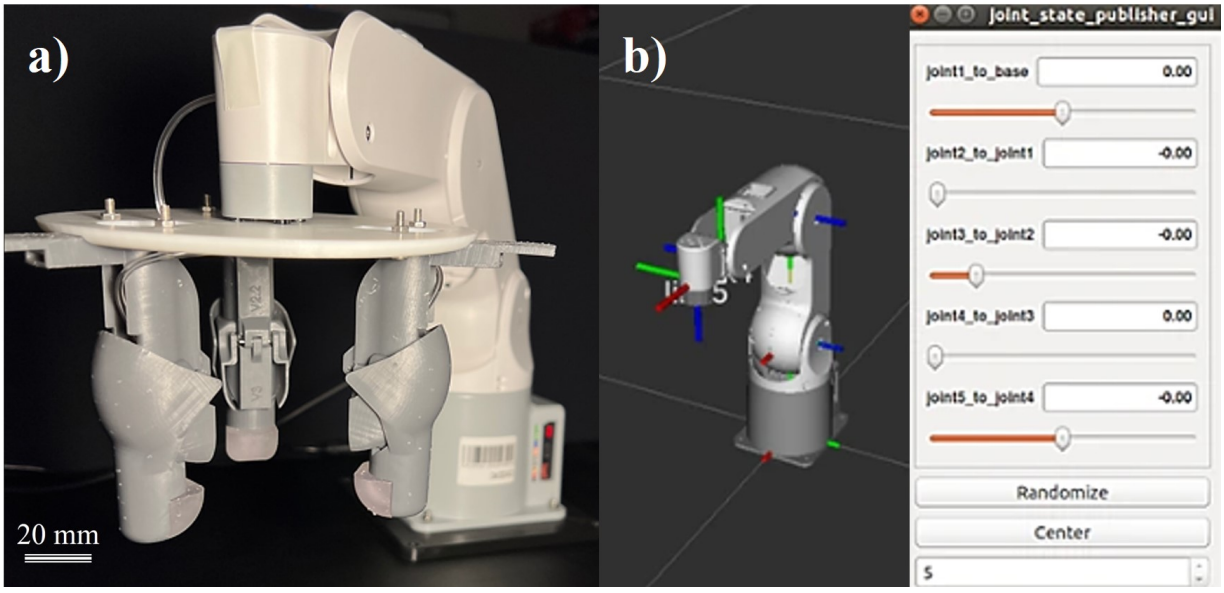


Figure 4.8: a) The proof-of-concept 3-point SRH gripper. b) The co-bot in its simulation settings with the custom joint state publisher in ROS.

To capture the angular displacement and internal pressure information of each SRH-RJA, a capacitive bend sensor and a pressure sensor (MPRLS Ported Pressure Sensor Breakout - 0 to 25 PSI, Adafruit Industries) were utilized for each SRH-RJA. These sensors were connected to the low-level controller through the I2C communication protocol. However, a challenge arose as the device address for each of the three pressure sensors and each of the three capacitive bend sensors were identical. To ensure proper segregation and labeling of sensor data, an I2C multiplexer (TCA9548A I2C Multiplexer, Adafruit Industries) was employed. The sensor data was then collected and preprocessed by a low-level microcontroller. This processed data was then fetched by a high-level microcontroller, which directly communicated with a centralized computer. The high-level microcontroller communicated with the centralized computer directly, and processed data were automatically logged into MATLAB after each operation for further post-processing. For the 3-point SRHG, only one low-level controller was required. However, this cascaded control system was designed to be easily scalable, allowing for an increase in the number of SRH-RJAs or the number of required sensors in the future.

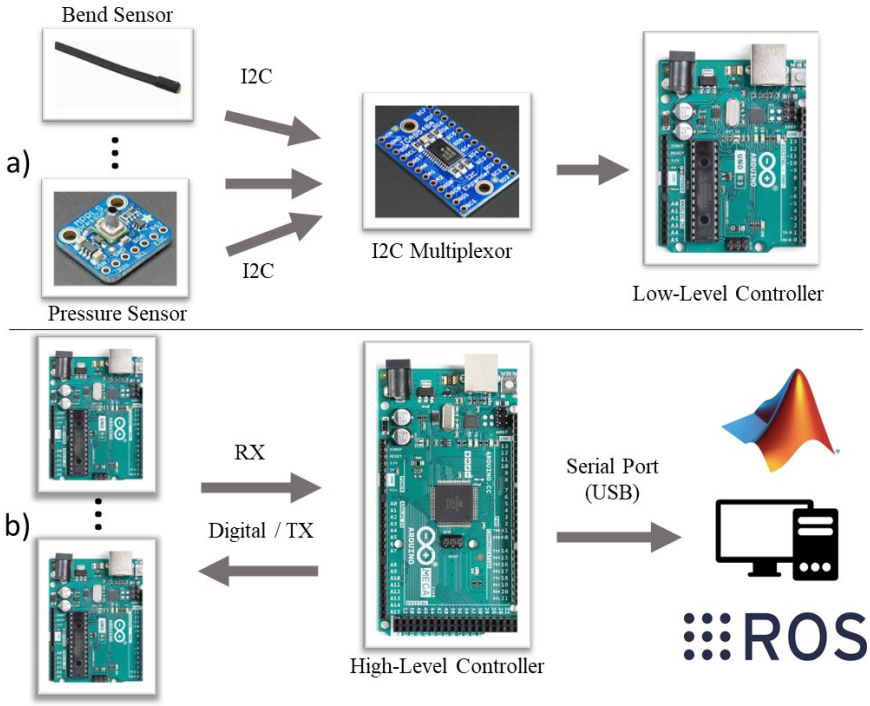


Figure 4.9: The schematic of the cascaded control setup. a) Entails the low-level controller and b) high-level controller configuration

4.3.2 Gripper Workspace and Demonstration

To explore a wide range of objects that the 3-point SRHG can manipulate, the gripper workspace was first derived using the geometric configuration of the SRHG. Using objects of different shapes and sizes, this gripper workspace was verified experimentally via open loop gripping with pressure input. The comparison result of the experimentally determined contact space for stable gripping and the expected contact trajectory for stable gripping are as shown in Figure. 4.10 a). The SRHG was capable of stably gripping objects of any sizes and irregular shapes, as long as the outer contour of the object were within the experimentally derived gripper contact space and have made contact with minimal of 2 fingers. Notable unique case was when the gripper was able to make stable grip via lateral pinching of only two fingers. This was made possible due to the rigid hinge providing lateral counteractive force against the object. A similar observation was reported in preliminary soft-rigid hybrid grippers focusing on lateral compliance [97]. In cases of gripping irregularly shaped objects, certain fingers contacted the object earlier than the others. When this had occurred, the finger that made contact earlier complied to the shape of the object and did not apply additional forces until the other fingers made full contacts with the object.

The stiffness of the SRHG gripper determines the ability of the gripper to provide stable gripping and lifting of the objects. To investigate the compliance of the SRHG, a tapered cylinder was used. Starting from the three fingers of the SRHG contacting the smaller diameter of the tapered cylinder, forces were applied to the fingers when the tapered cylinder was moved to the larger diameter section. As shown in Figure. 4.10 b), the result showed that the range of variable stiffness of SRHG gripper was 26.5.N/m to 76.2 N/m. This implies that the capability of the SRHG to vary its stiffness depends on the delicacy of the object. This is comparable with other soft grippers providing variable stiffness [114, 115]. As summarized in Figure. 4.10 c), the SRH gripper was able to securely grip a wide variety of objects as small as 7 mm in diameter, as light as 2.2 g, as large as 68 mm in diameter, and up to 1 kg calibration weight. The objects and their respective weights, sizes, as well as the pressure and joint stiffness required to perform holding grip stably are as summarized in Table. 4.1. While gripper stiffness investigation focused on the lower operating pressure range, the maximum payload stable holding grip was 1 kg calibration weight. This was enabled by applying a 77 kPa internal pneumatic pressure. Even though detailed evaluation has not yet been done with higher operating pressure ranges, this provided an insight that the proposed SRHG has great potential to be extended for use in general robotics requiring higher stiffness and payloads.

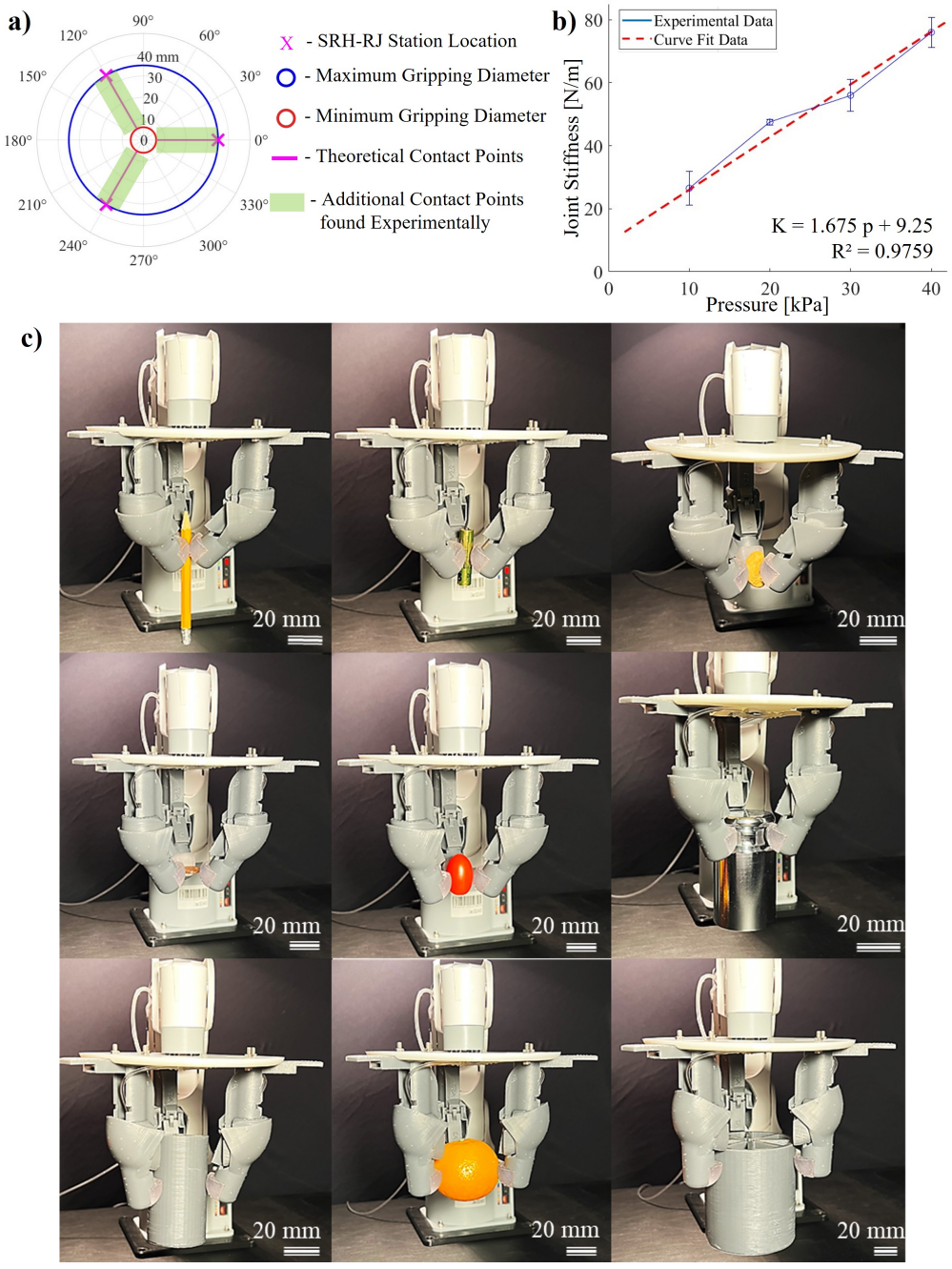


Figure 4.10: a) The soft-grip workspace for stable gripping. b) Joint stiffness results of the SRH gripper. c) Collage of wide variety of objects tested for validation.

Table 4.1: List of objects gripped with soft-rigid hybrid gripper and their respective gripping diameter and weight.

Object	Gripping Diameter (mm)	Weight (g)	Additional Pressure Required for Stable Gripping (kPa)	Estimated Gripper Stiffness (N/m)
Pencil	7	2.9	1.12	11.13
AAA Battery	10.3	11.65	3.20	14.61
Cashew	12	2.2	1.21	11.28
1 EU Cent	16.25	2.3	0.51	10.10
Grape Tomato	22	8.3	8.76	23.92
1-kg Weight	30.7	1000	75.01	134.89
Cylinder 1	45	97	7.55	21.90
Mandarin	56	80.5	6.73	20.52
Cylinder 2	68	157.7	9.13	24.54

4.3.3 Conclusion

This study proposed SRH-based joints enabled via the TPU-MBSPA - the Revolute Joint Actuator (SRH-RJA) and the Prismatic Joint Actuator (SRH-PJA). Through rigorous experimental testing, the robustness and repeatability of these joints under different conditions were confirmed. The performance of the SRH-RJA and SRH-PJA in terms of displacement, frequency response, durability, force output, stiffness, and power density has been thoroughly studied and validated. In addition, the application potential of these joints was demonstrated with the development of a three-point gripper, which can effectively handle objects of various sizes and shapes. This study laid an essential groundwork for future research and optimization in the field of soft robotics. The promising outcomes of this research suggest that with further improvements, the SRH system with MBSPAs could potentially revolutionize delicate object manipulation in numerous industries, particularly in food and agriculture.

Future work may include further optimizing the system and fine-tuning the gripper for specific berry harvesting such as blueberry, raspberry, and strawberry which present different needs. Field testing may also commence to validate the protective shell's efficacy at in protecting the internal soft components. Sensor technologies can also be integrated to provide real-time feedback and enable more precise control over manipulation tasks.

Chapter 5

Naturally Compliant Dexterous Anthropomorphic Hand via Modular Soft-Rigid Hybrid Robotics

This chapter entails the detailed investigation of the Modular Soft Rigid Hybrid Modular Soft-Rigid Hybrid (MSRH) robotics approach toward designing of a naturally compliant dexterous anthropomorphic hand. The following sections first provide a review of critical design philosophies in robotic hand design, existing methodologies, and limitations of each methods are provided. Upon applying new design and fabrication technique for the previously developed TPU-MBSPA, the design rationale and the anthropometrics of the robotic hand are shared. To account for the spatial constraints intrinsic to robotic hands, customized electrons are designed, fabricated, and shared. The proposed hand is then evaluated using the standard assessments including weight, force output, taxonomies, and gripping and grasping tests.

5.1 Background and Robotic Hand Philosophy

The front end of every social robot and robotic manipulators are the robotic end-effectors employed for the physical interaction with various objects, environments, and people. While the shapes, sizes, and types of the robotic end-effectors vary depending on the specific functions required in different applications, artificial hands have drawn a great deal of attention and research effort in applications requiring physical Human-Robot Interaction (pHRI). With the goal of replicating human-like motion and dexterity, novel designs

of anthropomorphic hand robots have been investigated over the years for use in social robots, hand prostheses, teleoperated surgical robots, handling of delicate objects, and most importantly, toward improved physical Human-Robot Interaction in general [116].

For the successful integration of artificial hands in daily pHRI applications, it is crucial to consider the social human-robot interaction (sHRI) focused principles such as social acceptance [117]. Social acceptance of robotic systems is governed by multiple factors including safety, affordability, and people's psychological acceptance toward the robot in general. Considering that familiarity is a crucial factor in how people perceive of robots [118], anthropomorphic designs involving human-like appearance and motions must not be overlooked [119]. Highly anthropomorphic artificial hands have a high number of actively controlled degrees of freedom (DOF) to closely mimic the highly intricate and complex nature of the human hand [120, 121]. These fully-actuated, if not nearly fully-actuated robotic hands are capable of achieving excellent dexterity and human-like kinematics [122, 123]. However, they typically require a high number of motorized devices and hence face practical issues such as spatial constraint, poor portability, and increased cost. To remedy this issue, underactuated robotic hands with smart linkage systems can be designed to reduce the number of actuation devices while maintaining limited anthropomorphic dexterity [124, 125]. However, underactuated robotic hands rely on fixed trajectories and often require complex linkage systems [126, 127]. This trade-off between attaining a highly anthropomorphic dexterity versus practical challenges in implementation is a dilemma often observed in motor-driven robotic hand systems, leading the researchers to develop function-specific hands [128].

Another critical aspect to consider when designing robotic systems for HRI is user safety [119]. User safety is intuitively the most important user-centered design philosophy and a crucial factor that significantly affects social acceptance of robotic systems, especially in HRI applications [117, 129]. To address user safety and to overcome the limitations exhibited in motor-driven rigid robotic hand systems, recent works in artificial hands utilized soft robotics approach [130]. Specifically, pneumatically actuated soft actuators can be employed to create soft robotic hands. Due to the compliant nature of soft materials and the compressibility of air, soft robotic hands are compliant, can conform to irregular shapes and unstructured environments without complex control schemes, and have low manufacturing costs [99]. In addition, the pneumatic source for the soft actuators can be placed further away from the joint locations, allowing the system to run on a simplified configuration without the need for a complex linkage system [130].

However, robotic hands comprised purely of soft components have limited dexterity because they rely on a fixed trajectory which is predefined during the design process of the soft actuators. Purely-soft robotic hands also possess oscillatory behaviour and are

insubstantial, often requiring skeletons made of rigid materials or needing to be body worn [131, 132]. As an innovative approach to these challenges, a SRH system can be formulated by implementing both soft and rigid robotic components in robotics design [7]. With the synergistic integration of soft and rigid components, SRH robot designs have proven to achieve improved structural rigidity while maintaining the inherent compliance of soft robotic systems [133, 134]. Following the same approach, recent works presented compliant grippers using finger-like structures [97, 135].

5.1.1 Project Objectives and Motives

In this project, the goal is to provide a novel design method of a general-purpose modular soft-rigid hybrid (MSRH) robotic hand, which is designed to be highly anthropomorphic, provide human-like motions, and be naturally compliant, hence suitable for safe pHRI applications. The construction of the hand leverages the soft-rigid hybrid approach developed in previous sections, hence comprised of soft actuators driving the angular displacements at the joint locations, and the rigid links for providing a robust skeleton structure.

While previous works adopted a similar soft-rigid hybrid structure [99], this method has not yet been extended to provide a fully actuated system. In addition, the proposed MSRH configuration allows the number of actively controlled DOF to be easily modified while maintaining robust kinematic trajectories, which is enabled by the combination of soft and rigid robotics approaches. This is unlike the underactuated purely-soft robots or traditional motorized rigid robotic systems, in which the number of controlled DOF is fixed during the design stage of the robotic hand. Also, this approach is aimed to reduce fabrication cost and time by leveraging the capability of soft robotic components to be manufactured at low cost and short lead time. Therefore, the proposed MSRH method would be of an innovative approach to designing a highly compliant and anthropomorphous robotic hand that is not limited by the local spatial constraints commonly challenged in dexterous robotic hand design methods in both soft robotics and rigid robotics [136].

5.2 MSRH Hand Design and Methods

5.2.1 TPU-MBSPA Fabrication via Folding Technique

Similar to the soft-rigid hybrid revolute joint actuator presented in chapter. 4, the core element that enables the presented MSRH configuration is the TPU-MBSPA. Unlike the

monolithic type SPAs, TPU-MBSPAs possess a good form factor, minimal thickness when retracted, and a superior retraction-expansion ratio. Depending on the shapes and sizes of the thermal adhesive films and/or thermal prevention layers used for the thermal bonding process, TPU-MBSPAs can be made to deliver desired amounts of displacements and provide any combination of linear or angular movements. These traits make TPU-MBSPAs favorable to be utilized in a hybrid configuration.

As previously demonstrated in Chapter. 3.1, the fabrication of TPU-MBSPA follows a layered manufacturing approach which requires the preparation of thermally adhesive materials and thermally resistive materials, stacking of these materials in specific orders and alignments, and lamination via heat press. While the fabrication method is straightforward and generally scalable in size, the process of individually aligning the materials is tedious and very time-consuming, especially when fabricating smaller scale TPU-MBSPAs. In addition, the TPU-MBSPAs have a tendency to bulge outward radially if improperly constrained, which is often observed in applications utilizing MBSPAs to provide angular displacements and torques. Radial bulging must be eliminated, if not mitigated, because it significantly reduces the torque delivered by the MBSPAs, making the entire system mechanically inefficient. While rigid casing methods to provide counteracting forces against the radial bulging have been investigated in Section. 4.2.1, this method inapplicable in applications involving extensive spatial constraints such as a robotic hand. To address an alternative approach to tackle the unconstrained radial bulging, the fabrication of the TPU-MBSPA in the presented MSRH hand employed a folding technique and a bulging constraint feature.

The fabrication details of the TPU-MBSPA are as shown in Figure. 5.1. As with the earlier fabrication method of TPU-MBSPA, the first step involves computer-controlled cutting of the three components; TPU layers, insert layer, and the separation layer (or the thermal-bonding stencil layer). The new folding method allows easier concentric alignment of layer components. Upon preparation of each actuation layers, all actuation layers are stacked and heat-pressed at 110 °C to create a multilayered structure. Upon the second folding procedure, removal of thermal bonding stencil papers, and insertion of pneumatic tubing, the fabrication of TPU-MBSPA is completed. The resultant MBSPAs used in the finger joints are designed to withstand 1 bar gauge pressure, have an initial retracted thickness of 8 mm, and can expand to provide 90° angular displacements to travel an arc length of 23.55 mm, resulting the retraction-expansion ratio of 294 %.

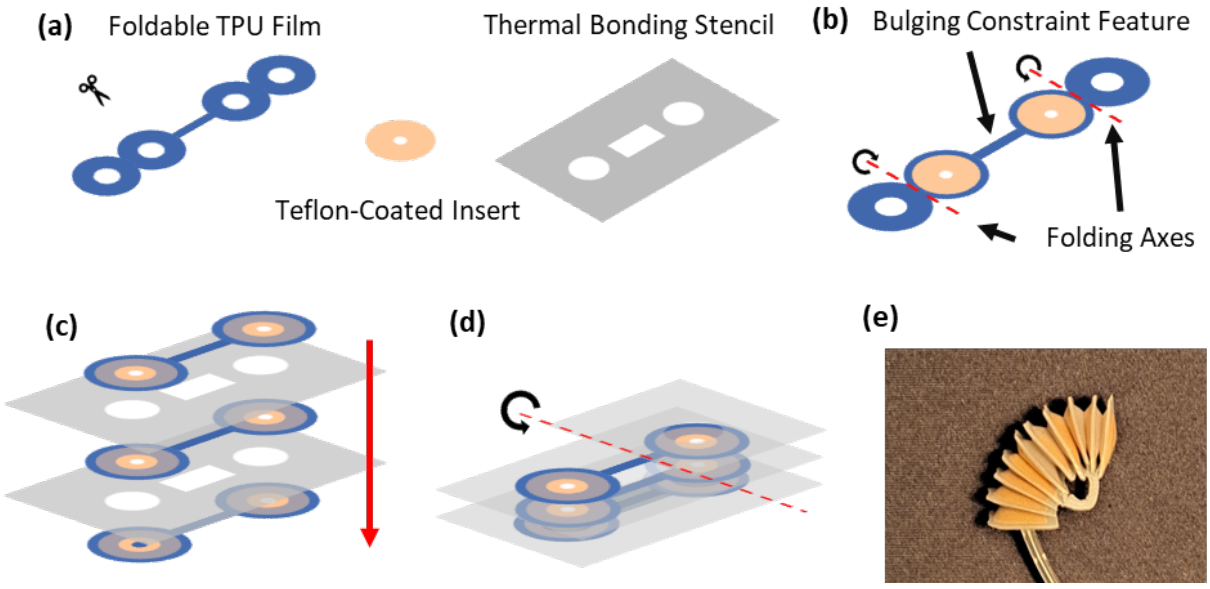


Figure 5.1: Fabrication details of the MBSPA joints. a) Preparation of layer components. b) Key features of the individual actuation layer. c) Heat-press to form multilayered structure. d) Second folding procedure. e) Resultant TPU-MBSPA.

5.2.2 Modular Soft-Rigid Hybrid Design Features

The MSRH hand is designed with the intention to achieve low manufacturing cost, high durability, and a soft compliant interface. For ease of assembly and disassembly, the mechanical construction of the hand is divided into three key modules: a two-piece phalanx module, a soft actuator module, and a soft human-like skin module, as shown in Figure. 5.2.

Each phalanx of all the hand phalanges is made up of the two-piece phalanx module. The two-piece phalanx modules are the rigid linkages of the MSRH system, providing the overall skeletal structure for the hand. The two-piece phalanx modules are 3D printed with PLA filament for its low cost, lightweight, and rapid prototyping capabilities. To account for the fact that human hands perform a large cycle of grasping during daily tasks [137], a rigid pin joint is adopted in each front half of the two-piece phalanx module. The two-piece phalanx module is also designed with press-fit features and internal grooves to encapsulate the soft actuator module during the assembly process. This snap-together design provides a tight and secured positioning of the soft actuator module, which can only be disassembled via pry opening the disassembly slot located on the side of the phalanx module. This

modular approach allows any part of the hand to be easily swappable, should the part require any modification or replacement. This is beneficial over having to re-fabricate the entire hand at every development stage.

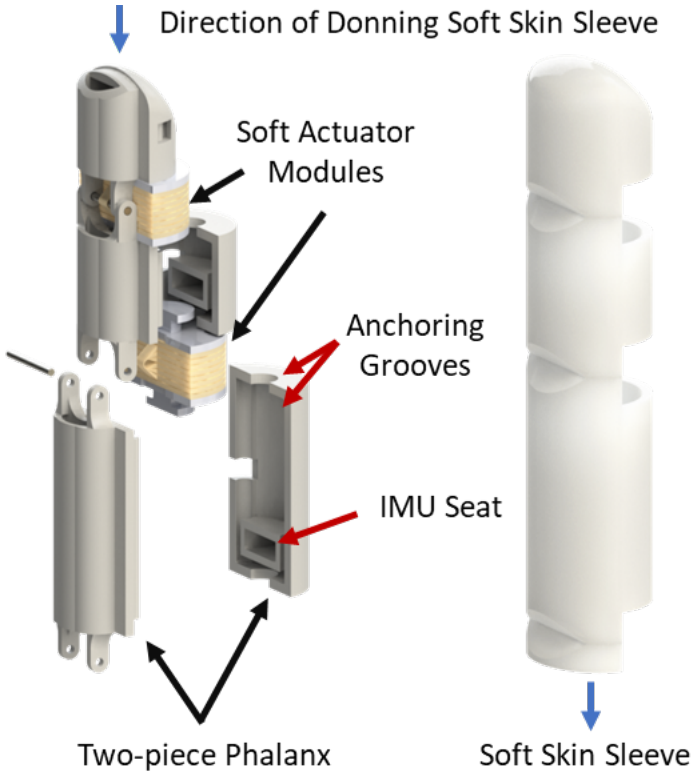


Figure 5.2: The three modules comprising the mechanical construction of the MSRH hand. The two-piece phalanx modules have integrated pin joints and grooves to encapsulate and secure the position of the soft actuator modules and the IMU sensor. The soft skin is designed to slip onto the assembled modules. To assemble, i) Soft-actuator module is fitted into the grooves of the two-piece phalanx modules, ii) The pin is inserted for concentric alignment of pin joints and the actuator bulging constraint feature, iii) Soft skin sleeve is donned over the sub-assembly.

The soft actuator module is comprised of two rigid plates attached to the top and the bottom of the MBSPA, in which the rigid plates are securely anchored by the two-piece phalanx modules during the assembly. Once the soft actuator module is assembled with the two-piece phalanx module, the pin is inserted through the pin joint mounts of the two-piece phalanx module as well as through the bulging limitation feature of the soft

actuator module. With the bulging limitation feature of the MBSPA wrapped around the pin, the soft actuator is anchored and prevented from bulging out radially. In addition, the pin joint enforces all rotation of the soft actuators to occur at a fixed axis of rotation. Therefore, the kinematic structure of the SRH hand can be constructed using the kinematic representations and coordinate transformations of rigid robotic systems. The soft humanlike skins are designed to enable a soft and compliant interface of the robot. With the molds for the individual fingers and the palm being 3D printed using PLA material, silicon rubber (Ecoflex 0030, SmoothOn Inc) is cast to closely mimic the outer skin layer of a human hand [138]. At each joint location, the thin-wall soft skins are designed with a taper to ensure that the bending of joints is not impeded by the soft skin.

5.2.3 Anthropometrics-Based Design

To achieve a highly anthropomorphous structure, the key geometric relations of the MSRH hand components are designed based on the proportions derived from the average human hand dimensions. This proportion-based approach is chosen because the reported human hand dimensions vary largely depending on the sampled demographics, but the proportions of hand parts are generally the same. For example, the length of the hand is generally reported to be about 1.75 times longer than the length of the palm, and 2.14 times longer than the width of the palm [139, 140]. The same idea is applied when designing the lengths of different finger segments. While the reported lengths of finger segments differ in terms of their magnitudes, the relative ratios of the segments remained similar in different reports [141, 142].

All the key dimensions of the hand and finger segments are normalized in terms of the length of the index proximal phalanx. The anatomy of the anthropomorphic SRH hand is as shown in Figure. 5.3, and the resultant dimension proportions are as summarized in Table. 5.1. Keeping the design dimensions in terms of normalized proportions allows the MSRH hand to be scaled to different sizes while maintaining the anthropometrics. For demonstrating this scalability of anthropomorphic design, the hand components are scaled to be 25 % larger than the average hand. In addition, the cross-sectional dimensions of all finger segments are chosen to be uniform in this proof of concept, represented as an oval shape with the width and thickness of the typical index proximal phalanx [143].

The metacarpophalangeal (MCP) joints of the human hand provide two DOF which enable the flexion/extension of the proximal phalanx as well as the abduction and adduction motion. To mimic such a spherical joint, the structures of the finger metacarpal phalanges are each modified to host two MBSPA in series, such that the first MBSPA provides

abduction and adduction motion, followed by the other MBSPA providing flexion and extension motion. This is necessary because the MBSPA is a modular joint that can only provide one DOF per actuator. In addition, the complicated structures of the carpal bones and human palm are simplified and modified to provide the thumb opposition motion and the small range of motion of the pinky metacarpal phalanx. The additional joint at the root of the pinky and ring metacarpal phalanges provides improved dexterity in ulnar grasping and ulnar manipulation [99].

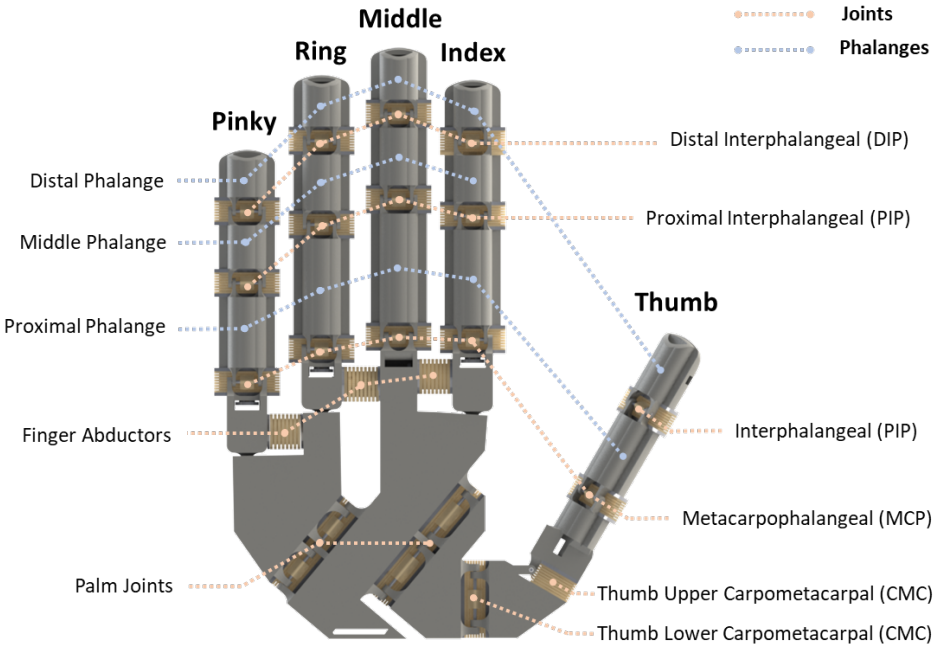


Figure 5.3: The anatomy of the MSRH hand.

The thumb of a human hand is capable of performing complex maneuvers such as flexion / extension, abduction / adduction, and reposition / anteposition [144]. Considering the importance of these movements in various gripping and grasping motions humans perform daily, the dexterity and the ability of the robotic hand to replicate human hand gestures depend greatly on the quality of the thumb design. To enable the robotic hand to mimic the complicated structure of the human thumb using single-DOF MBSPA joints, the thumb is comprised of 5 MBSPA joints mounted in a series configuration. The interphalangeal (IP) joint and MCP joints are enabled with one MBSPA joint each, for flexion/extension motion. Just underneath the MCP joint is the MBSPA joint oriented as a thumb adductor,

enabling the abduction and adduction motion. As for the opposition and reposition motion, two MBSPA joints are placed in series at different orientations to attain the wide range of motion of the thumb reposition / anteposition and abduction / adduction motions.

Table 5.1: Summary of key hand segment dimensions and their normalized ratio with respect to index proximal phalanx.

	Ratios of Finger Segment Dimensions		
Finger	**Distal (mm)**	**Middle (mm)**	**Proximal (mm)**
Thumb	0.71 (37.27)	-	0.81 (42.77)
Index	0.53 (28.04)	0.60 (31.77)	**1 (52.59)**
Middle	0.57 (30.14)	0.69 (36.50)	1.11 (58.39)
Ring	0.57 (29.88)	0.68 (35.69)	1.01 (52.91)
Pinky	0.54 (28.14)	0.58 (30.50)	0.80 (42.09)
Hand Length	4.78 (251.60)		
Palm Width	2.03 (107.00)		
Palm Length	1.81 (139.20)		

5.2.4 Joint Angle Data Acquisition

In applications requiring the robotic hand to precisely track reference hand gestures, such as replicating human motion or teleoperation applications, precise tracking of angular position is necessary. To monitor the angular position information of each phalanx, a total of 22 custom-designed PCBs are designed in this study, each incorporating a 6-DOF Inertial Measurement Unit (IMU) (MPU-6050, InvenSense). Utilizing the double-sided PCB assembly method, these IMU PCBs are designed to be encapsulated in every two-piece phalanx module of the hand. To do so, the surface area of the IMU PCBs are reduced to 10.45mm by 11.6 mm, an area reduction of 60 % as compared to the off-the-shelf counterpart. The miniature 4mm-thickness IMU PCB is as shown in Figure. 5.4.

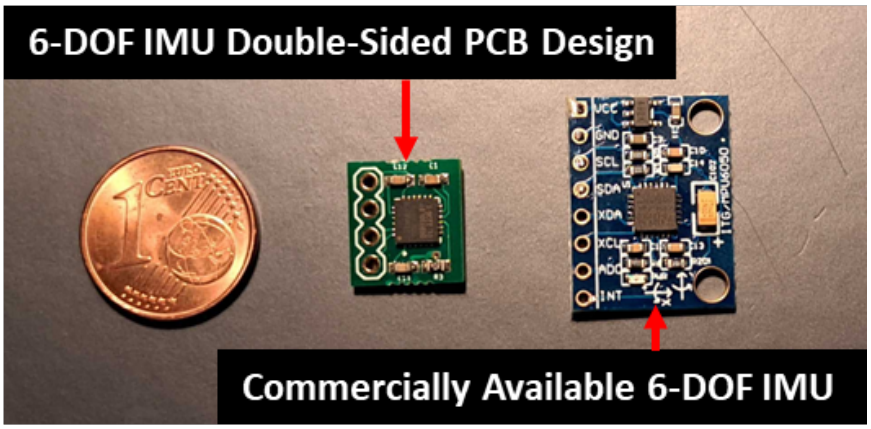


Figure 5.4: Custom designed double-sided 6-DOF IMU PCB compared with the commercially available version. A 1 cent Euro coin is used in this figure for size reference purposes.

5.3 Evaluation of the MSRH Hand Prototype

5.3.1 General Mechancial Specifications

The proof of concept of the naturally compliant dexterous anthropomorphic hand using modular soft-rigid hybrid approach is as shown in Figure. 5.5. The total weight of the MSRH hand is 448 g, of which the 120 g is the weight contributed by the soft skin module. Since force sensors are not yet implemented for this prototype, two force-sensitive resistor sensor arrays (Model 9811, Tekscan Inc) were used to record the contact forces created during the grasping motion. For the maximum operating pressure of the current MBSPA design of 0.8 bar gauge, the maximum grasping force generated by the MSRH hand prototype was measured to be 48 N. This is comparable to other similar types of robotic hands [99, 145]. With the same input pressure, the MSRH hand was capable of lifting stably a maximum payload of 1 kg. In applications requiring the MSRH to provide higher force and lift higher payloads, the MBSPA joints can be provided with higher input pressures. The total material cost of the mechanical components was less than $100 CAD, and the entire hand can be produced from scratch in three days with a two-person labour force.

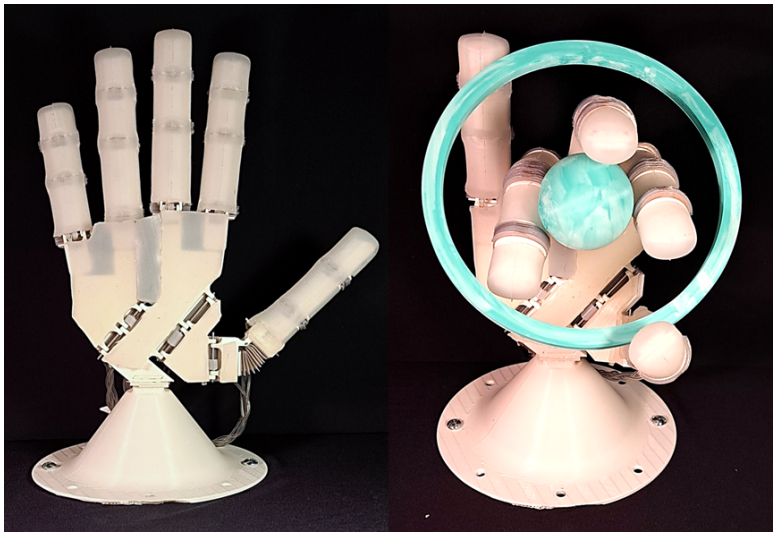


Figure 5.5: Proof of concept of the MSRH hand (left) at the resting state and (right) demonstrating its dexterity.

The MSRH hand design has a total of 21 DOF. Aside from the mechanical components being modular and Lego-like, it is also modular in terms of the number of actively controlled DOF it can have. Specifically, the utilization of MBSPA enables the coupling of any joints in any combinations depending on the desired motions and applications. This is possible because the MBSPA joints operate by pneumatic pressurization, in which the coupling of joints is done via the establishment of a pneumatic connection of the joints (i.e. via tubing) to the common pneumatic pressurization source. For example, the SRH hand can provide the same kinematic trajectories as the underactuated tendon cable motor-driven robotic hands, simply by connecting the distal interphalangeal (DIP), proximal interphalangeal (PIP), and MCP joints to the common pressurization source. By doing so, the three joints are coupled, and the finger will follow a fixed trajectory upon actuated by the common pressure source. This is highly unlike the motorized systems in which the coupling of joints is fixed during the design process of the mechanical structure or the linkage system. In addition, because the pressure sources of the MBSPA can be placed at any location away from the joint location, the configuration is not hindered by local spatial constraints. With the usage of mini-directional solenoid valves and microfluidic technologies, the pneumatic control system can be further miniaturized to achieve a highly dexterous anthropomorphic hand that is not hindered by spatial constraints. This provides a new angle to tackle spatial constraint that normally arises in robotic hand design with increased anthropomorphism.

5.3.2 Thumb Dexterity Evaluation

To assess the dexterity of the thumb design with respect to the human thumb, the MSRH hand was evaluated using the Kapandji taxonomy score [146]. The Kapandji score is a useful assessment tool for the evaluation of thumb dexterity, especially in demonstrating the opposition and reposition motion. The objective of the Kapandji taxonomy is to attain different locations of the hand using mainly the motions of the thumb. A score of 0/10 means that the thumb design has very poor opposition abilities, and a score of 10/10 represents an acquisition of maximum thumb opposition capability. To evaluate the MSRH hand using the Kapandji taxonomy, the desired joint positions were predetermined and executed by manual manipulation of each MBSPA joint individually. As demonstrated in the results shown in Figure. 5.6, the MSRH hand is capable of attaining all locations described in the Kapandji taxonomy, 10/10.

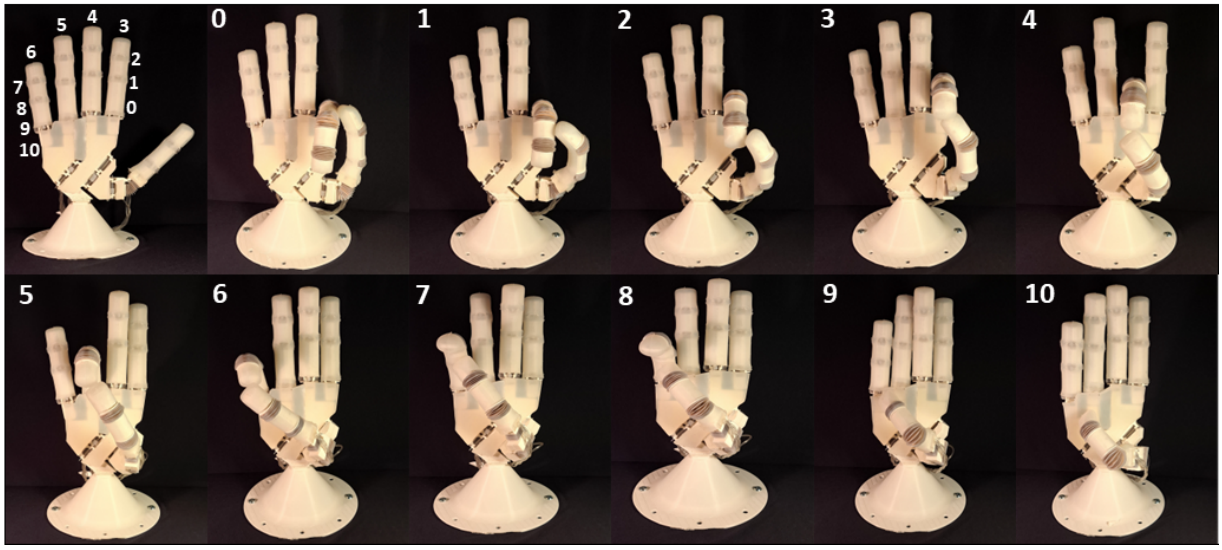


Figure 5.6: Demonstration of thumb dexterity, the MSRH hand is capable of attaining all locations specified in Kapandji Taxonomy Score.

5.3.3 Demonstration of Gripping and Grasping Capabilities

To assess the dexterity of the MSRH hand with respect to the maneuvers that human hands are capable of, the MSRH hand was evaluated using the GRASP taxonomy [147]. The gripping and grasping motions described in the GRASP taxonomy cover most of the grasp types achievable with human hands. With a total of 33 which can be reduced to 17 different modes, the GRASP taxonomy classifies the 33 grasp types into power versus precision grasp types, as well as based on the specific function of the hand components such as thumb abduction versus adduction.

As shown in Figure. 5.7, the MSRH hand was capable of performing all grasping and gripping types specified in GRASP taxonomy. To evaluate the MSRH hand using the GRASP taxonomy, the desired joint positions were predetermined in specific sequences. Due to the compliant nature of MBSPA joints, the MSRH hand conformed to the shape of the objects and provided firm grasps upon open loop grasping. So long as the internal pressures of the MBSPA joints were maintained constant, the hand was able to hold onto the objects stably.

5.3.4 Conclusion

In this project, a highly anthropomorphous and dexterous robotic hand was designed using the proposed modular soft-rigid hybrid (MSRH) approach. This MSRH approach allows the robotic hand to possess an inherently soft and compliant interface suitable for pHRI while maintaining the structural rigidity of the robot with the usage of rigid skeletons. The details of the design rationale, fabrication and assembly methods, and evaluation of the first prototype were investigated and shared. Even though the presented prototype was scaled to be 125 % of the average human hand, the mechanical components only weigh less than 450 g.

The modular design approach allows the MSRH hand to have low manufacturing costs and a short lead time. Creation of the presented prototype costs less than $100 CAD and can be built in three days from scratch with two-person labour. The usage of pneumatic soft robotic actuators also provides flexibility over choosing the number of controlled DOF and joint coupling. This hence provides a new angle to tackle spatial constraint that normally arises in robotic hand design with increased anthropomorphism. Lastly, the dexterity of the proposed hand is demonstrated by evaluating the hand using taxonomies highly relevant to replicating tasks humans perform daily.



Figure 5.7: Demonstration of the MSRH hand performing the grasping and gripping tasks specified in GRASP Taxonomy.

Chapter 6

Preliminary Pneumatic Control Strategies

The potential of the novel soft-rigid hybrid and modular SRH robotics approach has been demonstrated in the previous sections. However, demonstrations were all done in a lab environment, focusing on the basic essential mechanical performance characterizations as per the standard methods commonly adopted in the literature. Typical robotic end-effectors operate based on a centralized computer providing position trajectory input, in which the execution is done automatically via feedback control system. To bring these systems to the next level and achieve an automated system, it is critical to investigate control methods. This is not an easy task, because this involves an investigation of the dynamics of the SRH robot. Despite the challenges and the time limit of my master's program, a preliminary pneumatic control strategy is studied briefly in this chapter. The goal of this chapter is to provide a precedent, pioneering and paving the development of the SRH robots toward fully automated system using adaptive control.

This chapter entails the preliminary investigation of pneumatic control strategies specifically targeted for controlling the SRH robot. For simplicity, this investigation is limited to a 1-DOF SRH-RJA. The following sections first provide an overall system structure and dynamic models of the pneumatic control hardware, as well as an empirical attainment of the SRH-RJA dynamic model. Upon establishment of a parameter identifier, an adaptive controller and a nonlinear controller are formulated and tested in a simulation environment. Note that this preliminary control scheme is investigated solely in simulation settings.

6.1 Overall System Structure and Modeling

6.1.1 System Definition

In pneumatically operated soft robotic systems, there exist numerous methods to configure pneumatic hardware. Due to the fact that the formulation of plant models is dependent on the hardware configurations, which there exists no standard for it, it is common in the soft robotics field to derive the specific mathematical model for the system of interest.

The hardware configuration and the overall system structure adopted in this study are as shown in Figure 6.1. It is comprised of three subsystems in which the dynamics of each can be considered as three separate dynamics placed in a series configuration. The first dynamics is denoted i), and it involves the regulation of the pressure source and sink. It is comprised of a motor-driven fluidic pump, a vacuum pump, an accumulator, pressure sensors, and an internal pneumatic regulation hardware. Provided that the size of the accumulator is very large compared to the volume of the actuator, the pressure regulation dynamics of the source and the sink can be assumed to be negligible. In fluid mechanics lab environment, the pressure source is first provided from a large central pumping station to the lab and then regulated to provide a stable constant flow. The resultant pressure source to the system can then be considered as a constant pressure source with an infinitely large reservoir (i.e. infinite fluidic capacitance). In this project, the pressure source is regulated to be 800 mbar gauge (mbarg) pressure since it is the maximum allowable input pressure for the stable operation of TPU-MBSPA. Similarly, the atmosphere can be considered a pressure sink for SRH-RJA. This implies that the operating pressure range in controlling the SRH-RJA is 0 to 800 mbarg.

6.1.2 Pneumatic Control Dynamics

The second dynamic system involves the pressure dynamics of the pneumatic control hardware. Both the pressure source and the pressure sink are connected to the two inlets of the 3/2 pneumatic solenoid valve. With the resting state of the 3/2 valve connecting the SRH actuator pressure with the pressure sink, the internal pressure of the SRH actuator resets to atmospheric pressure and hence retracts to its original position when the valve is not excited. Upon actuating the 3/2 valve, the SRH actuator connects to the pressure source and hence will be pressurized to a maximum pressure of 1800 mbar absolute (mbara). Though the 3/2 valve used in this project is an on/off type, a high quality miniature solenoid valve (LHDB03333180, The Lee Co.) can achieve a response time of 3 ms, allowing a

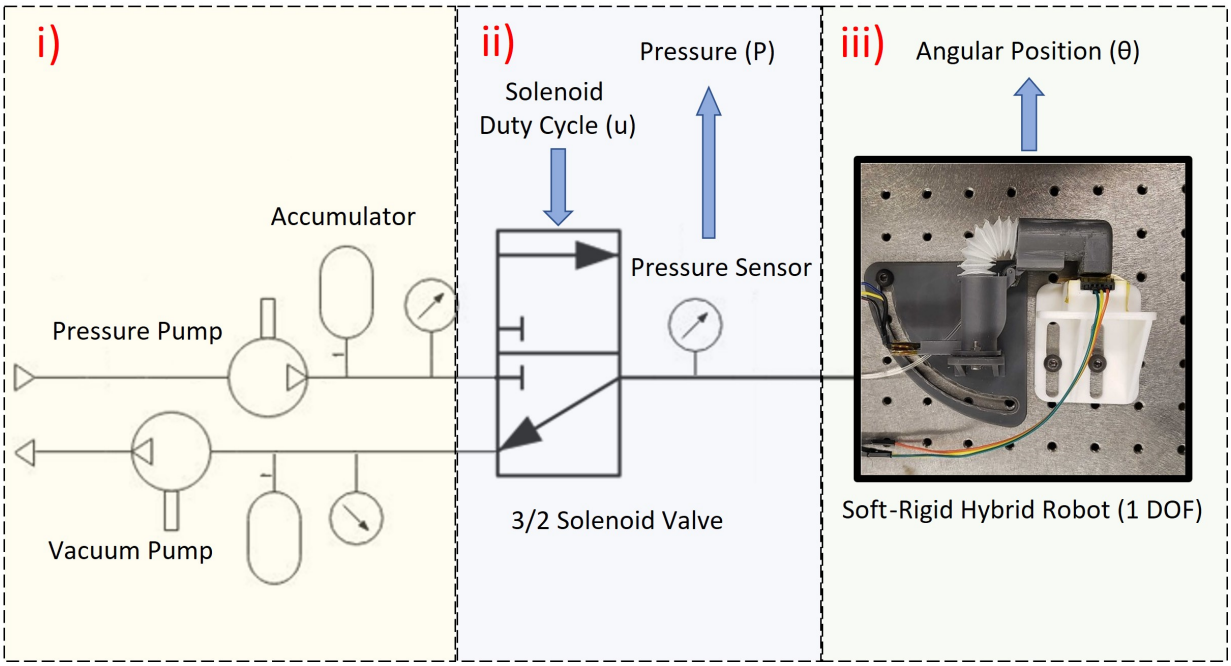


Figure 6.1: Overall system structure and the three dynamic subsystems. i) Represents the pressure and vacuum source considered constant in this study, ii) shows the 3/2 pneumatic solenoid valve switching between the pressure and the vacuum source. iii) Shows the pneumatic connection of the SRH-RJA to the pneumatic source via the solenoid valve.

proportional-like actuation up to 333 Hz. Hence, the pressure of the SRH actuator can be controlled via controlling the duty cycle signal (denoted u) of the 3/2 solenoid valve. The internal pressure of SRH actuator (denoted P) can be measured directly from the pressure sensor.

The derivation of the pneumatic hardware pressure dynamics can be done via formulation of control volume continuity analysis and isolating equations for the pressure dynamics. Assuming polytropic gas and constant density of 1.4 kg/m^3 at 25°C, the continuity equation can be written as

$$Q_i - Q_o = \frac{dV}{dt} + \frac{V}{\beta}\frac{dP}{dt} \tag{6.1}$$

where Q represents flow rate, $\frac{dV}{dt}$ is the boundary deformation of the control volume, V is the volume of the SRH actuator, β is bulk modulus, and $\frac{dP}{dt}$ is pressure derivative. By neglecting thermal processes and ignoring boundary deformation, the equation can be

simplified as

$$\frac{dP}{dt} = \frac{\gamma}{V}(Q_i - Q_o) \tag{6.2}$$

Applying the standard pneumatic valve models ANSI/NFPA T3.21.3 [148], the flow rates through the solenoid valve can be calculated. Noting that inlet flow is when the duty cycle of the solenoid valve is opened (i.e. uϵ[0,1]) and the outlet flow is when the solenoid is not actuated (i.e. 1-u), the inlet and outlet flow rates are defined as

$$\frac{Q_i = 114.5uC_v\sqrt{P(P_p - P)}}{\sqrt{T}} \tag{6.3}$$

$$\frac{Q_o = 114.5(1-u)C_v\sqrt{P_v(P_v - P)}}{\sqrt{T}} \tag{6.4}$$

where C_v is the flow coefficient of the solenoid valve, T is the operating temperature, P_p is the pressure of the source, and P_v is the pressure of the sink. Via substitution of (6.3) and (6.4) into (6.2) and upon simplification, the resultant pressure dynamics is a nonlinear equation as shown below:

$$\begin{aligned} \dot{P} &= f(P) - g(P)\,u \\ f(P) &= C\left(P_v P^3 - P_v^2 P^2\right)^{1/2} \\ g(P) &= C(P_p^3 - P^4)^{1/2} + C(P_v P^3 - P_v^2 P^2)^{1/2} \end{aligned} \tag{6.5}$$

where C is the lumped constant.

6.1.3 Soft Actuator Angle-Pressure Dynamics

The last subsystem involves the dynamic response of the SRH actuator upon receiving the output pressure of the pneumatic hardware system. The general behaviour of a SRH actuator can be described with a second order plant [149],[150]

$$\frac{\psi(s)}{P(s)} = \frac{b_0}{s^2 + a_1 s + a_0} \tag{6.6}$$

Note that ψ variable is used to represent the angular displacement to avoid confusion with the state estimation variable θ presented in later sections. However, the plant parameters b_0, a_1, and a_0 vary at different operating pressures. To capture this operation pressure-dependent angle-pressure dynamics of the SRH actuator, a series of angular

displacement responses of the SRH actuator were measured using a custom-made IMU at varied step pressure inputs. Upon post-processing of raw data, a set of second order plant parameters were attained using System Identification Toolbox in MATLAB. Using the Curve Fitting Toolbox in MATLAB, the pressure-dependent variation of the plant parameters was fitted into coefficients of exponential curves, A and B, using the skeleton function

$$A \cdot e^{B \cdot P} \tag{6.7}$$

where P is the operating pressure in mbarg. The results are as summarized in Table. 6.1.

Table 6.1: Summary of plant parameter variation fitted as a function of operating pressure.

Coefficient	b_0	a_1	a_0
A	3.07	8.86	11.99
B	0.0003334	0.001642	0.003791
R^2 Fitting	0.91	0.93	0.94

The step response of the parameter-varying second-order angle-pressure dynamics at varied pressure inputs are estimated using (6.7) and the results are as shown in Figure. 6.2.

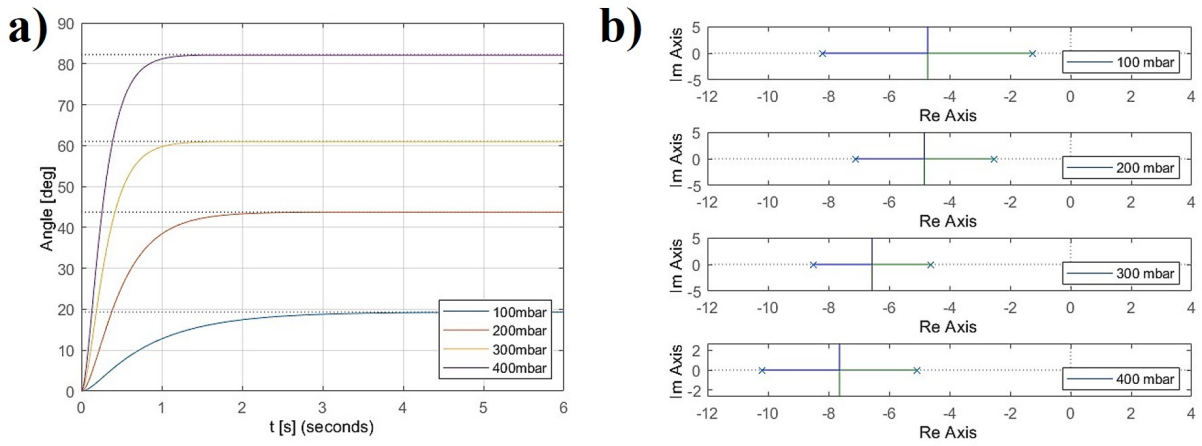


Figure 6.2: The resultant plots from the experimental data. i) The step response and ii) the root locus plots of skeleton parameter-varying plant at 4 different input pressures.

6.1.4 Control Objective

The equilibrium point for all dynamics of the system occurs when the system is not excited. Due to the control signal being the duty cycle at which the valve connects to the pressure source from the atmosphere, the soft actuator receives 0 gauge pressure when the 3/2 valve is not actuated. Due to the natural spring constant of the soft actuator, it regulates itself to a fully retracted position if not pressurized.

In the prospected applications of this system (i.e. in manipulators / humanoids / teleoperation), the system operates by the user/computer providing a desired angular displacement location, and the system tries to attain the desired positions. This then becomes a tracking problem. Based on the error of desired angular position and the angular position of the plant, the controller needs to be made such that it provides the actuation pressure required to reach the reference angular position. The output of the angle-pressure controller is then the reference pressure input for the pressure dynamics, in which another controller would be required to control the nonlinear pressure dynamics such that the output pressure of pneumatic hardware provides the required pressure to the actuator. This then becomes a cascaded control system with the inner feedback loop providing the required pressures calculated from the outer feedback loop providing the pressures required to track the angular position.

6.2 Parameter Identifier Design

All the components in the lumped constant C of pneumatic control hardware nonlinear dynamics are design parameters and constants attained with fluid mechanics assumptions. Provided that the pressure sensor provides the output pressure of the pressure dynamics subsystem, all parameters as well as the state of this subsystem are fully defined at all times.

The angle-pressure dynamics of the SRH actuator, however, is a parameter-varying plant. Hence a parameter identification (PI) method is required to provide an estimate of the plant parameter such that an adaptive control scheme can be utilized. In this case, the only parameters to be estimated would be b_0, a_1, a_0. The angular displacement output of the SRH actuator, ψ is attainable directly from the online processing of the integrated

IMU sensor. Formulating the static parametric model (SPM) from (6.6)

$$z = \frac{s^2}{\Lambda(s)}\varphi, \quad \theta^{*T} = [b_0, a_1, a_0]$$
$$\phi = \left[\frac{P}{\Lambda(s)}, \frac{-s}{\Lambda(s)}\varphi, \frac{-1}{\Lambda(s)}\varphi\right]^T$$

where $\Lambda(s)$ is a stable second-order filter. Such as $\Lambda(s) = (s+3)^2$. The estimation model is then expressed as

$$\hat{z}(t) = \theta^T \phi(t), \quad \theta^T = \left[\hat{b}_0, \hat{a}_1, \hat{a}_0\right]$$

Note that normalization was not used in this parameter identification task, because the plant is known to be stable and bounded, and the pressure input u is bounded by the pressure source and sink. For the estimation of the parameters, the Least Squares algorithm with forgetting factor and covariance resetting was used as follows

$$\dot{\theta}(t) = P(t)\varepsilon(t)\phi(t)$$
$$\dot{P}(t) = \beta P(t) - P(t)\phi(t)\phi^T\ (t)P(t)$$

where $\theta(0)$=θ_0 and P(0)=P_0=$Q_0^{-1} > 0$ and $\beta > 0$, with the following condition for covariance resetting

$$\text{Set } P(t_r^+) = P_0, t_r^+ \text{ is when } \lambda_{min} < 0.03 \text{ or } \lambda_{max} < 300$$

In this configuration, the PI will converge to true parameter values exponentially fast, should the input pressure signal is at least sufficiently rich of order 4, requiring a pressure signal comprised of at least two distinct frequencies. The simulation parameters were selected as

$$P_0 = 50I_{3x3}, \ \beta = 0.6, \ \theta^T(0) = [15\ 20\ 45]$$

The performance of the PI is tested with such input signal, P(t)=100sin(3.1t) + 75sin(1.8t+0.7) + 200 [mbar,g], as shown in Figure. 6.3:

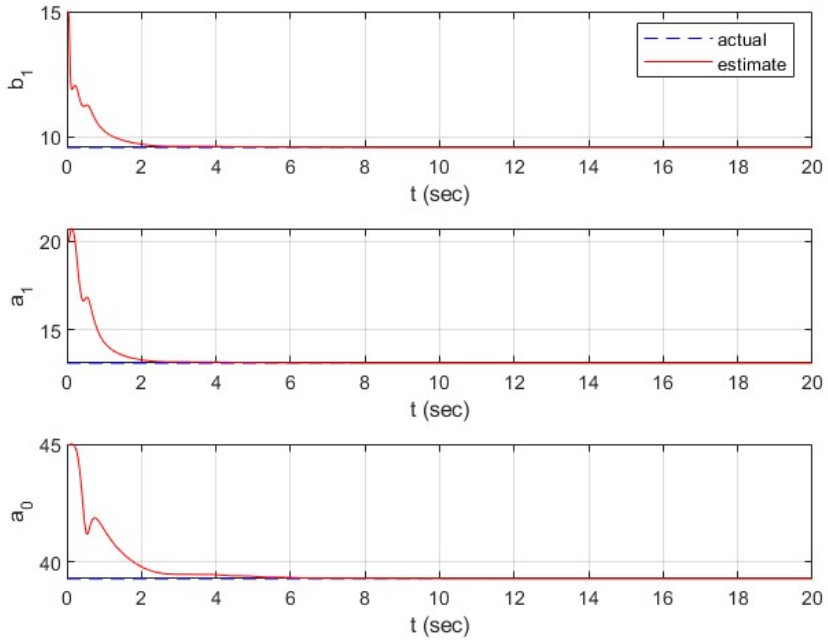


Figure 6.3: Parameter estimation results compared to the true parameter values. As expected, the parameter estimates converge to their true values exponentially fast.

6.3 Controller Design

This section provides a detailed design process and results of the cascade control utilized to attain the overall control objective. For the parameter-varying angle-pressure dynamics, an adaptive pole placement controller (APPC) is designed in which the outer feedback loop provides the pressure input required for the SRH actuator to reach the desired angle position set points. This desired pressure is then fed into the inner feedback loop to control the nonlinear dynamics of the pneumatic hardware control system such that the desired pressures are inputted to the SRH actuator.

6.3.1 APPC Design

In the prospected applications of the SRH actuator, the system receives a series of target angular positions for the SRH actuator to reach. This reference input can be represented as a sequence of reference constant angular positions. Hence, this is a tracking problem where the reference signal $y_m = constant$. Using the internal model principle, $Q_m = s$ satisfies the condition of driving $y_m Q_m = 0$. Keeping the coefficient of stable filter q in $Q_1 = s + q$ as a design variable, a steady-state APPC scheme can be derived. The tracking error can be expressed as

$$\begin{aligned} e_1 = y - y_m &= \frac{Z_p(s)\,Q_1(s)}{R_p(s)\,Q_m(s)}\bar{u} \\ e_1 &= \frac{b_0 s + q b_0}{s^3 + a_1 s^2 + a_0 s}\bar{u} \\ \bar{u} &= \frac{Q_m(s)}{Q_1(s)}u \end{aligned} \tag{6.8}$$

Then the steady-state realization of this error in canonical form allows the following equation

$$\begin{aligned} \dot{e} &= \begin{bmatrix} -a_1 & 1 & 0 \\ -a_0 & 0 & 1 \\ 0 & 0 & 0 \end{bmatrix}\hat{e} + \begin{bmatrix} 0 \\ b \\ qb \end{bmatrix}\bar{u} - K_o\left([1\ 0\ 0]\,\hat{e} - e_1\right) \\ \bar{u} &= -K_c\hat{e} \end{aligned} \tag{6.9}$$

Applying parameter identification and designing of pole locations for the error Luenberger observer, $\Delta_{obs} = (s + x)^3$ and the controller pole location, $\Delta_{cont} = (s + y)^3$, the adaptive gain matrices can be derived as

$$\hat{K}_o = \begin{bmatrix} 3x - \hat{a}_1 \\ 3x^2 - \hat{a}_0 \\ x^3 \end{bmatrix} \tag{6.10}$$

$$\hat{K}_c = \begin{bmatrix} 0 & 1 & q \\ 1 & q + \hat{a}_1 & q\hat{a}_1 \\ q & q\hat{a}_1 & \hat{a}_0 \end{bmatrix}^{-1} \begin{bmatrix} (3y - \hat{a}_1)/\hat{b}_0 \\ (3y^2 - \hat{a}_0)/\hat{b}_0 \\ y^3/\hat{b}_0 \end{bmatrix}$$

where $x > y > 0$ and the adaptive control law

$$u = \frac{Q_1(s)}{Q_m(s)}\bar{u} = -\hat{K}_c\frac{s + q}{s}\hat{e} \tag{6.11}$$

Upon investigating the speed of the plan pole locations (Figure. 6.2) and varying the design parameters of the internal model filter coefficients, and pole placement location of the observer and the controller, the following simulation design parameters are determined to provide the optimal response with minimal overshoot, fast rising time, and short settling time: $\Lambda(S) = (s+3)^2$, $Q_1(s) = s+4$, $\Delta_{obs} = (s+7)^3$, $\Delta_{obs} = (s+4)^3$. The plant response is as shown in Figure. 6.4. This promises a fast and stable capability of the Adaptive control method for controlling the SRH actuator, provided that the nonlinear pressure dynamics of the pneumatic hardware can be controlled to deliver the requested pressure fast enough.

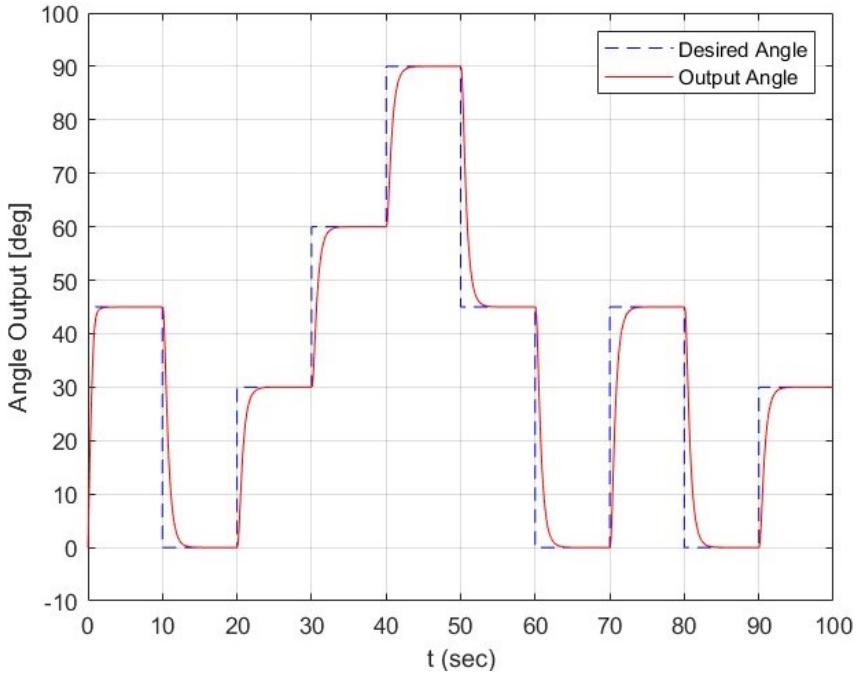


Figure 6.4: Performance of the State-Space APPC with driving the output angle of SRH actuator to desired target angular positions.

The performance of the adaptive error Luenberger observer as well as the parameter estimator is as shown in Figure. 6.5. The poles of error Luenberger observer are placed to be faster than that of the APPC controller, such that the observer attempts to provide the most updated, ideally converged state estimation to the controller. Note that despite the parameter estimates did not converge to the true parameter values due to the input signal not consisting of at least two distinct frequency contents, the control objective is met. The simulation took 24 seconds, and the response had 0% overshoot and settling time of $\epsilon[1.3, 4]$

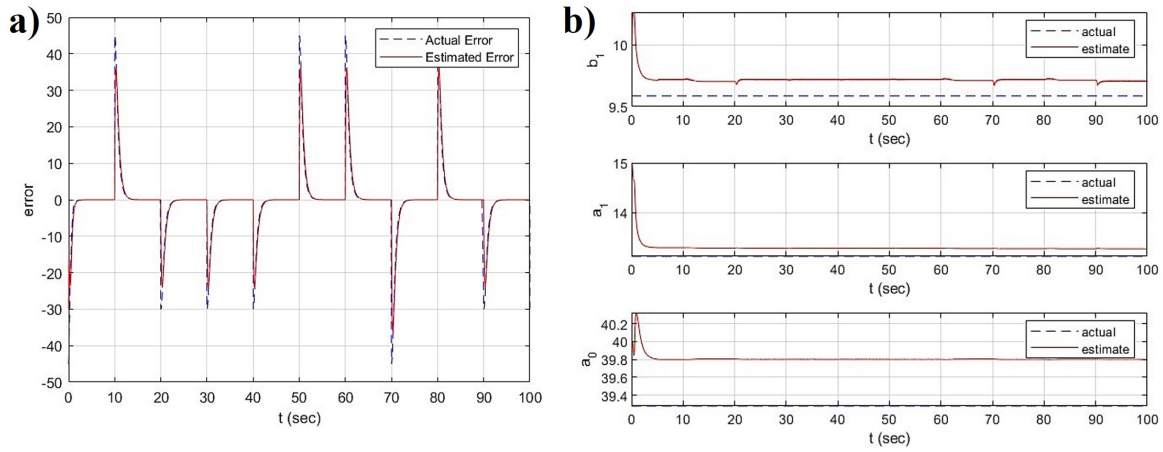


Figure 6.5: Performance of the a) Error Luenberger Observer and b) the Parameter Identifier.

6.3.2 Feedback Linearization Design

The pneumatic hardware needs to be controlled such that it provides the pressure requested by the APPC controller. To do so, the pneumatic 3/2 solenoid valve needs to be connected back and forth to the pressure source and the pressure sink via duty cycle solenoid control signal, u. The nonlinear pressure dynamics of this effect is as shown in (6.5). In this configuration, the pressure sensor directly provides the pressure output to the SRH actuator, which is the state of interest. Hence, the nonlinear dynamic system can be represented as

$$\begin{aligned} \dot{P}(t) &= f(P,u) \\ \dot{u} &= v \\ y &= h(P) = P \end{aligned} \tag{6.12}$$

where v is a new control signal. Due to the pressure sensor providing the output of interest, $\frac{\partial h(P)}{\partial P} = 1$, and because the Lie derivative $L_g h = \frac{\partial h}{\partial P}(P_0)g(P_0) \neq 0$ at any $P_0 > 0$, it has a relative degree of 1. This configuration then can be controlled using the feedback linearization method. The idea of feedback linearization is to cancel out all, if not some, of the effects caused by the nonlinear terms in the system [151]. By doing so, the nonlinearity is reduced and the system is expected to behave in a more linear fashion. The general feedback linearization control law is

$$u = \frac{1}{L_g L_f^{n-1} h(P)} \left(v - L_f^n h(P) \right) \tag{6.13}$$

Utilizing the fact that the relative degree 1, coordinate transformation can be performed to find feedback law v

$$\begin{aligned} \dot{z} &= 0z + v \\ v &= -Kz = -K(P - P_{APPC}) \end{aligned} \tag{6.14}$$

where K is the feedback linearization control gain, and P_{APPC} is the pressure requested by the APPC controller. The feedback linearization control law can be formulated by combining (6.12) with (6.13)

$$u = \frac{1}{g(P)}\left(v - f(P)\right) \tag{6.15}$$

The implementation of this feedback linearization is as shown in Figure. 6.6. Note that, to avoid singularity in the controller which can occur when $g(P) = 0$ when $P = 0$, all the pressure variables in nonlinear pressure dynamic subsystem were converted to absolute pressures instead of gauge pressures.

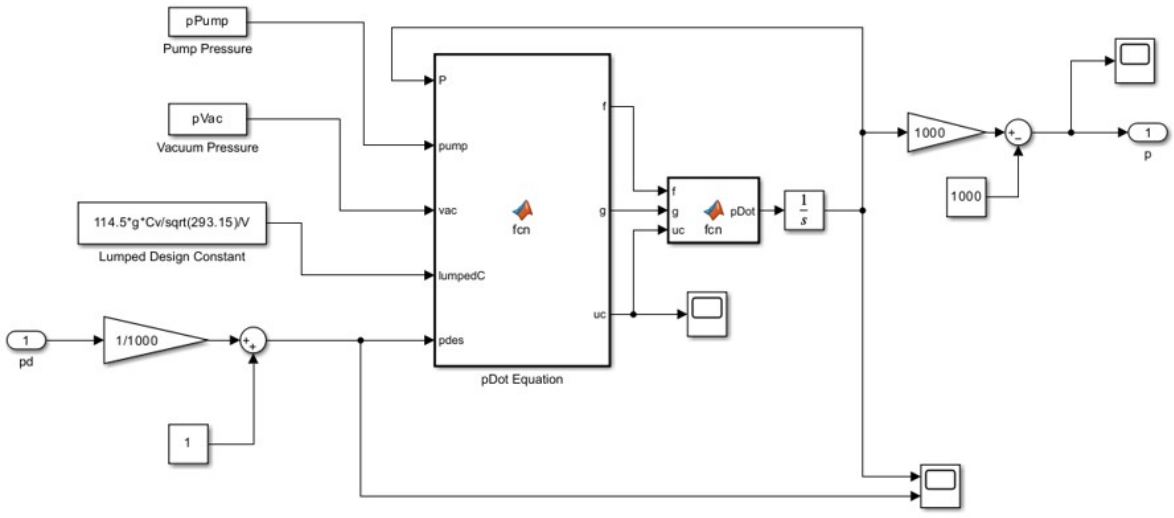


Figure 6.6: Implementation of nonlinear feedback linearization controller

The result of the nonlinear pressure controller is as shown in Figure. 6.7. Because the poles of the controller were all placed at -4, a gain of at least 5 is found to be fast enough for the feedback linearization controller.

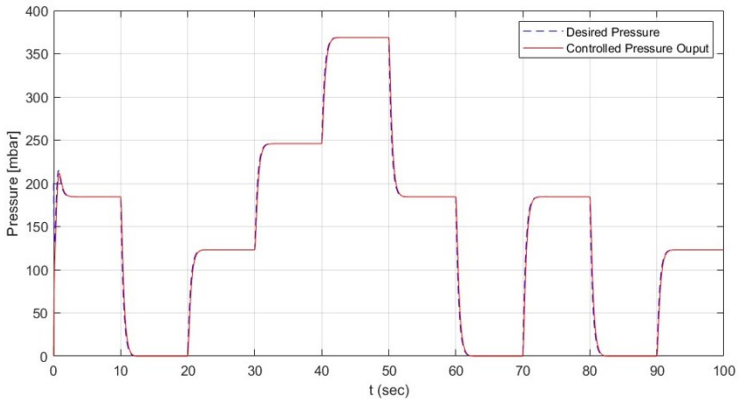


Figure 6.7: Implementation of nonlinear feedback linearization controller

6.4 Simulation Results and Discussion

Upon successful implementation of each subsystem individually, all components required to acquire the overall control objective were integrated into one simulation environment (Figure. 6.8).

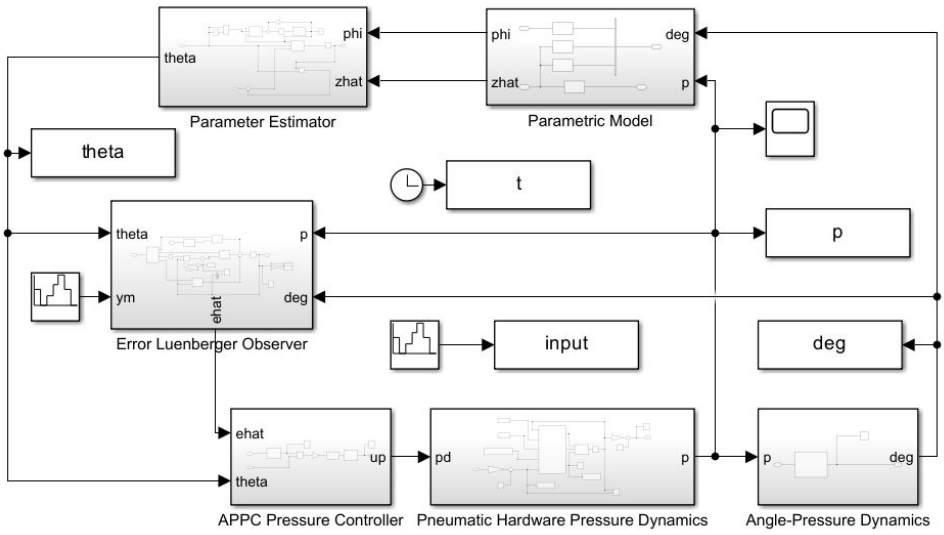


Figure 6.8: Overall simulation environment incorporating all subsystems used in this study

As shown in the key results, Figure. 6.9, the overall control objective of driving the SRH actuator to provide the requested angular displacements are successfully attained. A 100-second simulation required 44 seconds to compute, APPC controller was able to predict the pressure input required to drive the SRH actuator to successfully track the desired angular displacements with minimal overshoot and fast rising and settling times. As expected, the error Luenberger observer of the APPC controller, parameter identifier, and the nonlinear feedback linearization controller were able to provide satisfiable results.

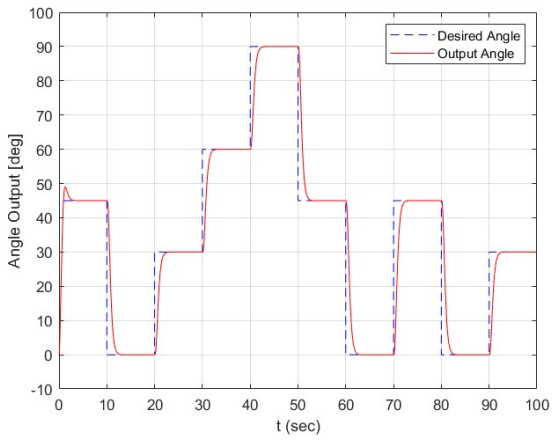


Figure 6.9: Performance of the overall system in tracking of reference angles

6.5 Conclusion

In this project, the capability of utilizing adaptive control and nonlinear control methods to fulfill the task of tracking desired angular displacements of a soft-rigid hybrid actuator was demonstrated. With the help of Parameter Identifier, an APPC Controller was designed and demonstrated its ability to predict the pressures required to drive the angle-pressure dynamics of SRH actuator to achieve the desired positions. With the nonlinear feedback linearization controller design, the severe nonlinear effects of the pneumatic control hardware were cancelled out and allowed the nonlinear pneumatic control system to closely follow the desired pressures received from the APPC controller. However, the controller design and tests were carried out only in a simulated environment. An additional real-life implementation should be investigated as future works, incorporating all practical parameters such as hysteresis, maximum actuation frequency, and noise.

Chapter 7

Conclusions and Recommendations

7.1 Thesis Conclusions

The main goal of this thesis was to investigate various types of soft robotic actuators existing in the newly emerging field of soft robotics for the purpose of identifying the critical elements currently lacking in the state of the art technologies, and tackling the identified challenges with a novel unconventional approach. The presented thesis work guided through the entire journey of ideation, conceptualization, investigation, and sharing of a multi-staged development of Soft-Rigid Hybrid (SRH) robotics. Upon an extensive literature review of a wide range of soft actuators and analyzing the fundamental principles, advantages, and drawbacks of each technology, the justification was provided for the selection of soft pneumatic actuator in this study. Keeping in mind the objective of developing an innovative embodiment using the soft-rigid hybrid robotics approach, further segregation of existing soft pneumatic actuators suitable for the proposed approach narrowed down to multilayered bellow-shaped soft pneumatic actuators (MBSPA).

As the first stage of the development progress, the details of the investigation, key design features, and the results of the novel Thermoplastic Polyurethane Multilayered Bellow-shaped Soft Pneumatic Actuator (TPU-MBSPA) was shared. By first exploring the existing fabrication methods, the working principle and fundamental structure of layered soft pneumatic actuators were thoroughly examined. After a careful investigation of material selection for identification of the most suitable material for constructing the TPU-MBSPA, Teflon-coated material was selected as the insert layer material upon evaluation of all material candidates with reasoned criteria. Upon introduction of the multi-layered fabrication technique, the resultant TPU-MBSPA provided a highly efficient displacement

motion, in which all key design variables and fabrication details were shared in this thesis and as a journal article submitted to the soft robotics journal to contribute expansion of the field.

For the purpose of further advancing the understanding of the TPU-MBSPA as well as adopting hyperelastic models toward numerical simulation of estimating the expansion behavior, an extensive material characterization was conducted. With the provision of reasonable justification for simplification, uniaxial tensile tests were conducted according the the standardized methods. Additional investigations were carried out to confirm the validity of the simplifications, isotropicity, and independence of increased temperature. The numerical simulation model, which was based on the material models formulated using the experimentally obtained data, accurately predicted the expansion performance of the TPU-MBSPA. To confirm the generous estimation of the simulation results, additional displacement experiments were conducted for detailed comparison. In addition, an alternative application was investigated where the TPU-MBSPA was utilized as a displacement sensor. The results of this investigation showcased the versatility and the potential of a wide spectrum of applications beyond the primary function of the TPU-MBSPA. Through this comprehensive study, the TPU-MBSPA emerged as a promising soft pneumatic actuator with a wide range of practical applications in the field of robotics and beyond.

With the TPU-MBSPA invented, the preliminary investigations conducted, and limitations of the state of the art soft grippers reviewed, the first stage of SRH robotics approach was explored via the invention of SRH Revolute Joint Actuator (SRH-RJA) and SRH Prismatic Joint Actuator (SRH-PJA). The detailed philosophy, design, and construction of each joint actuators were shared. With the preliminary investigation of SRH-RJA identifying the significant of radial bulging phenomenon, additional designs were carried out to mitigate the occurrence of the disruption. Using both the bio-inspired armadillo-casing and the embedded casing methods, the force output of SRH-RJA was improved significantly. The choice of the material comprising the rigid structures were also justified focusing on the practicality of the proposed device.

For the purpose of evaluating the novelty, efficiency, and superiority of the proposed design, performances of the SRH-RJA and SRH-PJA were tested extensively. Using the methods commonly adopted for characterization of soft pneumatic actuators, such as quasi-static displacement characterization, blocked-force output, and variable joint-stiffness, the key characteristics of the joint actuators were fully defined and compared with other soft-rigid hybrid robots in the literature. All test setups and procedures were shared in the thesis in detail. To contribute further, additional tests were conducted evaluating the dynamic characteristics of joint actuators such as frequency-based displacement characteristics, durability, and power density. To validate the practicality aspect of the proposed

technology, the SRH-RJAs were utilized to formulate a 3-point SRH Gripper (SRHG). Upon establishment of sensors and communication protocols, the manipulatively, varied joint stiffness, and the compliance of the 3-point SRHG was demonstrated using a wide range of objects of various sizes, weights, and stiffness.

Leveraging the modular capability of the SRH joint actuators, a naturally compliant dexterous anthropomorphic hand was designed using the Modular SRH (MSRH) approach. Utilizing that each SRH-RJA provides 1 active degrees of freedom (DOF), this end-effector was capable of providing up to 21 actively controlled DOF, in which the number of actively controlled DOF was easily customizable fundamentally. This MSRH approach allowed the robotic hand to possess an inherently soft and compliant interface suitable for pHRI while maintaining the structural rigidity of the robot with the usage of rigid skeletons. The details of the design rationale, fabrication and assembly methods, and evaluation of the first prototype were investigated and shared. Even though the presented prototype was scaled to be 125 % of the average human hand, the mechanical components only weigh less than 450 g.

The modular design approach allowed the MSRH hand to possess low manufacturing costs and a short lead time. Creation of the presented prototype costed less than $100 CAD and was built in three days from scratch with two-person labour. The usage of pneumatic soft robotic actuators also provided flexibility over choosing the number of controlled DOF and joint coupling. This hence provided a new angle to tackle spatial constraint that normally arises in robotic hand design with increased anthropomorphism. Lastly, the dexterity of the proposed hand was demonstrated by evaluating the hand using taxonomies highly relevant to replicating tasks humans perform daily, in which all tasks specified in multiple taxonomies were all achievable.

Despite that the demonstrations in this thesis were mostly done in a controlled lab environment and hence complex control algorithms were not necessary, a preliminary pneumatic control strategy was studied to pave the way for practical applications of the proposed SRH approach in the future. The goal of this study was to provide a precedent, pioneering and paving the development of the SRH robots toward fully automated system using adaptive control. For simplicity, the applicability of the investigated pneumatic control strategy was specifically limited to controlling a 1-DOF SRH-RJA. Upon formulation of the overall system structure and deriving the dynamics models of the pneumatic control hardware scheme, experiments were conducted to empirically attain the dynamic model of SRH-RJA at varied operating points. Upon establishment of a parameter identifier, an adaptive controller and a nonlinear controller were formulated and tested in a simulation environment. The capability of utilizing adaptive control and nonlinear control methods to fulfill the task of tracking desired angular displacements of a soft-rigid hybrid actuator

was then demonstrated. With the Parameter Identifier, the APPC controller demonstrated its ability to accurately predict the pressures required for driving the angle-pressure dynamics of SRH-RJA. Following the APPC controller, the nonlinear feedback linearization controller suppressed the severe nonlinear effects innate to SRH-RJA and allowed the nonlinear pneumatic control system to closely follow the desired pressures received from the APPC controller. Though all investigation of this control scheme was done in a simulated environment, the preliminary investigation proved the potential of applying adaptive control methods for controlling of the proposed SRH robots.

Overall, the long journey of investigating a novel approach toward pioneering of a new field successfully provided numerous valuable insights, demonstrations, and promising results of the proposed technology. The presented works not only provided a precedent with the detailed development progress following the standard protocols, but went beyond to establish new methods and procedures contributing greatly toward promoting and expanding the knowledge in the newly emerging research field.

7.2 Recommendations

The methods presented in this thesis provided successful precedents of TPU-MBSPA, SRH robotics approach, and MSRH robotics approach, each with promising results. While the proposed technology can be applied to infinitely many number of applications, the investigations were still relatively preliminary. Many hurdles need to be overcome for this preceding technology to be adopted in real-world applications. The following recommendations are based on the limitations and obstacles of the current state of the technology which were perceived over the 2 years of observation during the development period.

First and foremost, the fabrication method of TPU-MBSPA must be improved. Despite the efforts to create novel fabrication methods to reduce lead time and improve ease of fabrication, the nature of layered manufacturing approach requires stacking of layers, which requires a tedious and time consuming labour. The most monotonous part of the fabrication process lies with the preparation of the layered materials as well as concentric alignment process. While the actual heat-pressing process takes up to a minute or two, the aforementioned processes are very repetitive and slow in nature. For this technology to be more favourable to others not yet involved in this direction, additional extensive investigation of alternatives or improved fabrication methods should be carried out to significantly improve the lead time of making the TPU-MBSPAs. As a first step of mitigating lead time, I would suggest creating either a metallic or heat-resistant die for easier alignment

during stacking of layers. While this can be of any shape, a good inspiration may be perhaps from Ring Toss type of design. To shorten the time of layered material preparation, either a high-precision plotter or an alternative equipment such as a laser cutter can be investigated. Lastly, in the event where TPU-MBSPA is unable to provide high enough of torque and suffers greatly from radial bulging, the structural layer can be substituted with more rigid material.

In applications where the soft robot only needs to provide simple open-loop gripping or grasping, there is no need for a complicated pneumatic hardware control. However, in more advanced robotic applications, real-life implementation of the pneumatic hardware control must be performed. While the preliminary investigation of the proposed adaptive controller showed great promise for controlling the 1-DOF SRH-RJA, the study was greatly simplified to simply test the capability of adaptive controllers. To make the simulation model more realistic, MATLAB simulink tools such as Simscape Fluids should be used to incorporate the effects of solenoid chattering, and other variances. In practice, there will be a number of rapidly changing variables such as inertial gravity effects, hysteresis, solenoid chattering, maximum actuation frequency, process noise, and measurement noises. I would recommend starting with the proposed miniature 3/2 valve from Lee Co, controlled with the Arduino Pulse-Width Modulation signals at a fixed control frequencies, with actuation duty cycle being the control signal.

As for the applications to adopt the proposed SRH and MSRH approach, I would suggest a total of five directions. The first would be to leverage the lego-like modularity of the technology to formulate a creative tool for educational purposes. The proposed technology can be understood by upper-year undergraduate students, given sufficient guidance is provided (such as ME/MTE380). A modular educational toolkit can be used to teach soft robotics to the next generation students, allowing the students to occasionally depart from old traditional Engineering methods. The next application is upper limb prosthesis. While the proposed MSRH hand can be provided up to 21 actively controlled DOF, it can be simplified to provide only the key gripping and grasping motions required for assisting daily lives of amputees. In this direction, an array of surface Electromyography (sEMG) systems and classification or machine learning methods can be used to provide preset motions using the robotic device. The proposed technology can also be utilized in mitigating Lymphedema patients, if shaped in a format where it can provide appropriate motion and forces onto the targeted extremities. Particularly, the mild compression and shear motion provided lymphedema specialists would be replicated.

The last two prospected directions are tele-operated robotic manipulation and social robotics. Using an IR based camera combined with classification methods, or via IMU-integrated gloves, the angular positions of each finger joints can be acquired, in which can be translated into the soft robotic device. This would allow robots to be utilized in applications such as remote surgery. Similarly, the proposed device can be implemented into social robots such as humanoid robots, to attain safe phyiscal Human-Robot Interaction for safe operation and human-robot coexistence.

References

[1] M. Li, A. Milojević, and H. Handroos, "Robotics in manufacturing-the past and the present," *Technical, Economic and Societal Effects of Manufacturing 4.0*, pp. 85–95, 1 2020.

[2] M. Ceccarelli, "A historical perspective of robotics toward the future," *Journal of Robotics and Mechatronics*, vol. 13, pp. 299–313, 6 2001.

[3] A. Gasparetto, L. Scalera, A. Gasparetto, and L. Scalera, "A brief history of industrial robotics in the 20th century," *Advances in Historical Studies*, vol. 8, pp. 24–35, 1 2019.

[4] N. G. Hockstein, C. G. Gourin, R. A. Faust, and D. J. Terris, "A history of robots: From science fiction to surgical robotics," *Journal of Robotic Surgery*, vol. 1, pp. 113–118, 3 2007.

[5] T. D. Veiga, J. H. Chandler, P. Lloyd, G. Pittiglio, N. J. Wilkinson, A. K. Hoshiar, R. A. Harris, and P. Valdastri, "Challenges of continuum robots in clinical context: a review," *Progress in Biomedical Engineering*, vol. 2, p. 032003, 7 2020.

[6] A. Pauliková, Z. G. Babel'ová, and M. Ubárová, "Analysis of the impact of human–cobot collaborative manufacturing implementation on the occupational health and safety and the quality requirements," *International Journal of Environmental Research and Public Health*, vol. 18, pp. 1–15, 2 2021.

[7] G. M. Whitesides, "Soft robotics," *Angewandte Chemie International Edition*, vol. 57, pp. 4258–4273, 4 2018.

[8] Y. Zhou and H. Li, "A scientometric review of soft robotics: Intellectual structures and emerging trends analysis (2010–2021)," *Frontiers in Robotics and AI*, vol. 9, p. 868682, 5 2022.

[9] O. Yasa, Y. Toshimitsu, M. Y. Michelis, L. S. Jones, M. Filippi, T. Buchner, and R. K. Katzschmann, "An overview of soft robotics," *https://doi.org/10.1146/annurev-control-062322-100607*, vol. 6, pp. 1–29, 5 2023.

[10] N. El-Atab, R. B. Mishra, F. Al-Modaf, L. Joharji, A. A. Alsharif, H. Alamoudi, M. Diaz, N. Qaiser, and M. M. Hussain, "Soft actuators for soft robotic applications: A review," *Advanced Intelligent Systems*, vol. 2, p. 2000128, 10 2020.

[11] M. S. Xavier, C. D. Tawk, A. Zolfagharian, J. Pinskier, D. Howard, T. Young, J. Lai, S. M. Harrison, Y. K. Yong, M. Bodaghi, and A. J. Fleming, "Soft pneumatic actuators: A review of design, fabrication, modeling, sensing, control and applications," *IEEE Access*, vol. 10, pp. 59 442–59 485, 2022.

[12] J. Zhou, S. Chen, and Z. Wang, "A soft-robotic gripper with enhanced object adaptation and grasping reliability," *IEEE Robotics and Automation Letters*, vol. 2, pp. 2287–2293, 10 2017.

[13] P. Polygerinos, Z. Wang, K. C. Galloway, R. J. Wood, and C. J. Walsh, "Soft robotic glove for combined assistance and at-home rehabilitation," *Robotics and Autonomous Systems*, vol. 73, pp. 135–143, 11 2015.

[14] Z. Ma and D. Sameoto, "A review of electrically driven soft actuators for soft robotics," *Micromachines 2022, Vol. 13, Page 1881*, vol. 13, p. 1881, 11 2022.

[15] M. Li, A. Pal, A. Aghakhani, A. Pena-Francesch, and M. Sitti, "Soft actuators for real-world applications," *Nature Reviews Materials 2021 7:3*, vol. 7, pp. 235–249, 11 2021.

[16] H. Rodrigue, W. Wang, M. W. Han, T. J. Kim, and S. H. Ahn, "An overview of shape memory alloy-coupled actuators and robots," *https://home.liebertpub.com/soro*, vol. 4, pp. 3–15, 3 2017.

[17] J. M. Jani, M. Leary, A. Subic, and M. A. Gibson, "A review of shape memory alloy research, applications and opportunities," *Materials & Design (1980-2015)*, vol. 56, pp. 1078–1113, 4 2014.

[18] S. K. Ghosh, "Isotropic-nematic transition in liquid crystals," *Recent Developments in Condensed Matter Physics*, pp. 85–96, 1981.

[19] R. S. Kularatne, H. Kim, J. M. Boothby, and T. H. Ware, "Liquid crystal elastomer actuators: Synthesis, alignment, and applications," *Journal of Polymer Science Part B: Polymer Physics*, vol. 55, pp. 395–411, 3 2017.

[20] S. Wu, G. L. Baker, J. Yin, and Y. Zhu, "Fast thermal actuators for soft robotics," *https://home.liebertpub.com/soro*, vol. 9, pp. 1031–1039, 12 2022.

[21] B. P. Edmonds and A. L. Trejos, "Design of an active cooling system for thermally activated soft actuators," *IEEE International Conference on Rehabilitation Robotics*, vol. 2019-June, pp. 368–373, 6 2019.

[22] X. Wang, N. Jiao, S. Tung, and L. Liu, "Photoresponsive graphene composite bilayer actuator for soft robots," *ACS Applied Materials and Interfaces*, vol. 11, pp. 30 290–30 299, 8 2019.

[23] Y. Yan, Y. Wu, Q. Wang, Y. Wang, Y. Zhan, Z. Sun, L. Yu, and X. Wang, "Photoresponsive bilayer soft actuators synergic fluorescence and shape change towards biomimetic untethered camouflage robots," *Advanced Optical Materials*, vol. 11, p. 2203019, 4 2023.

[24] Y. Huang, Q. Yu, C. Su, J. Jiang, N. Chen, and H. Shao, "Light-responsive soft actuators: Mechanism, materials, fabrication, and applications," *Actuators 2021, Vol. 10, Page 298*, vol. 10, p. 298, 11 2021.

[25] Z. Tang, Z. Gao, S. Jia, F. Wang, and Y. Wang, "Graphene-based polymer bilayers with superior light-driven properties for remote construction of 3d structures," *Advanced Science*, vol. 4, p. 1600437, 5 2017.

[26] Z. . Ma, D. A. Sameoto, Z. Ma, and D. Sameoto, "A review of electrically driven soft actuators for soft robotics," *Micromachines 2022, Vol. 13, Page 1881*, vol. 13, p. 1881, 11 2022.

[27] M. C. Yip and G. Niemeyer, "On the control and properties of supercoiled polymer artificial muscles," *IEEE Transactions on Robotics*, vol. 33, pp. 689–699, 6 2017.

[28] X. Ji, X. Liu, V. Cacucciolo, M. Imboden, Y. Civet, A. E. Haitami, S. Cantin, Y. Perriard, and H. Shea, "An autonomous untethered fast soft robotic insect driven by low-voltage dielectric elastomer actuators," *Science Robotics*, vol. 4, 12 2019.

[29] R. Kornbluh, R. Pelrine, Q. Pei, S. Oh, J. D. J. R. Kornbluh, J. Joseph, and R. Peirine, "Ultrahigh strain response of field-actuated elastomeric polymers," *https://doi.org/10.1117/12.387763*, vol. 3987, pp. 51–64, 6 2000.

[30] M. S. Xavier, C. D. Tawk, A. Zolfagharian, J. Pinskier, D. Howard, T. Young, J. Lai, S. M. Harrison, Y. K. Yong, M. Bodaghi, and A. J. Fleming, "Soft pneumatic actuators: A review of design, fabrication, modeling, sensing, control and applications," *IEEE Access*, vol. 10, pp. 59 442–59 485, 2022.

[31] S. I. Rich, R. J. Wood, and C. Majidi, "Untethered soft robotics," *Nature Electronics 2018 1:2*, vol. 1, pp. 102–112, 2 2018.

[32] D. Rus and M. T. Tolley, "Design, fabrication and control of soft robots," *Nature 2015 521:7553*, vol. 521, pp. 467–475, 5 2015.

[33] C. Majidi, "Soft-matter engineering for soft robotics," *Advanced Materials Technologies*, vol. 4, p. 1800477, 2 2019.

[34] P. S. Lee, R. Z. Gao, A. Colpitts, R. W. Murdock, D. Dittmer, A. Schirm, J. Y. Tung, and C. L. Ren, "Air microfluidics-enabled soft robotic transtibial prosthesis socket liner toward dynamic management of residual limb contact pressure and volume fluctuation," *Biomicrofluidics*, vol. 16, p. 034107, 6 2022.

[35] A. A. Stokes, R. F. Shepherd, S. A. Morin, F. Ilievski, and G. M. Whitesides, "A hybrid combining hard and soft robots," *Soft Robotics*, vol. 1, pp. 70–74, 3 2014.

[36] M. S. Xavier, C. D. Tawk, Y. K. Yong, and A. J. Fleming, "3d-printed omnidirectional soft pneumatic actuators: Design, modeling and characterization," *Sensors and Actuators A: Physical*, vol. 332, p. 113199, 12 2021.

[37] H. D. Yang and A. T. Asbeck, "A layered manufacturing approach for soft and soft-rigid hybrid robots," *Soft Robotics*, vol. 7, pp. 218–232, 4 2020.

[38] P. H. Nguyen and W. Zhang, "Design and computational modeling of fabric soft pneumatic actuators for wearable assistive devices," *Scientific Reports 2020 10:1*, vol. 10, pp. 1–13, 6 2020.

[39] S. Becker, T. Ranzani, S. Russo, and R. J. Wood, "Pop-up tissue retraction mechanism for endoscopic surgery," *IEEE International Conference on Intelligent Robots and Systems*, vol. 2017-September, pp. 920–927, 12 2017.

[40] T. Ranzani, S. Russo, F. Schwab, C. J. Walsh, and R. J. Wood, "Deployable stabilization mechanisms for endoscopic procedures," *Proceedings - IEEE International Conference on Robotics and Automation*, pp. 1125–1131, 7 2017.

[41] J. Rogatinsky, K. Gomatam, Z. H. Lim, M. Lee, L. Kinnicutt, C. Duriez, P. Thomson, K. McDonald, and T. Ranzani, "A collapsible soft actuator facilitates performance in constrained environments," *Advanced Intelligent Systems*, vol. 4, p. 2200085, 10 2022.

[42] S. Zaidi, M. Maselli, C. Laschi, and M. Cianchetti, "Actuation technologies for soft robot grippers and manipulators: A review," *Current Robotics Reports 2021 2:3*, vol. 2, pp. 355–369, 5 2021.

[43] H. Li, D. Xie, and Y. Xie, "A soft pneumatic gripper with endoskeletons resisting out-of-plane bending," *Actuators 2022, Vol. 11, Page 246*, vol. 11, p. 246, 8 2022.

[44] H. Su, X. Hou, X. Zhang, W. Qi, S. Cai, X. Xiong, and J. Guo, "Pneumatic soft robots: Challenges and benefits," *Actuators 2022, Vol. 11, Page 92*, vol. 11, p. 92, 3 2022.

[45] M. S. Xavier, A. J. Fleming, and Y. K. Yong, "Finite element modeling of soft fluidic actuators: Overview and recent developments," *Advanced Intelligent Systems*, vol. 3, p. 2000187, 2 2021.

[46] M. A. Robertson, H. Sadeghi, J. M. Florez, and J. Paik, "Soft pneumatic actuator fascicles for high force and reliability," *Soft Robotics*, vol. 4, pp. 23–32, 3 2017.

[47] M. A. Bell, B. Gorissen, K. Bertoldi, J. C. Weaver, and R. J. Wood, "A modular and self-contained fluidic engine for soft actuators," *Advanced Intelligent Systems*, vol. 4, p. 2100094, 1 2022.

[48] H. Li, J. Yao, P. Zhou, X. Chen, Y. Xu, and Y. Zhao, "High-force soft pneumatic actuators based on novel casting method for robotic applications," *Sensors and Actuators A: Physical*, vol. 306, p. 111957, 5 2020.

[49] A. Gunderman, J. Collins, A. Myers, R. Threlfall, and Y. Chen, "Tendon-driven soft robotic gripper for blackberry harvesting," *IEEE Robotics and Automation Letters*, vol. 7, pp. 2652–2659, 4 2022.

[50] J. Wang and A. Chortos, "Control strategies for soft robot systems," *Advanced Intelligent Systems*, vol. 4, p. 2100165, 5 2022.

[51] A. Al-Ibadi, S. Nefti-Meziani, and S. Davis, "The design, kinematics and torque analysis of the self-bending soft contraction actuator," *Actuators 2020, Vol. 9, Page 33*, vol. 9, p. 33, 4 2020.

[52] T. G. Thuruthel, Y. Ansari, E. Falotico, and C. Laschi, "Control strategies for soft robotic manipulators: A survey," *Soft Robotics*, vol. 5, pp. 149–163, 4 2018.

[53] M. Tiboni and C. Amici, "Soft gloves: A review on recent developments in actuation, sensing, control and applications," *Actuators 2022, Vol. 11, Page 232*, vol. 11, p. 232, 8 2022.

[54] N. Guo, Z. Sun, X. Wang, E. H. K. Yeung, M. K. T. To, X. Li, and Y. Hu, "Simulation analysis for optimal design of pneumatic bellow actuators for soft-robotic glove," *Biocybernetics and Biomedical Engineering*, vol. 40, pp. 1359–1368, 10 2020.

[55] W. Park, S. Seo, and J. Bae, "A hybrid gripper with soft material and rigid structures," *IEEE Robotics and Automation Letters*, vol. 4, pp. 65–72, 1 2019.

[56] H. Wang, F. J. Abu-Dakka, T. L. Nguyen, V. Kyrki, and H. Xu, "A novel soft robotic hand design with human-inspired soft palm: Achieving a great diversity of grasps," *IEEE Robotics and Automation Magazine*, vol. 28, pp. 37–49, 6 2021.

[57] J. Hughes, U. Culha, F. Giardina, F. Guenther, A. Rosendo, and F. Iida, "Soft manipulators and grippers: A review," *Frontiers Robotics AI*, vol. 3, p. 223168, 11 2016.

[58] R. Z. Gao, V. N. T. Mai, N. Levinski, J. M. Kormylo, R. W. Murdock, C. R. Dickerson, and C. L. Ren, "A novel air microfluidics-enabled soft robotic sleeve: Toward realizing innovative lymphedema treatment," *Biomicrofluidics*, vol. 16, p. 34101, 5 2022.

[59] T. Ngah, "3919 bemis thermally activated sewfree adhesive tape datasheet v2," Bemis Associates Inc., Tech. Rep., 8 2009.

[60] H. Lee, N. Oh, and H. Rodrigue, "Expanding pouch motor patterns for programmable soft bending actuation: Enabling soft robotic system adaptations," *IEEE Robotics and Automation Magazine*, vol. 27, pp. 65–74, 12 2020.

[61] P. Lee, C. Sjaarda, R. Gao, J. Dupuis, M. Rukavina-Nolsoe, and C. Ren, "Soft-rigid hybrid revolute and prismatic joints using multilayered bellow soft pneumatic actuators: Design, characterization, and its application as soft-rigid hybrid gripper," *Soft Robotics (Manuscript Under Review)*, 2023.

[62] M. S. Xavier, A. J. Fleming, and Y. K. Yong, "Finite element modeling of soft fluidic actuators: Overview and recent developments," *Advanced Intelligent Systems*, vol. 3, p. 2000187, 2 2021.

[63] H. HIBBITT, "Abaqus/epgen–a general purpose finite element code with emphasis on nonlinear applications," *Structural Integrity Research of the Electric Power Research Institute*, pp. 271–297, 1 1984.

[64] S. E. Bechtel and R. L. Lowe, "What is a continuum?" *Fundamentals of Continuum Mechanics*, pp. 3–4, 1 2015.

[65] S. E. Bechtel and R. Lowe, "Nonlinear elasticity," *Fundamentals of Continuum Mechanics*, pp. 181–195, 1 2015.

[66] H. Shin, J. B. Kim, S. J. Kim, and K. Y. Rhee, "A simulation-based determination of cap parameters of the modified drucker–prager cap model by considering specimen barreling during conventional triaxial testing," *Computational Materials Science*, vol. 100, pp. 31–38, 4 2015.

[67] J. C. Lagarias, J. A. Reeds, M. H. Wright, and P. E. Wright, "Convergence properties of the nelder–mead simplex method in low dimensions," *https://doi.org/10.1137/S1052623496303470*, vol. 9, pp. 112–147, 7 2006.

[68] D. Gutierrez-Lemini, "Engineering viscoelasticity," *Engineering Viscoelasticity*, pp. 1–353, 1 2014.

[69] S. P. Marques and G. J. Creus, "Computational viscoelasticity," *SpringerBriefs in Applied Sciences and Technology*, pp. iv–v, 2012.

[70] M. T. Shaw and W. J. MacKnight, "Introduction to polymer viscoelasticity: Third edition," *Introduction to Polymer Viscoelasticity: Third Edition*, pp. 1–316, 9 2005.

[71] P. Moseley, J. M. Florez, H. A. Sonar, G. Agarwal, W. Curtin, and J. Paik, "Modeling, design, and development of soft pneumatic actuators with finite element method," *Advanced Engineering Materials*, vol. 18, pp. 978–988, 6 2016.

[72] Y. Wang, W. Luo, J. Huang, C. Peng, H. Wang, C. Yuan, G. Chen, B. Zeng, L. Dai, Y. Z. Wang, W. A. Luo, J. W. Huang, C. H. Peng, H. C. Wang, C. H. Yuan, G. R. Chen, B. R. Zeng, and L. Z. Dai, "Simplification of hyperelastic constitutive model and finite element analysis of thermoplastic polyurethane elastomers," *Macromolecular Theory and Simulations*, vol. 29, p. 2000009, 7 2020.

[73] R. W. Ogden, "Large deformation isotropic elasticity – on the correlation of theory and experiment for incompressible rubberlike solids," *Proceedings of the Royal Society of London. A. Mathematical and Physical Sciences*, vol. 326, pp. 565–584, 2 1972.

[74] R. Rivlin, "Large deformation isotropic elasticity – on the correlation of theory and experiment for incompressible rubberlike solids," *Proceedings of the Royal Society of London. A. Mathematical and Physical Sciences*, vol. 326, pp. 565–584, 2 1972.

[75] O. H. Yeoh, "Some forms of the strain energy function for rubber," *Rubber Chemistry and Technology*, vol. 66, pp. 754–771, 11 1993.

[76] L. Marechal, P. Balland, L. Lindenroth, F. Petrou, C. Kontovounisios, and F. Bello, "Toward a common framework and database of materials for soft robotics," *Soft Robotics*, vol. 8, pp. 284–297, 6 2021.

[77] ASTM, "D882 standard test method for tensile properties of thin plastic sheeting," American Society for Testing and Materials, Tech. Rep., 2018. [Online]. Available: https://www.astm.org/d0882-18.html

[78] P. Ćurković and A. Jambrečić, "Improving structural design of soft actuators using finite element method analysis," *Interdisciplinary Description of Complex Systems : INDECS*, vol. 18, pp. 490–500, 10 2020.

[79] M. L. Dezaki, M. Bodaghi, A. Serjouei, S. Afazov, and A. Zolfagharian, "Soft pneumatic actuators with controllable stiffness by bio-inspired lattice chambers and fused deposition modeling 3d printing," *Advanced Engineering Materials*, vol. 25, p. 2200797, 3 2023.

[80] T. Du, L. Sun, and J. Wan, "A worm-like crawling soft robot with pneumatic actuators based on selective laser sintering of tpu powder," *Biomimetics*, vol. 7, 12 2022.

[81] Y. Wang, W. Luo, J. Huang, C. Peng, H. Wang, C. Yuan, G. Chen, B. Zeng, L. Dai, Y. Z. Wang, W. A. Luo, J. W. Huang, C. H. Peng, H. C. Wang, C. H. Yuan, G. R. Chen, B. R. Zeng, and L. Z. Dai, "Simplification of hyperelastic constitutive model and finite element analysis of thermoplastic polyurethane elastomers," *Macromolecular Theory and Simulations*, vol. 29, p. 2000009, 7 2020.

[82] D. R. Nolan, A. L. Gower, M. Destrade, R. W. Ogden, and P. McGarry, "A robust anisotropic hyperelastic formulation for the modelling of soft tissue," *Journal of the Mechanical Behavior of Biomedical Materials*, vol. 39, pp. 48–60, 9 2020.

[83] A. Rühl, "Material modelling of tpu," *On the Time and Temperature Dependent Behaviour of Laminated Amorphous Polymers Subjected to Low-Velocity Impact*, pp. 109–115, 2017.

[84] C. Tawk and G. Alici, "Finite element modeling in the design process of 3d printed pneumatic soft actuators and sensors," *Robotics 2020, Vol. 9, Page 52*, vol. 9, p. 52, 7 2020.

[85] D. Maruthavanan, A. Seibel, and J. Schlattmann, "Fluid-structure interaction modelling of a soft pneumatic actuator," *Actuators 2021, Vol. 10, Page 163*, vol. 10, p. 163, 7 2021.

[86] A. Yu, R. Gao, P. Lee, C. Mele, D. Dittmer, A. Schirm, C. Ren, and J. Tung, "Soft robotics-inspired sensing system for detecting downward movement and pistoning in prosthetic sockets: Proof of concept study," *Prosthetics and Orthotics International, Revision Requested: POI-D-22-00150*, 10 2022.

[87] E. Navas, R. Fernández, D. Sepúlveda, M. Armada, and P. Gonzalez-De-santos, "Soft grippers for automatic crop harvesting: A review," *Sensors 2021, Vol. 21, Page 2689*, vol. 21, p. 2689, 4 2021.

[88] J. Shintake, V. Cacucciolo, D. Floreano, and H. Shea, "Soft robotic grippers," *Advanced Materials*, vol. 30, 2018.

[89] A. Pagoli, F. Chapelle, J. A. Corrales-Ramon, Y. Mezouar, and Y. Lapusta, "Review of soft fluidic actuators: Classification and materials modeling analysis," *Smart Materials and Structures*, vol. 31, 2022.

[90] R. F. Shepherd, F. Ilievski, W. Choi, S. A. Morin, A. A. Stokes, A. D. Mazzeo, X. Chen, M. Wang, and G. M. Whitesides, "Multigait soft robot," *Proceedings of the National Academy of Sciences of the United States of America*, vol. 108, pp. 20 400–20 403, 12 2011.

[91] D. Xie, L. Chen, L. Liu, L. Chen, and H. Wang, "Actuators and sensors for application in agricultural robots: A review," *Machines 2022, Vol. 10, Page 913*, vol. 10, p. 913, 10 2022.

[92] C. Tawk, A. Gillett, M. I. H. Panhuis, G. M. Spinks, and G. Alici, "A 3d-printed omni-purpose soft gripper," *IEEE Transactions on Robotics*, vol. 35, pp. 1268–1275, 10 2019.

[93] W. Park, S. Seo, and J. Bae, "Development of a hybrid gripper with soft material and rigid structures," in *2018 IEEE/RSJ International Conference on Intelligent Robots and Systems (IROS)*, 2018, pp. 5930–5935.

[94] B. Mosadegh, P. Polygerinos, C. Keplinger, S. Wennstedt, R. F. Shepherd, U. Gupta, J. Shim, K. Bertoldi, C. J. Walsh, and G. M. Whitesides, "Pneumatic networks for soft robotics that actuate rapidly," *Advanced Functional Materials*, vol. 24, 2014.

[95] B. Jamil, G. Yoo, Y. Choi, and H. Rodrigue, "Proprioceptive soft pneumatic gripper for extreme environments using hybrid optical fibers," *IEEE Robotics and Automation Letters*, vol. 6, 2021.

[96] W. Jung, Y. Kang, S. Han, and Y. Hwang, "Biocompatible micro, soft bellow actuator rapidly manufactured using 3d-printed soluble mold," *Journal of Micromechanics and Microengineering*, vol. 29, 2019.

[97] W. Zhu, C. Lu, Q. Zheng, Z. Fang, H. Che, K. Tang, M. Zhu, S. Liu, and Z. Wang, "A soft-rigid hybrid gripper with lateral compliance and dexterous in-hand manipulation," *IEEE/ASME Transactions on Mechatronics*, 2022.

[98] Q. Tan, Y. Chen, J. Liu, K. Zou, J. Yi, S. Liu, and Z. Wang, "Underwater crawling robot with hydraulic soft actuators," *Frontiers in Robotics and AI*, vol. 8, p. 688697, 8 2021.

[99] S. Puhlmann, J. Harris, and O. Brock, "Rbo hand 3: A platform for soft dexterous manipulation," *IEEE Transactions on Robotics*, 2022.

[100] H. D. Yang and A. T. Asbeck, "Design and characterization of a modular hybrid continuum robotic manipulator," *IEEE/ASME Transactions on Mechatronics*, vol. 25, pp. 2812–2823, 12 2020.

[101] M. Hofer and R. D'Andrea, "Design, fabrication, modeling and control of a fabric-based spherical robotic arm," *Mechatronics*, vol. 68, p. 102369, 6 2020.

[102] J. Yi, X. Chen, C. Song, J. Zhou, Y. Liu, S. Liu, and Z. Wang, "Customizable three-dimensional-printed origami soft robotic joint with effective behavior shaping for safe interactions," *IEEE Transactions on Robotics*, vol. 35, pp. 114–123, 2 2019.

[103] W. Chen, C. Xiong, C. Liu, P. Li, and Y. Chen, "Fabrication and dynamic modeling of bidirectional bending soft actuator integrated with optical waveguide curvature sensor," *Soft Robotics*, vol. 6, 2019.

[104] Formalbs, "Tough 2000 resin technical data sheet," Formlabs, Tech. Rep., March 2020. [Online]. Available: https://formlabs-media.formlabs.com/datasheets/2001340-TDS-ENUS-0P.pdf

[105] C. Riccio, M. Civera, O. G. Ruiz, P. Pedullà, M. R. Reinoso, G. Tommasi, M. Vollaro, V. Burgio, and C. Surace, "Effects of curing on photosensitive resins in sla additive manufacturing," *Applied Mechanics 2021, Vol. 2, Pages 942-955*, vol. 2, pp. 942–955, 11 2021.

[106] L. Paez, G. Agarwal, and J. Paik, "Design and analysis of a soft pneumatic actuator with origami shell reinforcement," *Soft Robotics Journal*, vol. 3, pp. 109–119, 9 2016.

[107] A. D. Marchese, R. K. Katzschmann, and D. Rus, "A recipe for soft fluidic elastomer robots," *Soft Robotics*, vol. 2, 2015.

[108] S. Joshi and J. Paik, "Multi-dof force characterization of soft actuators," *IEEE Robotics and Automation Letters*, vol. 4, pp. 3679–3686, 10 2019.

[109] S. Russo, T. Ranzani, C. J. Walsh, R. J. Wood, S. Russo, T. Ranzani, C. J. Walsh, R. J. Wood, H. John, and A. Paulson, "An additive millimeter-scale fabrication method for soft biocompatible actuators and sensors," *Advanced Materials Technologies*, vol. 2, p. 1700135, 10 2017.

[110] S. Li, D. M. Vogt, D. Rus, and R. J. Wood, "Fluid-driven origami-inspired artificial muscles," *Proceedings of the National Academy of Sciences of the United States of America*, vol. 114, pp. 13 132–13 137, 12 2017.

[111] Z. Wang, S. Hirai, and S. Kawamura, "Challenges and opportunities in robotic food handling: A review," *Frontiers in Robotics and AI*, vol. 8, p. 789107, 1 2022.

[112] M. Intelligence, "Fresh berries market size & share analysis - industry research report - growth trends & forecasts (2023 - 2028)," Mordor Intelligence, Tech. Rep., 2023.

[113] R. K. Gallardo, E. T. Stafne, L. W. DeVetter, Q. Zhang, C. Li, F. Takeda, J. Williamson, W. Q. Yang, W. O. Cline, R. Beaudry, and R. Allen, "Blueberry producers' attitudes toward harvest mechanization for fresh market," *HortTechnology*, vol. 28, pp. 10–16, 2 2018.

[114] H. Wang, B. Gao, A. Hu, and J. He, "A variable stiffness gripper with reconfigurable finger joint for versatile manipulations," *https://home.liebertpub.com/soro*, 4 2023.

[115] J. Zhu, Z. Chai, H. Yong, Y. Xu, C. Guo, H. Ding, and Z. Wu, "Bioinspired multimodal multipose hybrid fingers for wide-range force, compliant, and stable grasping," *https://home.liebertpub.com/soro*, vol. 10, pp. 30–39, 2 2023.

[116] S. R. Kashef, S. Amini, and A. Akbarzadeh, "Robotic hand: A review on linkage-driven finger mechanisms of prosthetic hands and evaluation of the performance criteria," *Mechanism and Machine Theory*, vol. 145, p. 103677, 3 2020.

[117] D. David, P. Thérouanne, and I. Milhabet, "The acceptability of social robots: A scoping review of the recent literature," *Computers in Human Behavior*, vol. 137, p. 107419, 12 2022.

[118] S. Saunderson and G. Nejat, "Robots asking for favors: The effects of directness and familiarity on persuasive hri," *IEEE Robotics and Automation Letters*, vol. 6, pp. 1793–1800, 4 2021.

[119] A. D. Santis, B. Siciliano, A. D. Luca, and A. Bicchi, "An atlas of physical human–robot interaction," *Mechanism and Machine Theory*, vol. 43, pp. 253–270, 3 2008.

[120] Z. Xu and E. Todorov, "Design of a highly biomimetic anthropomorphic robotic hand towards artificial limb regeneration," in *2016 IEEE International Conference on Robotics and Automation (ICRA)*, 2016, pp. 3485–3492.

[121] U. Kim, D. Jung, H. Jeong, J. Park, H.-M. Jung, J. Cheong, H. R. Choi, H. Do, and C. Park, "Integrated linkage-driven dexterous anthropomorphic robotic hand," *Nature Communications*, vol. 12, p. 7177, 12 2021.

[122] J. Martin and M. Grossard, "Design of a fully modular and backdrivable dexterous hand," *The International Journal of Robotics Research*, vol. 33, pp. 783–798, 4 2014.

[123] M. Grossard, "Robust decentralized control of a fully actuated robot hand," *IFAC-PapersOnLine*, vol. 48, pp. 2176–2182, 1 2015.

[124] J. K. Paik, B. H. Shin, Y. bong Bang, and Y.-B. Shim, "Development of an anthropomorphic robotic arm and hand for interactive humanoids," *Journal of Bionic Engineering*, vol. 9, pp. 133–142, 6 2012.

[125] M. A. Saliba, M. Cutajar, and G. A. Pascalidis, "Prototype development of a prosthetic derivative of the minimal anthropomorphic artificial hand," in *2022 31st IEEE International Conference on Robot and Human Interactive Communication (RO-MAN)*, 2022, pp. 14–21.

[126] D. Wang, Y. Xiong, B. Zi, S. Qian, Z. Wang, and W. Zhu, "Design, analysis and experiment of a passively adaptive underactuated robotic hand with linkage-slider

and rack-pinion mechanisms," *Mechanism and Machine Theory*, vol. 155, p. 104092, 1 2021.

[127] R. R. Ma and A. M. Dollar, "Linkage-based analysis and optimization of an underactuated planar manipulator for in-hand manipulation," *Journal of Mechanisms and Robotics*, vol. 6, 2 2014.

[128] F. Negrello, H. S. Stuart, and M. G. Catalano, "Hands in the real world," *Frontiers in Robotics and AI*, vol. 6, 1 2020.

[129] G. Michalos, S. Makris, P. Tsarouchi, T. Guasch, D. Kontovrakis, and G. Chryssolouris, "Design considerations for safe human-robot collaborative workplaces," *Procedia CIRP*, vol. 37, pp. 248–253, 2015.

[130] R. Deimel and O. Brock, "A novel type of compliant and underactuated robotic hand for dexterous grasping," *The International Journal of Robotics Research*, vol. 35, pp. 161–185, 1 2016.

[131] H. K. Yap, J. H. Lim, F. Nasrallah, J. C. H. Goh, and R. C. H. Yeow, "A soft exoskeleton for hand assistive and rehabilitation application using pneumatic actuators with variable stiffness," in *2015 IEEE International Conference on Robotics and Automation (ICRA)*, 2015, pp. 4967–4972.

[132] Y. Jiang, "Modeling and control of a soft-rigid hybrid robotic glove for hand rehabilitation and assistance," in *2022 12th International Conference on CYBER Technology in Automation, Control, and Intelligent Systems (CYBER)*, 2022, pp. 43–48.

[133] Z. Shahid, A. L. Glatman, and S. C. Ryu, "Design of a soft composite finger with adjustable joint stiffness," *Soft Robotics*, vol. 6, pp. 722–732, 12 2019.

[134] Z. Liu, D. Chen, Z. Zhang, G. Huang, W. Liu, and Y. Jiang, *Configuration Design and Verification of Soft-Rigid Hybrid Hand with ab/adduction Movement.* ICMD 2021: Advances in Mechanical Design, 2022, vol. 111.

[135] S. Zhao, Y. Lei, Z. Wang, J. Zhang, J. Liu, P. Zheng, Z. Gong, and Y. Sun, "Biomimetic artificial joints based on multi-material pneumatic actuators developed for soft robotic finger application," *Micromachines*, vol. 12, p. 1593, 12 2021.

[136] P. Lee, C. Sjaarda, R. Cornelious, R. Gao, K. Lu, and C. Ren, "Soft-rigid hybrid revolute and prismatic joints using multilayered bellow soft pneumatic actuators: Design, characterization, and its application as soft-rigid hybrid gripper," in *2023 32nd*

IEEE International Conference on Robot and Human Interactive Communication, IEEE RO-MAN 2023 (In Press), 8 2023.

[137] I. M. Bullock, J. Z. Zheng, S. D. L. Rosa, C. Guertler, and A. M. Dollar, "Grasp frequency and usage in daily household and machine shop tasks," *IEEE Transactions on Haptics*, vol. 6, pp. 296–308, 7 2013.

[138] S. Heo, C. Kim, T. Kim, and H. Park, "Human-palm-inspired artificial skin material enhances operational functionality of hand manipulation," *Advanced Functional Materials*, vol. 30, p. 2002360, 6 2020.

[139] Y. Yang, H. Zhou, Y. Song, and P. Vink, "Identify dominant dimensions of 3d hand shapes using statistical shape model and deep neural network," *Applied Ergonomics*, vol. 96, p. 103462, 10 2021.

[140] A. Yu, K. Yick, S. Ng, and J. Yip, "2d and 3d anatomical analyses of hand dimensions for custom-made gloves," *Applied Ergonomics*, vol. 44, pp. 381–392, 5 2013.

[141] A. Buryanov and V. Kotiuk, "Proportions of hand segments," *International Journal of Morphology*, vol. 28, 9 2010.

[142] L. Dunai, M. Novak, and C. G. Espert, "Human hand anatomy-based prosthetic hand," *Sensors*, vol. 21, p. 137, 12 2020.

[143] R. Mutlu, G. Alici, M. in het Panhuis, and G. M. Spinks, "3d printed flexure hinges for soft monolithic prosthetic fingers," *Soft Robotics*, vol. 3, pp. 120–133, 9 2016.

[144] J.-J. Cabibihan, F. Alkhatib, M. Mudassir, L. A. Lambert, O. S. Al-Kwifi, K. Diab, and E. Mahdi, "Suitability of the openly accessible 3d printed prosthetic hands for war-wounded children," *Frontiers in Robotics and AI*, vol. 7, 1 2021.

[145] J. Zhou, X. Chen, U. Chang, J.-T. Lu, C. C. Y. Leung, Y. Chen, Y. Hu, and Z. Wang, "A soft-robotic approach to anthropomorphic robotic hand dexterity," *IEEE Access*, vol. 7, pp. 101 483–101 495, 2019.

[146] A. Kapandji, "Cotation clinique de l'opposition et de la contre-opposition du pouce," *Annales de Chirurgie de la Main*, vol. 5, pp. 67–73, 1 1986.

[147] T. Feix, J. Romero, H.-B. Schmiedmayer, A. M. Dollar, and D. Kragic, "The grasp taxonomy of human grasp types," *IEEE Transactions on Human-Machine Systems*, vol. 46, pp. 66–77, 2 2016.

[148] A. N. S. Institute, "Ansi/nfpa/t3.21.3 r1-2008 (r2018) pneumatic fluid power - flow rating test procedure and reporting method - for fixed orifice components," American National Standards Institute, Tech. Rep., 2008. [Online]. Available: https://webstore.ansi.org/standards/nfpa-fluid/nfpat321r12008r2018

[149] E. H. Skorina, M. Luo, W. Tao, F. Chen, J. Fu, and C. D. Onal, "Adapting to flexibility: Model reference adaptive control of soft bending actuators," *IEEE Robotics and Automation Letters*, vol. 2, no. 2, pp. 964–970, 2017.

[150] E. H. Skorina, M. Luo, S. Ozel, F. Chen, W. Tao, and C. D. Onal, "Feedforward augmented sliding mode motion control of antagonistic soft pneumatic actuators," in *2015 IEEE International Conference on Robotics and Automation (ICRA)*, 2015, pp. 2544–2549.

[151] P. Ioannou and B. Fidan, *Adaptive Control Tutorial*. Philadelphia, PA: Society for Industrial and Applied Mathematics, 2006. [Online]. Available: https://epubs.siam.org/doi/abs/10.1137/1.9780898718652

APPENDICES

Appendix A

Detailed Fabrication Steps

The appendix document provided below entails the detailed step-by-step of fabrication procedures of the single-layer soft pneumatic actuator, using SLA-based 3D printer, as well as additional items used in E5-3008 lab, such as microfluidic chip fabrication and plasma bonding procedures. This document have been used as a training document to help co-op students to catch up with the fabrication methods.

Summary of Fabrication Procedures

20220906 Rev 1 – Peter Lee

Highlighted = Software

***Outlines the chronological order of the tasks completed – Use it as reference only**

****If you have any questions, please feel free to ask Runze or Peter**

Singular Soft Fluidic Actuator

Task	Description/Details
Design - **AutoCAD**	- Make the desired Elastomer/Insert shape on AutoCAD
Export design and Convert in **Cricut Design Space**	- Using 'Export' command in AutoCAD, save the design as .bmp file - Load the design in Cricut software: Upload – Simple – Erase – Cut Image - Upload
Cricut Setup	- First check the dimensions and quantity, then click 'Make it' - Select cutting board size and setup as below: Material: Double-Sided Adhesive (almost always) Pressure: Default for Elastomer / High for Insert and Fabric
Elastomers and Inserts Preparation	- Cut the elastomer roll into the required size - Attach the material onto the cutting board
Automated Cutting with Cricut	- Load the cutting board + material into the machine - Click GO button
(optional) Tab for the Tubing	- Prepare paper tabs of 0.75" ~ 1" width
Heat Press	- Prepare non-sticking press papers, one for the bottom and the other for the top of the stack - Check if the press surface is clear of dust/residue - Stack all materials, beware of the order: (Fabric) + Elastomer + Insert + (Tab) + Elastomer - Heat Press at ~ 110 °C for ~ 30+ seconds
Let it cool down	- Elastomers will be thermally active when heated, and hence has tendency to stick to one another. Wait for it to cool down entirely to avoid the trouble
Insert Tubing	- While the tabs are still in place, insert the tubing - Once the tubing is well within the actuator, remove the tab
Hand Ironing and Glue Seal	- Prepare heat insulating material - Preheat Mini Iron to Low Temp - Thermally close the tubing adjacent - Glue to provide complete seal

3D Printing (Formlabs Form 3 SLA Printer)

Task	Description/Details
3D Modelling - **Solidworks**	- Make the desired 3D Model on Solidworks and save the .SLDPRT
Export design	- Save as .STL file
PreForm	- Open PreForm - Job Setup (can be changed later at any time): Resin: Tough 2000 Version: V1 Print Setting: Default Layer Thickness: Fixed or Adaptive (depends on the part) - Load the .STL file - Orient and locate the part correctly onto the print platform - Set support and etc if required
Printer Setup	- Printer setup depends on the resin type you're printing with - Insert resin Tank - Insert print platform - Insert Resin Cartridge: remember to open the cap
Print and Monitoring	- Connect to printer via USB - Upload PreForm to the printer - Select Print - Wait for the printer to fill resin, heat up, print first layer
Parts Removal	- Prepare the resin waste box, Kimwipes, IPA bottle - Take the platform off the printer: let the excess resins fall into the tank first - Remove the parts off the platform using the tools
IPA bath	- Place parts in IPA agitator bath for 20 mins
IPA clean	- Place parts in secondary/tertiary IPA bath
Drying	- Place parts in drying box, wait till fully dried
UV Cure	- UV cure the parts, refer to the Formlabs website for time and temperature - For clear resin parts to be used as molds, need to cure for 60 mins at 60 °C

Chip Fabrication

Task	Description/Details
Preparation of the Mold	- Most of the molds are fabricated via 3D printer, needs to be fully UV cured
PDMS Estimation	- Estimate the amount of PDMS required for your mold - Easiest is to find the estimated volume of the parts, multiply by density (around 970~1000 kg/m^3), and multiply by 1.3~1.5 as safety factor
PDMS Mixing	- Prepare PDMS for mixing - 10:1 ratio – 1 g of curing agent per 10 g of PDMS - Mix PDMS under the fume hood, mix well for ~3 mins
Degassing	- Place the mixed PDMS in vacuum chamber E3 Vacuum = -25 ~ -27 in.Hg E5 Vacuum = -0.08 ~ -0.09 MPa - Operate Vacuum pump, go to the desired vacuum level - Wait about 40~60 mins for degassing
Pouring	- Once PDMS is degassed, pour PDMS into the molds
PDMS Curing	- Place the PDMS + mold on heat plate or oven - Curing temperature and duration can be varied - Typical setup: Cure for 1 day at 90~95 °C
Delamination	- Once PDMS is fully cured, carefully delaminate from the mold - Place Saran wrap over the area to be plasma bonded to protect from dust
Hole Punching	- Hole punch at required locations
Plasma Bonding	- Read Below for Plasma bonding procedures

Plasma Bonding

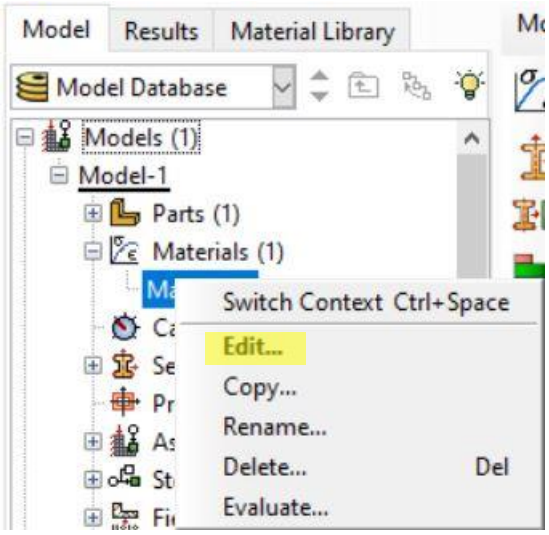
Task	Description/Details
Gather Parts	- Prepare all the components to be plasma bonded, bring with you: 2 layers of the chip, PDMS membrane of your choice, X-Acto knife, (AllenKey)
Clean the Chamber	- Give a quick IPA clean in the plasma chamber
Air-Clean Parts	- Remove the Saran Wrap from the chip layer - Give a quick air blast to remove any dusts on surface
Place in the Chamber	- Place 1 layer of the chip and the membrane in the chamber. - Surface to be bonded facing up
Plasma Bond	- First ensure all valves are fully closed, plasma power is on - Turn on the pump, go to 300 mTorr - Turn on the air valve all the way to flush for ~16 seconds - Partially close the air valve, go to 500 mTorr - Turn on Plasma all the way, wait ~1 minute - Turn off plasma, turn off the pump and power, open the air valve all the way - Quickly grab the components and bond the chip layer onto the membrane
Membrane Excess Removal	- Use the X-Acto knife to cut off the excess membrane parts and delaminate
Repeat	- Place parts in the chamber again - Repeat the plasma bonding procedure

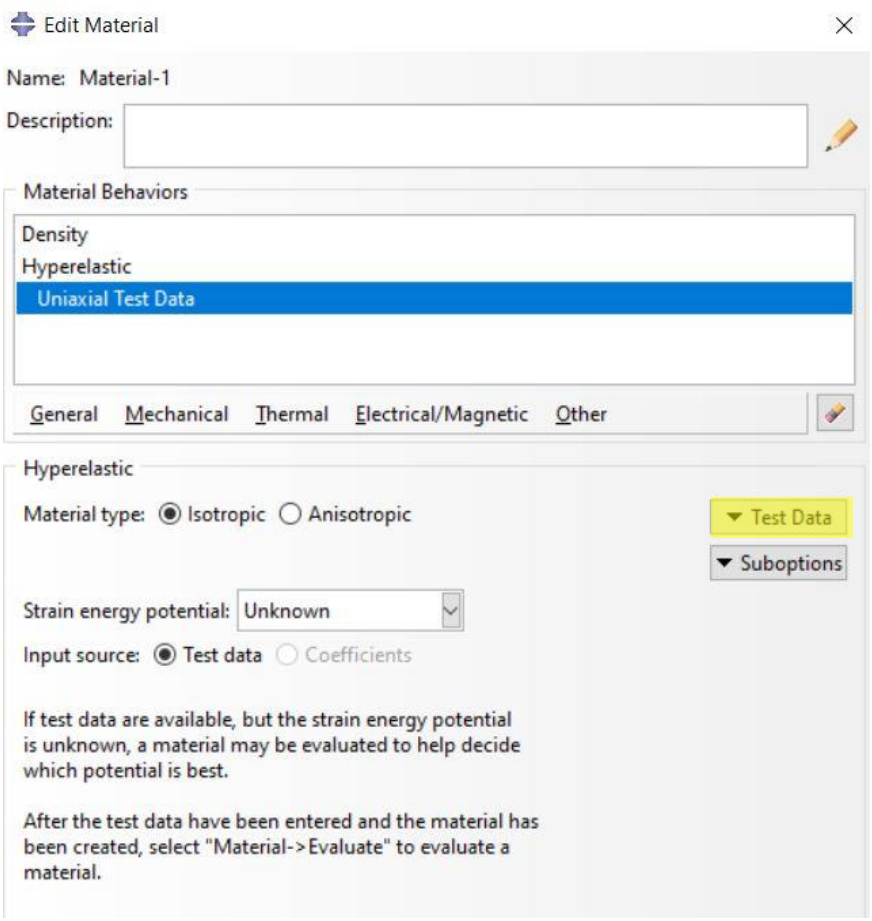
Appendix B

ABAQUS Material Evaluation

The instruction below illustrates the step-by-step process of attaining coefficients of the hyperelastic models using the empirically attained uniaxial tensile data. The stability of the material evaluation results simply means that model may have instability in convergence at certain range of strain, due to insufficient modes (i.e. equibiaxial or planar stress-strain data) to full define the behavior of the material across all range. Typically, the instability occurs at higher strain ranges, and it is dependent on the hyperelastic model.

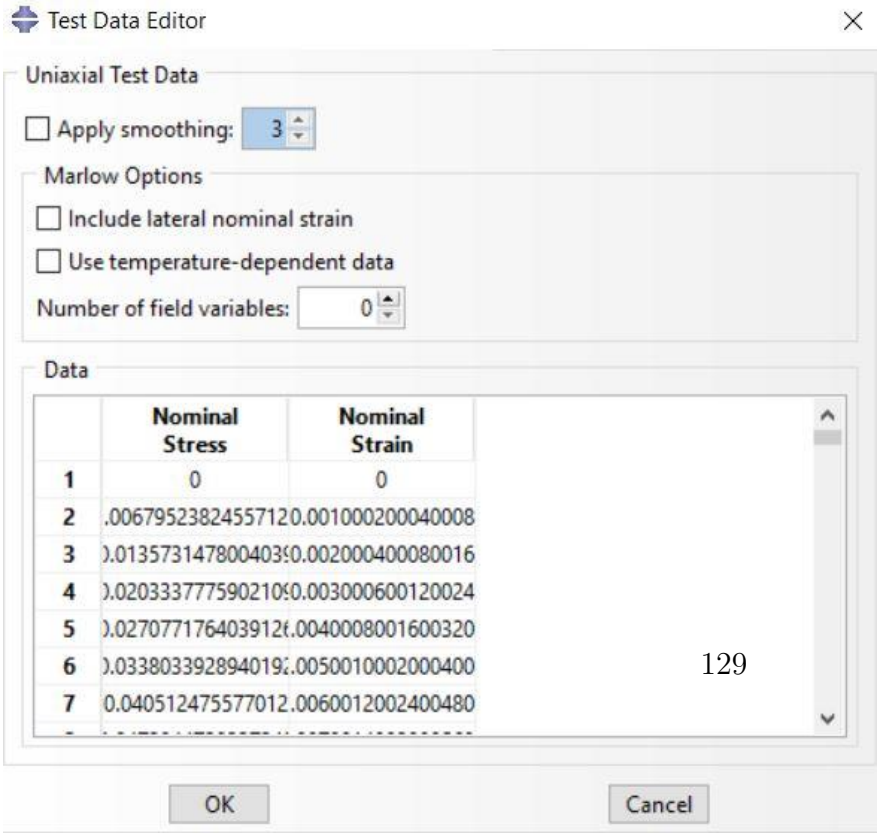
Step 1



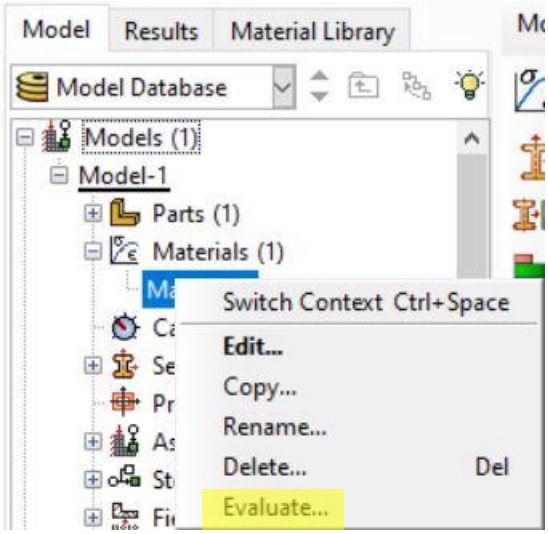


Step 2: Choose 'Isotropic' with Input Source 'Test data'

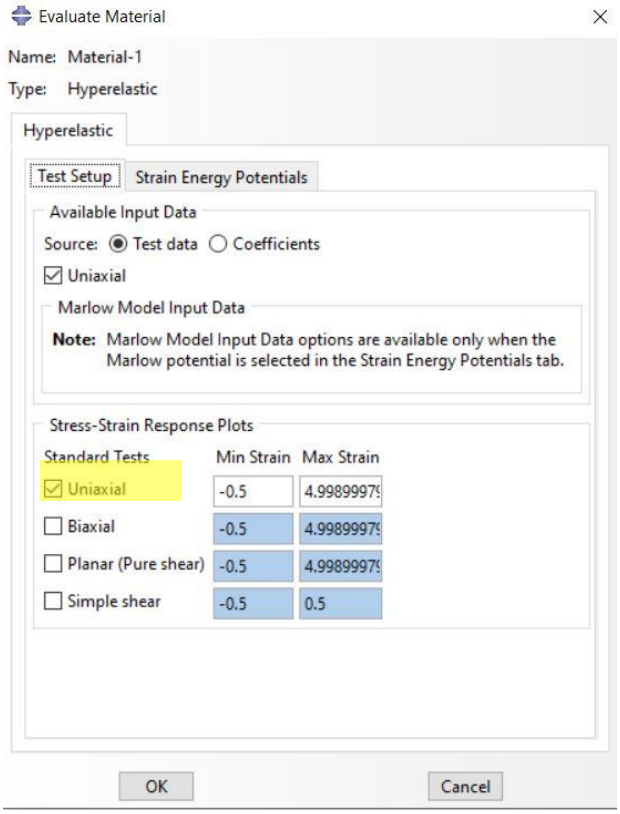
Step 3: Input Uniaxial Data



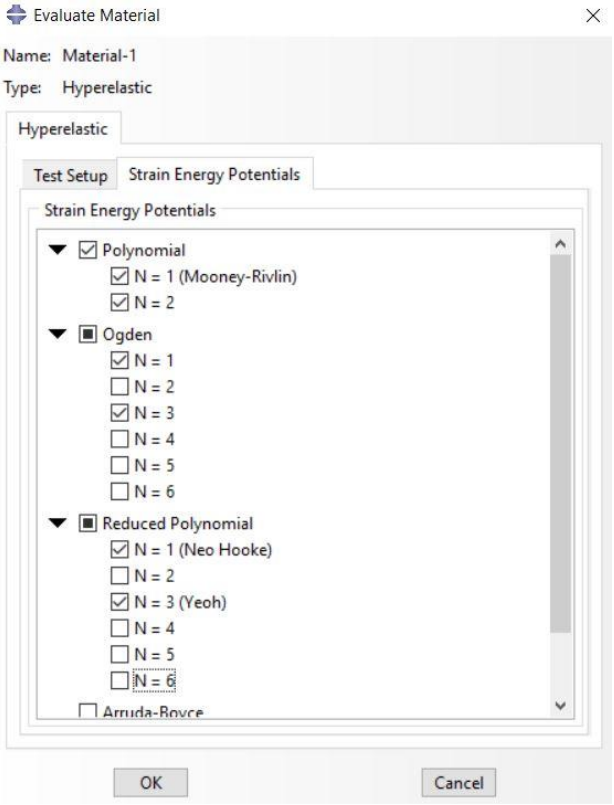
Step 4: Evaluate



Step 5: Select Evaluation Data



Step 6: Select Desired Models



Results

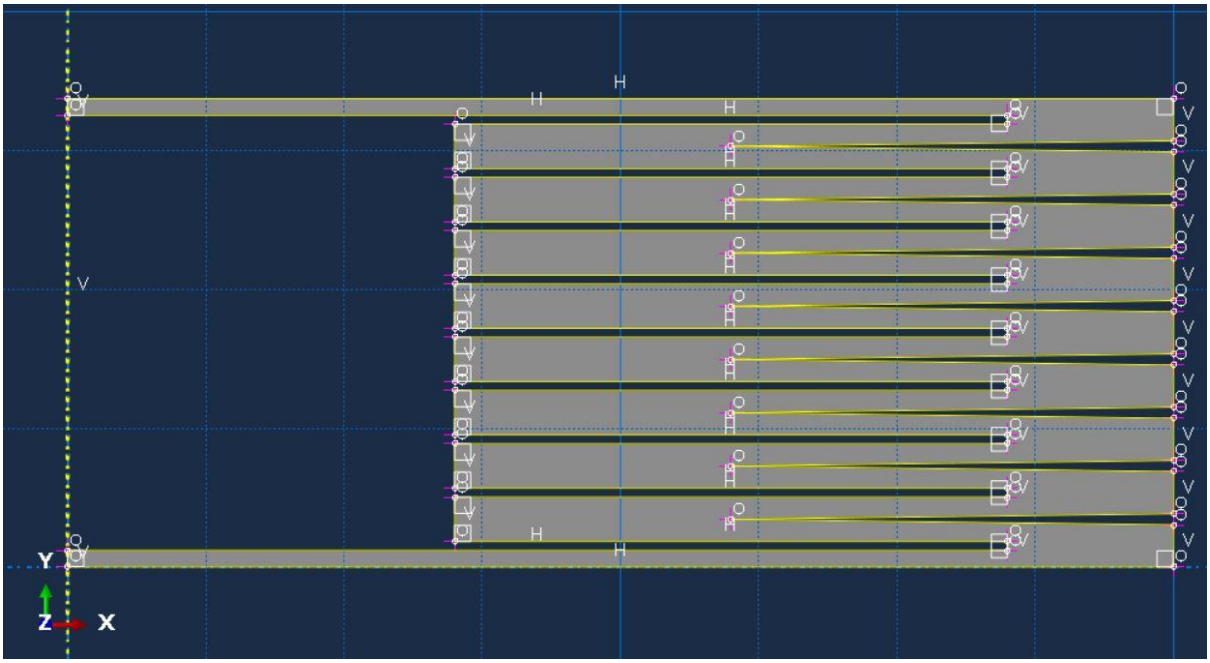
Constitutive Model	Material Coefficients				Stability	Fitting Error
	Deviatoric Terms			Volumetric		
Ogden (N=3)	μ_i	α_i	-	D	Stable	2.9085 E-02
	-2.5359	1.6269		0		
	1.0806	2.4824		0		
	3.7527	0.6109		0		
Mooney-Rivlin	C10	C01	-	D1	Stable	16.20
	0.4705	0.6204		0		
Polynomial (N=2)	C10	C01	-	D1	Unstable	5.0490 E-03
	0.8971	0.2342		0		
	C20	C11	C02	D2		
	1.849 E-04	3.0315 E-02	-0.2433	0		
Neo-Hookean	C10	C01	-	D1	Stable	113.0
	0.6621	0		0		

Appendix C

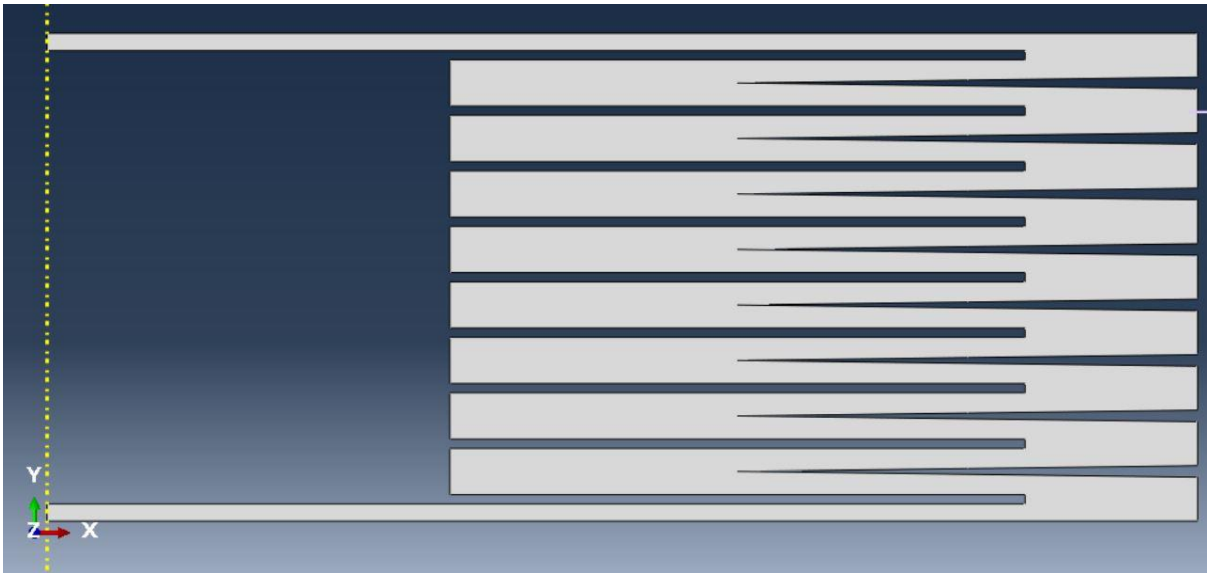
ABAQUS FEM Model Setup

The steps below illustrate the necessary step for setting up the Axisymmetric Finite Element Model for simulating the quasi-static expansion of the TPU-MBSPA. This appendix is only meant to provide insight as to how to set it up in general, specific details of the simulation need to be varied depending on the application and desired outputs. There exists numerous tutorials online.

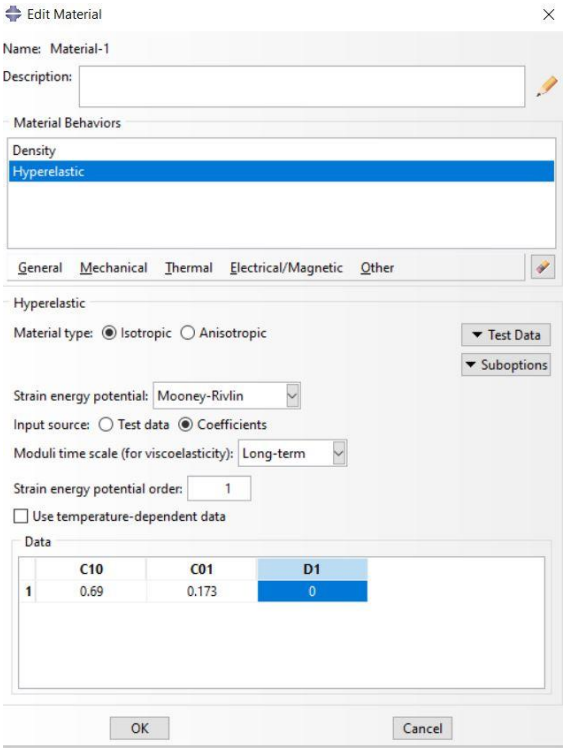
Step 1: Define the cross-sectional sketch of the axisymmetric model

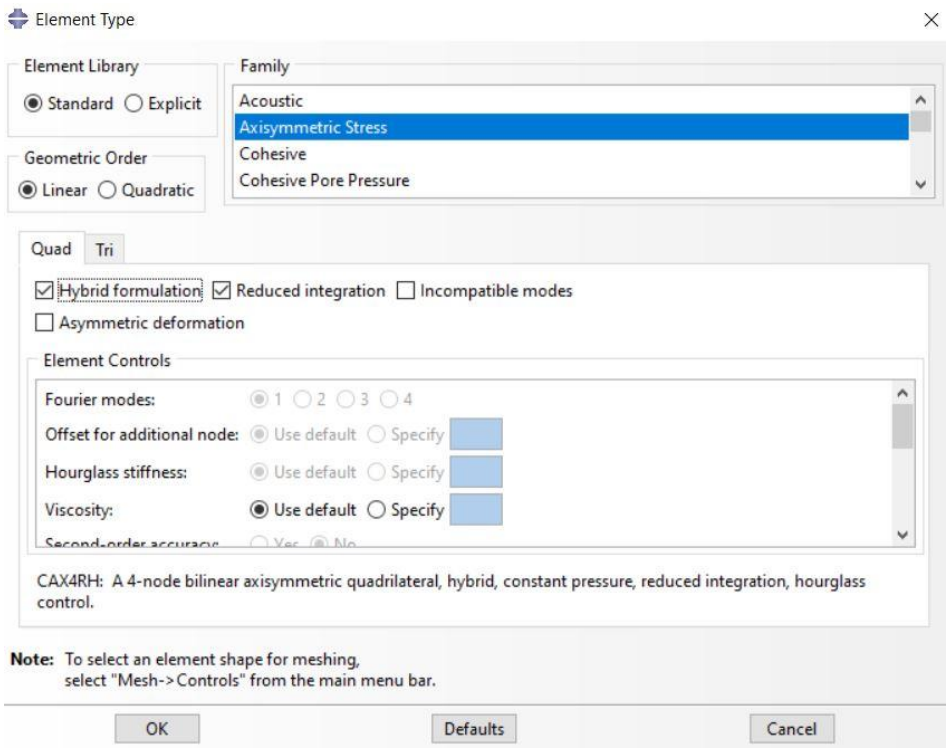


Step 2: Regenerate the model and define all points of interest



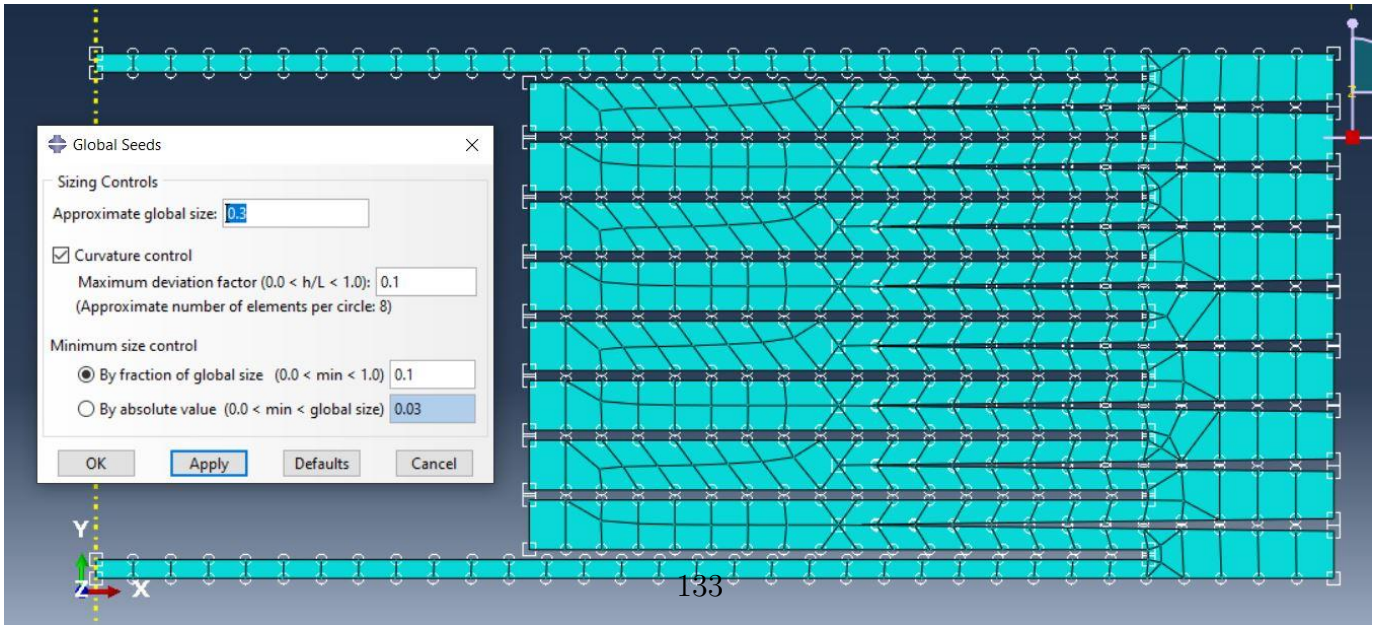
Step 3: Apply the Hyperelastic Coefficients

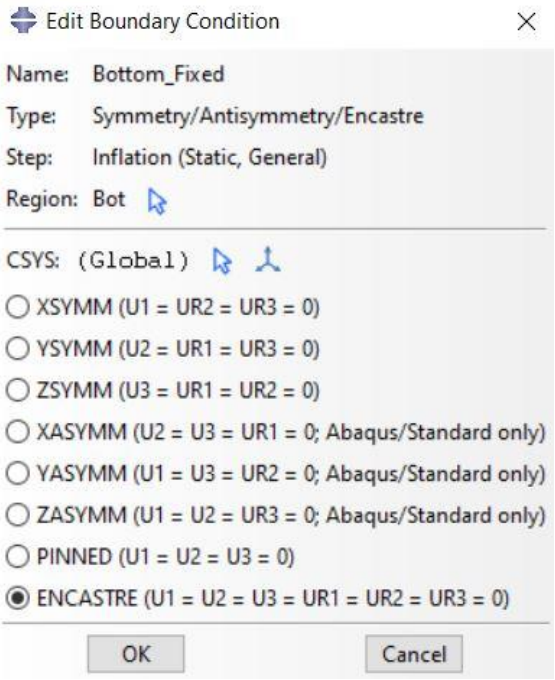




Step 4: For incompressible material (using Abaqus/Standard), use Hybrid Formulation as Mesh Element Type

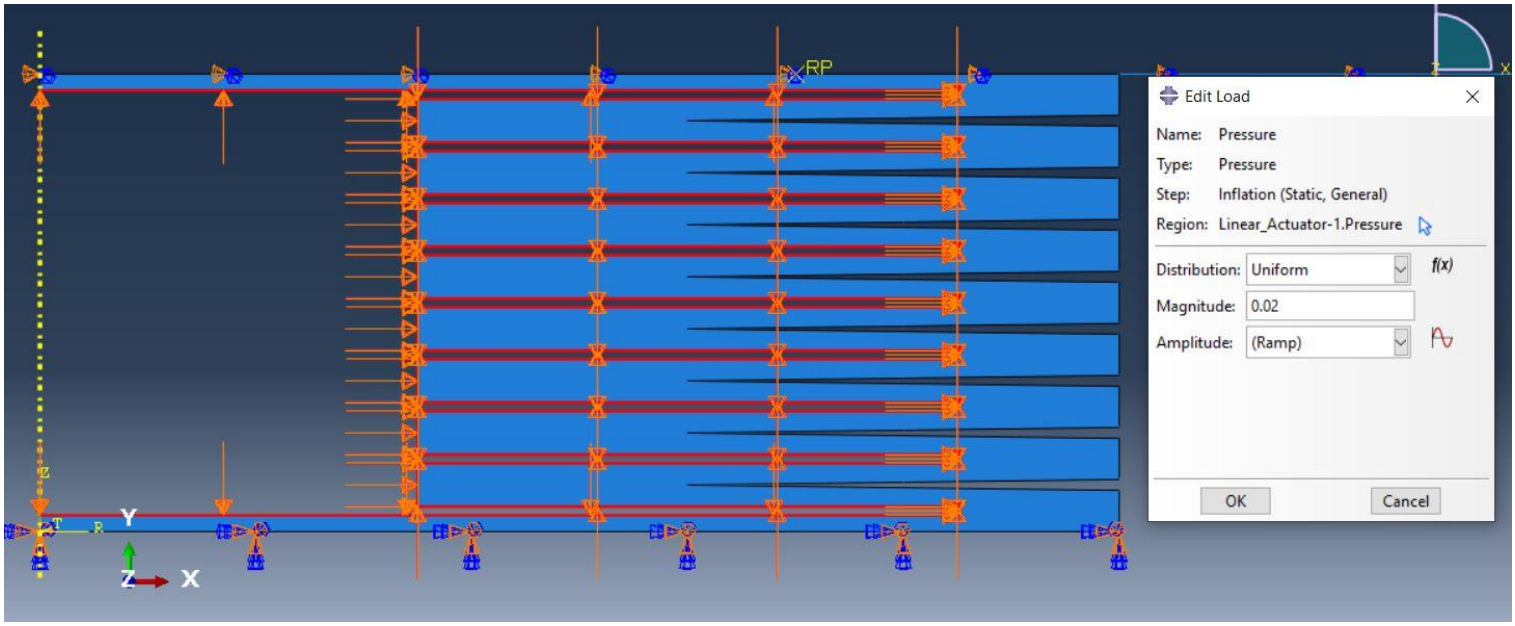
Step 5: Apply Global Seeds and Generate Mesh



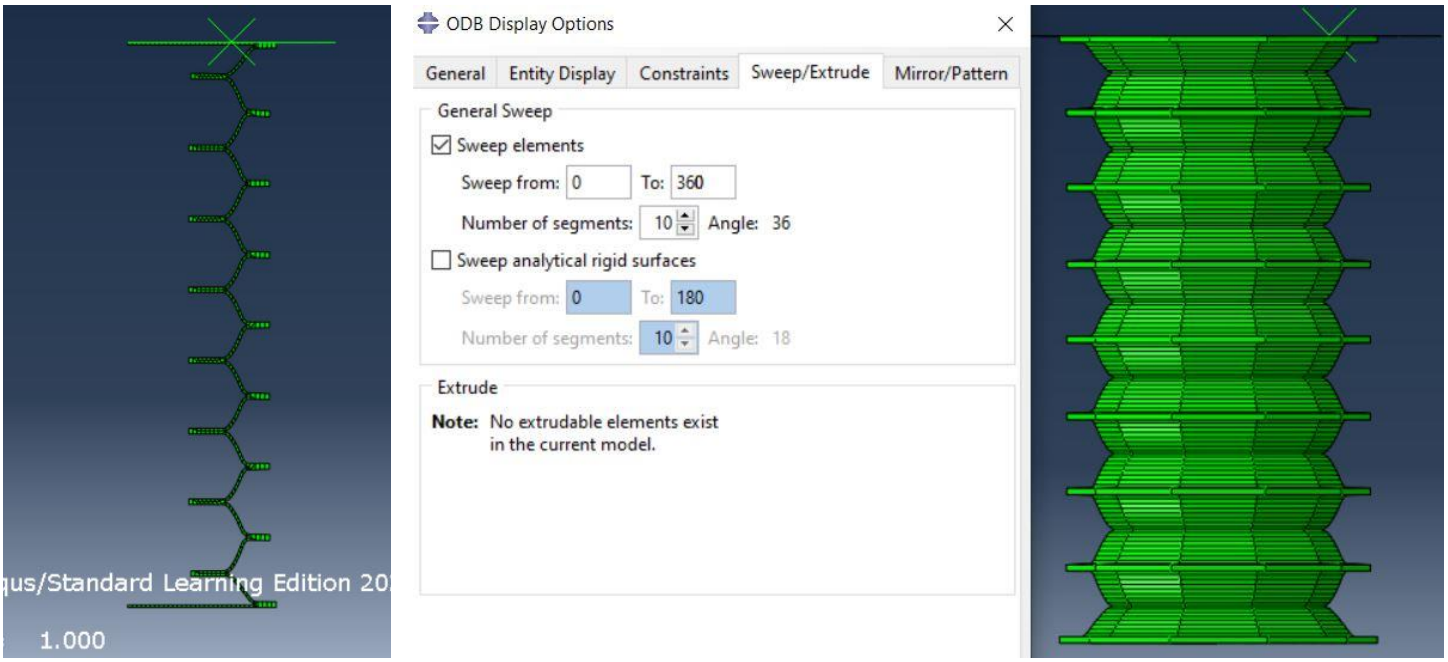


Step 6: After Generating Step, Apply Boundary Conditions. Use Encastre for the Bottom Surface and YASYMM for the Top Surface.

Step 7: Apply the Internal Pressures, Keep in Mind of the Units. The Input Stress of Uniaxial Tensile Data was in [MPa], hence Input Pressure Below is 20 [kPa]



Step 8: After Running the Simulation, the Results can be Swept for Better Illustration



Step 9: Resultant Displacement Output at Varied Pressure Input. In case of Quasi-Static Output, Multiply the Step Time by Input Pressure

